Adaptive optics for fluorescence correlation spectroscopy

Joseph Gallagher

To cite this version:

Joseph Gallagher. Adaptive optics for fluorescence correlation spectroscopy. Instrumentation and Detectors [physics.ins-det]. Université Grenoble Alpes, 2017. English. NNT : 2017GREAY054 . tel-01819084

HAL Id: tel-01819084
https://theses.hal.science/tel-01819084

Submitted on 20 Jun 2018

Communauté
UNIVERSITÉ Grenoble Alpes

THÈSE

Pour obtenir le grade de

DOCTEUR DE LA COMMUNAUTÉ UNIVERSITÉ GRENOBLE ALPES

Spécialité : **Physique pour les Sciences du Vivant**
Arrêté ministériel : 25 mai 2016

Présentée par

Joseph Gallagher

Thèse dirigée par **Giovanni CAPPELLO**
et codirigée par **Irène WANG**

préparée au sein du **Laboratoire Interdisciplinaire de Physique (LIPhy)**
et de l'**École Doctorale de Physique**

Adaptive Optics for Fluorescence Correlation Spectroscopy

Thèse soutenue publiquement le **19/9/2017,**
devant le jury composé de :

Joerg ENDERLEIN
Prof. – Drittes Physikalisches Institut, Göttingen, Rapporteur
Eva PEBAY-PEYROULA
Prof. – Institut Biologie Structurale, Grenoble, Examinatrice, Présidente du Jury
Emmanuel BOSSY
Prof. – Laboratoire Interdisciplinaire de Physique, Grenoble, Examinateur
Kevin VYNCK
CR – Institut d'Optique, Bordeaux, Examinateur

Contents

Abstract

This work details the development of an adaptive optics (AO) system for fluorescence correlation spectroscopy (FCS). We look at the instrumentation of such a system in detail, most importantly, its wave-front shaping element, an ALPAO deformable mirror (DM).

We design and implement a confocal microscope with an AO system capable of performing FCS measurements and we assess the performance of such a system. We look in detail at the metrics obtained from FCS measurements in order to optimise the AO system. We examine in detail the statistics of these metrics and their sensitivity to aberration. We determine the possible attainable wave-front correction given the concentration of fluorescent species and its brightness using either the intensity signal or molecular brightness as a metric.

We examine the effect of aberrations on FCS measurements.

Finally we apply this system to perform absolute measurements of mechanical stress in spheroids. We show that without the intervention of AO in the FCS measurements to determine the pressure, the measurements would be biased, such that we would be led to believe the interior pressure of a spheroid under no external pressure is on the order of 5 kPa, when in fact it is negligible.

Keywords

Optics, Microscopy, Control Theory, FCS, Spheroids, Optical Pressure Sensor,

Resumé

Ce travail détaille le développement d'un système d'optique adaptative (AO) pour la spectroscopie de corrélation de fluorescence (FCS). Nous regardons l'instrumentation d'un tel système en détail, surtout, son élément de mise en forme fond d'onde, un miroir déformable ALPAO (DM).

Nous concevons et mettons en œuvre un microscope confocal avec un système AO capable d'effectuer des mesures FCS et nous évaluons la préforme d'un tel système. Nous examinons en détail les métriques obtenues à partir des mesures FCS afin d'optimiser le système AO. Nous examinons en détail les statistiques de ces indicateurs et leur sensibilité aux aberrations. Nous déterminons la possible correction de front d'onde possible compte tenu de la concentration d'espèces fluorescentes et de sa luminosité en utilisant soit une intensité de clarté unique soit une luminosité moléculaire en tant que métrique.

Nous examinons l'effet des aberrations sur les mesures FCS.

Enfin, nous appliquons ce système pour effectuer des mesures absolues du stress mécanique dans les sphéroïdes. Nous montrons qu'avec l'intervention d'AO dans les mesures FCS pour déterminer la pression, les mesures seraient biaisées, de sorte qu'on nous ferait croire que la pression intérieure d'un sphéroïde sous aucune pression externe est de l'ordre de 5 kPa, Alors qu'en fait, il est négligeable.

Mots-clés

Optique, Microscopie, Theorie de Controle, FCS, Spheröids, Capteur de pression optique,

Acknowledgements

I would like to thank all those involved in the coordination and direction of my thesis and also the many collaborators I had the opportunity to work with over the past few years that allowed this thesis to be possible. Antoine Delon, for taking a chance on me and bringing me to Grenoble to join the MOTIV team, for his scientific direction, and also his generosity and friendship. Irène Wang, for her scientific direction, for guiding every aspect of my PhD, for the immense quantity of science she has taught me, and also for her kindness and friendship. Giovanni Cappello who also took a chance on me to be part of an amazing project, for his scientific direction, for his loyalty and support, and for his amazing creativity. Julien Charton, who exceeded all my expectations by getting involved in every aspect of the PhD even beyond ALPAO's part, for his scientific direction, for integrating me into the team at ALPAO, and for his support.

I would also like to mention my gratitude especially for Philippe Moreau, Monika Dolega, Pierre Mahiou, Mickael Micallef and Jacques Derouard who I had the greatest pleasure of working with. I worked closest with them during the PhD and they each taught me much technical knowledge from there expertise for which I am very grateful. They each also supported me and got me through some of the most turbulent moments of the last three years, a kindness which I will not forget.

Un grand merci à tout l'équipe à ALPAO qui m'a beaucoup soutenu, qui m'a beaucoup appris, et pour leur amicalité. C'etait un grand plaisir de travailler avec vous tous.

Thank you to everyone I worked with in LIPhy, particularly team MOTIV, for your support, for the warmest of welcomes to to a strange place that I've experienced, and for the many friendships.

To my friends, some old and many new, you are the best. I really appreciate you all even though I may struggle to show it at times. You made all the struggles easier, and all the successes so much sweeter.

To Carol, whom I am so grateful to have in my life, thank you for your friendship and your love.

To my family who have always been my rock and supported me through everything, you mean so much to me. Thank you for your love and for making dreams possible. I hope I have made you proud Mum, and that I can continue to do so, I miss you.

Strive not to be a success but rather to be of value.

Albert Einstein, .

Chapter 1
Introduction

Fluorescence correlation spectroscopy (FCS) is a quantitative optical technique to characterise diffusing fluorescent species by analysing the statistics of their signal fluctuations. A simple but powerful technique made possible through modern high resolution microscopes to perform localised measurements of the dynamics of fluorescent molecules in live biological specimens. Optical microscopes are ubiquitous tools in many areas of science and engineering where inspection of micrometer scale structures is required. They are of particular importance in the life sciences in order to visualise cellular structures and the interactions of biological samples. The optical systems of most modern microscopes have been optimised to produce effectively diffraction limited point spread functions (PSF) with sub-micrometre lateral and axial dimensions. This in turn defines observation volumes for FCS on the order of femtolitres. However, the optical properties of the specimens themselves can diminish these performances considerably within a few tens of wavelengths deep into a biological sample. This loss of resolution is due to optical aberrations induced mainly by the inhomogeneities of the samples. Here we look at the causes of optical aberrations in microscopy, their effect on FCS and the application of Adaptive Optics (AO) to these techniques.

1.1
Fluorescence Correlation Spectroscopy

FCS was first introduced in 1972 by Magde et al. [1] as a technique to study relaxation times of freely diffusing fluorescent molecules. Originally developed as a chemistry technique, they would perturb the equilibrium state of chemical reactions in order to measure the characteristic time for its return to equilibrium. Here they used the temporal fluctuations of their fluorescence measurements at a single point to get this information. Before this work, these fluctuations were often regarded as measurement noise. However their research showed definitively that the temporal statistics of the fluorescence fluctuations indeed offered details into the dynamics of the fluorophore under observation. Although the intention of these first measurements were used to chemical reactions out of equilibrium, this signal was found to be quite difficult to discriminate from the dominant source of fluctuations, the normal diffusion of the molecules. Thus FCS became instead a technique primarily to study the diffusion of near equilibrium state species. Since then much work was consecrated to improve FCS as a tool for such.

A large advance came when groups began to formalise diffusion models to fit the data recorded from these measurements and extract critical information. Perhaps the most successful of these is the normal 3D diffusion model formalised by Aragon et al. [2] but also by Elson and Magde [3]. The model of Aragon et al. is ubiquitous, even 30 years later [4–6], and used extensively in this thesis.

The principle of operation of modern FCS measurements is shown here in simplified version in figure 1.1. A stable source for fluorescence excitation, typically a solid state laser or similar, is focused into a sample by means of a high numerical aperture (NA) objective. The fluorescence signal emitted is then gathered, usually by means of epi-detection, and focussed on to a pinhole, in the case of single photon excitation. Detection is generally performed by way of a sensitive detector, such as a photon counting

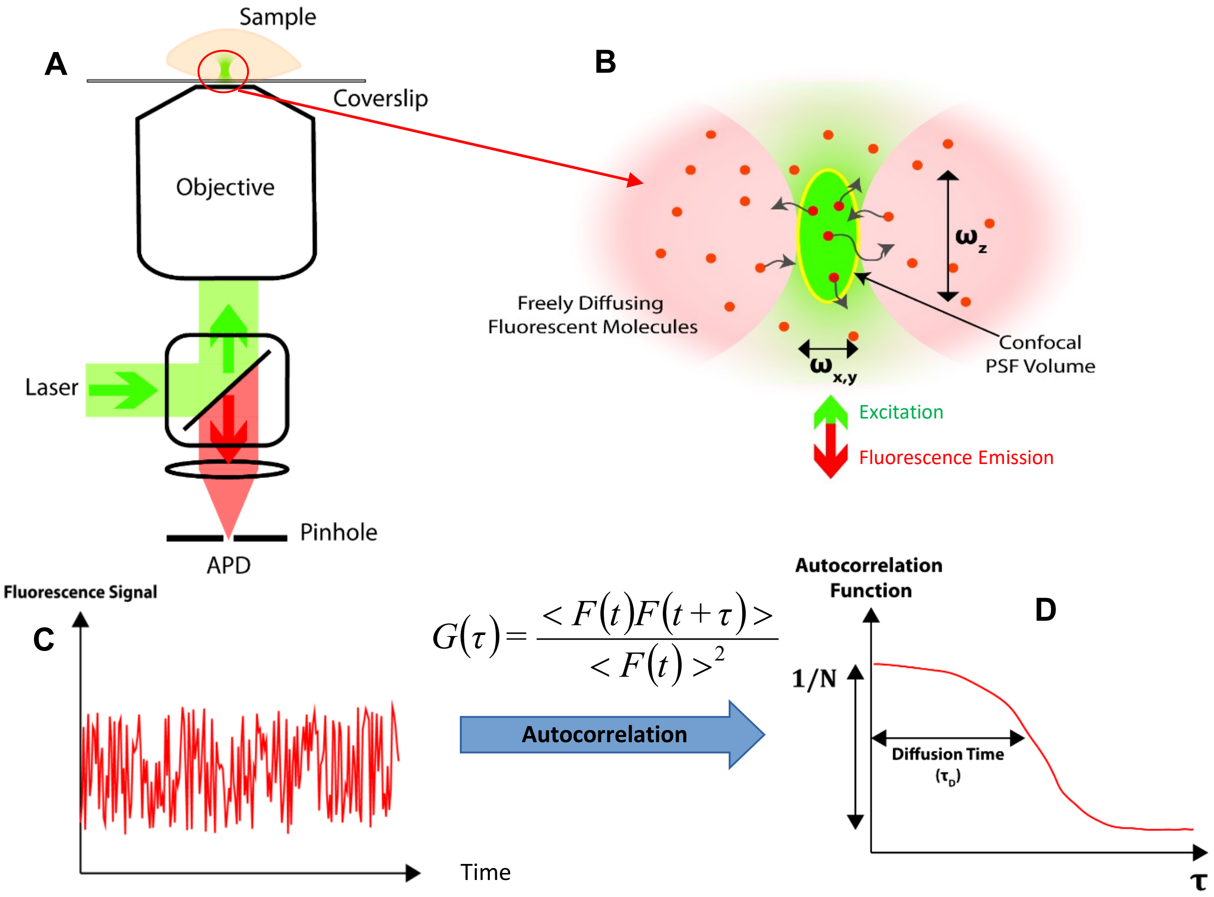

Figure 1.1 – Fluorescence Correlation Spectroscopy. **A)** FCS measurements are generally conducted using high numerical aperture (NA) objectives with laser excitation of a weakly concentrated diffusing fluorophore, and the fluorescence is detected using a sensitive detector such as an photon counting device in an epi detection scheme. **B)** Close up of the observation volume. High NA objectives give a narrow beam waist ($W_{(x,y)}$) while a pinhole provides optical sectioning in z in the case of a confocal system. The effective FCS observation volume is outlined in yellow. **B)** A typical fluorescence signal trace recorded via a photon counting device is autocorrelated to give: **D)** the autocorrelation function which can be fitted to determine N molecules in the observation volume and the typical molecule diffusion time τ_D, among others.

device, at very high cadence (typically < 10 µs). The high acquisition rate is important to accurately sample the diffusion time of fluorophores passing through the observation volume.

The observation volume is analogous to the PSF of the optical system. In fact, they are often identical [7]. It is important that the volume be as small as possible as this allows for higher concentrations of fluorophores to be accurately measured. The lateral size of the observation volume (w_{xy}) is determined by the NA of the objective as [8,9]:

$$w_{xy} = \frac{\lambda}{\mathrm{NA}} \tag{1-1}$$

where λ is the wavelength of the light. The axial height of the observation volume is also determined largely by the NA but also by the pinhole [8].

The photons detected by the microscope are counted at intervals δt, typical on the order of 1 µs, for a period, t, of 1 second to 1 minute depending on the sample. Then the fluorescence signal is autocorrelated to determine the autocorrelation function $G(\tau)$ defined as:

$$G(\tau) = \frac{\langle F(t)F(t+\tau)\rangle}{\langle F(t)\rangle^2} = \frac{\langle \delta F(t)\delta F(t+\tau)\rangle}{\langle F(t)\rangle^2} + 1 \tag{1-2}$$

To then extract relevant information about the diffusive species present in the observation volume $G(\tau)$ must be fitted using appropriate models. As mentioned above, we use the normal 3D diffusion model of Aragon et al. in this thesis [2]. This model assumes observation volume with a 3D Gaussian profile, elongated in the axial direction compared to the lateral. In its simplest form for a single diffusing fluorescent species it can be expressed as:

$$G(\tau) = \frac{1}{\langle N \rangle}\left(1 + \frac{\tau}{\tau_D}\right)^{-1}\left(1 + \frac{\tau}{S^2\tau_D}\right)^{-\frac{1}{2}} + 1 \tag{1-3}$$

where $\langle N \rangle$ is the mean number of molecules in the observation volume (referred to as N mol. hereafter), τ_D is the diffusion time and S is the parameter describing the ratio of the axial length of the observation volume, w_z, to width, w_{xy}. It should be noted that the height of the autocorrelation determines N mol. and τ_D relates to its decay (Figure 1.1 D). Because the geometry of the observation volume is not in fact 3D Gaussian generally the parameter S is a tuning parameter which is determined from fitting of measured curves [10, 11]. The diffusion time determined from equation 1-3 can be related to w_{xy} and the diffusion constant of the fluorescent molecule, D, by:

$$\tau_D = \frac{w_{xy}^2}{4D}. \tag{1-4}$$

Equation 1-3 accounts well for the diffusion dynamics of molecules at the µs scale. However, for shorter time scales other effects can be seen in the measured autocorrelation functions. One such factor which should be taken into account is the effect of the intramolecular dynamics between singlet and triplet states of the molecules [12]. This leads to the modified form of equation 1-3 to account for this effect:

$$G(\tau) = \frac{1}{\langle N \rangle}\left(1 + \frac{f_T}{1 - f_T}e^{\frac{-\tau}{\tau_T}}\right)\left(1 + \frac{\tau}{\tau_D}\right)^{-1}\left(1 + \frac{\tau}{S^2\tau_D}\right)^{-\frac{1}{2}} + 1 \tag{1-5}$$

where τ_T is the triplet state resident time and f_T is the fraction of the species in this state. This form of the 3D normal diffusion model will be used throughout this thesis.

1.2
High Resolution Microscopy for FCS

Widefield fluorescence microscopy can achieve high resolution images of specimen through excitation of fluorescent markers. However there is the problem of out of focus light contribution at the image plane [13]. This certainly does not create a controlled observation volume required for FCS.

Techniques such as confocal fluorescence and Two Photon Excitation Fluorescence (TPEF) microscopy have fulfilled many requirements of life scientists through highly localised sample excitation. In confocal techniques, out of focus light is rejected by a pinhole, which is placed at a plane conjugate to the sample focus and the illumination source [14]. TPEF utilises non linear effects, whereby fluorescence is achieved by the simultaneous absorption of 2 photons to produced fluorescence at half the excitation wavelength [15]. These techniques can produce pseudo 3D images by utilising image stacking whereby the sample is scanned through the focus of the objective. Because of the ability of these techniques to efficiently reject out of focus light, theoretically these microscopes can image into samples as deep as the objective working distance will physically allow. The advent of microscopes with well controlled PSF geometry in 3D finally allowed for FCS measurements in biological samples [16–18].

Although many new microscopy techniques have been established to further increase the resolution of optical microscopes, even beyond the optical diffraction limit [19, 20] the potential of all of these methods is in fact severely limited due to aberrations. Optical resolution degradation due to aberrations is two-fold in such techniques; the excitation light is blurred as it passes into the sample and; the fluorescence light is also blurred exiting the sample. The decreasing signal with depth in biological samples can be compensated to a degree by increasing the power of the excitation source [14] but this does not account for the distorted shape of the PSF which translates to a changing observation volume in FCS measurements. Simple aberrations such as spherical aberration can be compensated by tuning of the tube length [21, 22], a technique now incorporated in many modern objectives by way of a correction collar [23], but not all aberrations in microscopy are as simple.

1.3
Aberrations in microscopy

The loss of resolution in microscope systems is not usually due to fault of the optical design of the microscope components. These have been designed at great expense to account for the media which they image through. However, significant optical aberrations still appear. The most frequently encountered aberrations in microscopes are due to the refractive index mismatches between the imaging medium and the sample. This is of particular issue in microscopy due to the high angles of converging rays of light passing through media of changing refractive indices. This results in light rays from different angles converginf at different possitions along the optical axis, elongating the PSF, and introducing what is commonly referred to as spherical aberration in the images. The effect of this refractive index mismatch was examined by Hell et al. who showed the increasing degradation of the focal spot in a confocal microscope with depth due to the refractive index mismatch [24]. Analytical solutions for the effect of these aberrations with depth for high Numerical Aperture (NA) systems were shown by Török et al. [25] and a summary of investigations into the effects of refractive index mismatch until 1998 was performed by Egner and Hell [26].

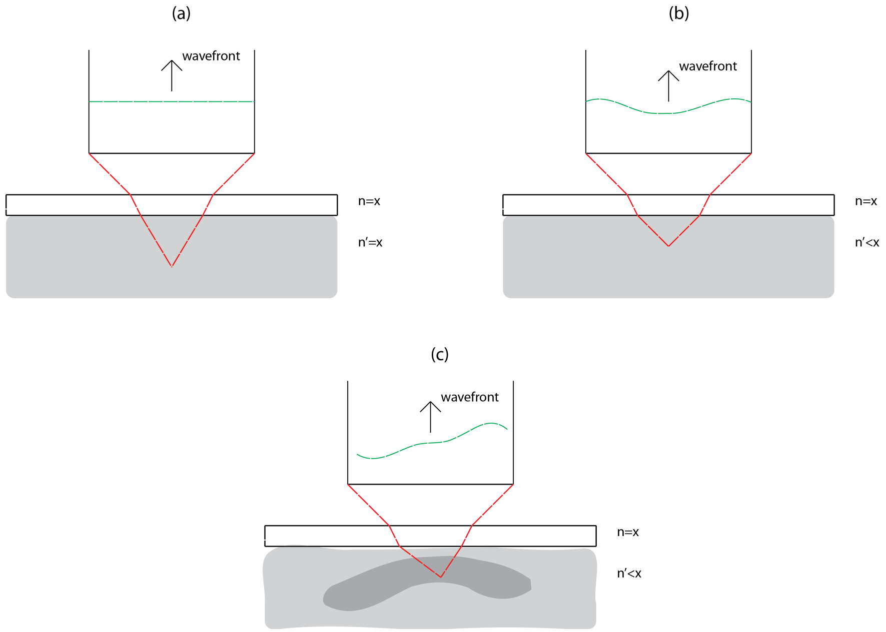

Figure 1.2 – Refractive index mismatch aberrations in microscopy; a) an ideal microscope imaging system with an immersion medium with the same refractive index as both the sample and the coverslip, and; b) an air objective with refractive index changes between the coverslip - specimen boundary and the coverslip - imaging media boundary. This induces spherical aberration in the wave-front, which increases with depth through the sample; c) an optically inhomogeneous sample which introduces complex wave-front aberrations.

Coupled with the problem of the refractive index mismatch, biological specimens are optically inhomogeneous, mainly due to spatial variations in the refractive indices of the sample [27]. These variations can induce dramatic phase changes in light wave-fronts passing in and out of the sample thus inducing further undesirable aberrations in images of the samples [28, 29], also shown in figure 1.2. The earliest measurements of variation of specimen refractive indices were made by Bolin et al. in 1989, using an optical fibre carrying coherent light with mammalian tissue as cladding for the fibre [30]. The refractive index, n through the sample was quantified assuming a homogeneous tissue. This work was a remarkable step forward for microscopy because prior to this it was assumed that these tissues were largely water based and therefore with $n = 1.33$, whereas the average experimental values were closer to $n = 1.4$. Using a similar preparation with a digital holographic microscope (DHM), Charriere et al. demonstrated a method to determine refractive indices in specimens up to an accuracy of ± 0.01 with spatial resolution of a few microns and form a 3D spatial map of the refractive indices of the sample [31]. Optical coherence tomography methods have also been used to determine the spatial variance of refractive indices in living tissue [32].

The effect of these aberrations is that microscopes cannot image effectively through thick biological samples or samples in which the refractive index varies significantly across it. As a result, the samples need to be modified significantly in order to be imaged effectively by preparing very thin, fixed sections, with contrast materials or other imaging aids added. All of these techniques modify the natural behaviour of specimens and destroy the ability to examine natural *in vivo* biological dynamics. Thus, there is a large demand to increase the effectiveness of microscopes to image deeper into live biological samples without having to modify the behaviour of the specimens.

1.4
Adaptive Optics for microscopy and FCS

Adaptive optics is a technique borrowed from astronomy, originally used to correct for aberrations induced by atmospheric turbulence when imaging stars from ground-based telescopes [33]. The technology has subsequently been adapted to ophthalmic imaging and has been developed to image single rods and cones in vivo in the human retina [34]. Booth et al. demonstrated the potential of adaptive optics for microscopy in 1998 by simulating the effect of correcting for spherical aberration in a confocal microscope when focusing into water under a glass coverslip [35]. This work showed that through correction of 1st and 2nd order spherical aberration alone, the range and resolution of an oil immersion objective could be massively increased. A theoretical examination of imaging more complicated structures, such as skin, showed that although careful selection of immersion media and reduction of pupil size could reduce aberrations in certain conditions, only a variable phase correction element could efficiently account for the range of aberrations encountered [36]. Although TPEF microscopy has the advantage over confocal microscopy of reduced out of focus light contribution, the degradation of the focal spot due to aberrations is, in fact, very similar [37] and this was shown experimentally also [38]. The spatial variation of refractive indices in samples was also demonstrated to require wave-front correction in order to restore the optimum resolution of microscopes [39].

The first demonstration of adaptive optics in a microscope was a transmission illumination confocal microscope with a tip-tilt correction mirror [40]. However, this only corrected for the misalignment of the fluorescence signal with respect to the imaging pinhole. A similar system was developed for a transmission TPEF microscope with a Deformable Mirror (DM) correcting for some blurring aberrations [41]. It is important to note that transmission illumination is rare in confocal and TPEF microscopy. Most adopt an epi-illumination configuration where both excitation and fluorescence light passes through the objective and, as such, they do not suffer from tip-tilt misalignment issues. Although some groups have implemented AO systems based on the correction of on-axis aberrations alone, it is now well known that off-axis aberrations are also present in most systems [42].

A typical AO system consists of some form of wave-front sensor that detects the aberrations in the wave-front incident on the detector, a deformable element, which can apply a correction to the wave-front and a control system. The layout shown in figure 1.3 is a closed loop AO configuration, where the wave-front sensor is located after the deformable element in a feedback loop configuration. Open loop configurations are also possible. Wave-front sensing can be achieved by either direct wave-front sensing methods or through indirect methods. Indirect methods are known as sensor-less AO systems and a number of variations have been developed for the specific requirements and conditions of microscopy.

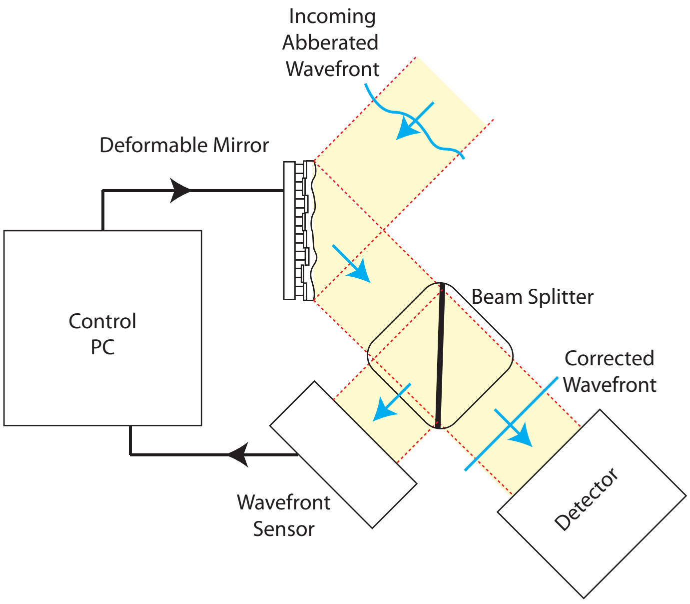

Figure 1.3 – Schematic of a typical AO system.

Wave-front Correction Devices

Correction of an aberrated wave-front in an optical system is most commonly achieved by physically altering the shape of the wave-front using controllable devices, which can change the phase of the wave-front in different parts of the pupil independently. The DM is the most common device used for this purpose in ophthalmic [34], astronomical [33] and microscopy applications [43].

Most commercially available DMs are based on continuous face-sheet reflective membranes which are deformed using various methods. The method of actuation varies: the first electronically controlled DMs were actuated by piezo actuators, either by; a monolithic slab of piezo material beneath a deformable membrane with local electrodes [44]; or by multiple individual actuators [45]. Despite the well-known hysteresis and non-linearites associated, Piezo actuation is still used today in some commercial systems. Curvature control can also be obtained using biomorph mirrors [46]. Electrostatically actuated DMs are now becoming widely available and boast fast response times [47,48]. Some have been developed for push and pull actuation with a second electrode per actuator [49]. Using new techniques to address mirror actuators, such a multiplexing control, mirror shapes can be refreshed at kHz rates [50]. More exotic technologies under development include ferrofluidic mirrors and thermally actuated mirrors [51,52].

All of these technologies have their merits and limitations and therefore choosing a mirror for a particular application is non trivial. Mirror specifications give somewhat little information as to how mirrors will perform for particular applications as they do not indicate the aberration modes, which a DM can or cannot correct [53]. A number of comparisons have been carried out examining these characteristics [54] and the application of DM's to particular tasks [55, 56] but these are rare, mainly due to the cost of acquiring so many mirrors in the same lab. As such, DM's must be characterised for each individual application. Booth et al. developed two new methods to characterise deformable mirrors without the use of a wave-front sensor [57]. One method employs an interference technique based on alignment of fringe patterns and the other involves using a liquid crystal spatial light modulator to generate accurately known wave-fronts which the mirror can correct.

The liquid crystal spatial light modulator (often referred to simply as SLM for short) is also gaining popularity in AO systems. For a long time, SLMs could not achieve the correction speed of DMs. This is generally not a factor in many forms of microscopy where temporal dynamics of samples are many orders of magnitude slower than say the dynamics of atmospheric turbulence in astronomy [58, 59], although recent trends in AO correction in microscopy demonstrate that it could benefit greatly from fast responding wave-front correctors for correction of scattering [60], or fast refocusing [61]. Recently, however, new ferroelectric SLMs have been developed and when combined with modern Graphics Processor Units (GPU) which improve greatly on this [62]. Still, by far the biggest drawback of SLMs is their sensitivity to changes in polarisation, which limits their application [53].

In this thesis we use an electro-magnetically actuated continuous face-sheet DM developed by ALPAO [63, 64]. This technology generally produces DMs that can have all the advantages of the aforemetioned technologies and few of their disadvantages. The small contact area of the actuators to the continuous face-sheet ensure maximum flatness with no artefacts compared to other technologies with large actuation areas or discontinuities [47, 65]. The magneto-static actuation ensures high linearity actuation, low hysteresis and the highest wave-front stroke available in the industry. The actuator spring technology allows for high speed wave-front shaping with up to 4 kHz refresh rate. Finally, 97 actuators allows Zernike aberration modes up 10th radial to be produced.

Sensorless Adaptive Optics

One of the major problems encountered when people first wanted to implement AO in microscopy was wave-front sensing. Generally in other applications of AO before, such as astronomical telescopes and retinal imaging devices, direct wave-front sensing was ubiquitous ever since AO's first conception [66]. This is to say that a scheme similar to figure 1.3 was implemented with a dedicated device that could measure aberrations, generally using a 'guide star'; a natural or artificial point source close to the focal plane of interest whose image perturbation would indicate the aberrations present [67]. However this caused a headache in microscopy. Implementing such a scheme involved: placing a point source accurately inside delicate micrometre size samples, employing extra light sources, adding a wave-front sensor and otherwise complicating the optical path on top of the wave-front correction device to be used. Thus some groups set about finding ways to avoid the use of direct wave-front sensing to simplify the systems and thus sensorless AO was born.

In sensorless AO microscopy the deformable element is shaped to improve certain image metrics with no prior knowledge of the wave-front aberrations present. The first sensorless algorithms were stochastic, whereby random wave-front shapes were continuously applied to the deformable element until the desired correction was achieved [41].

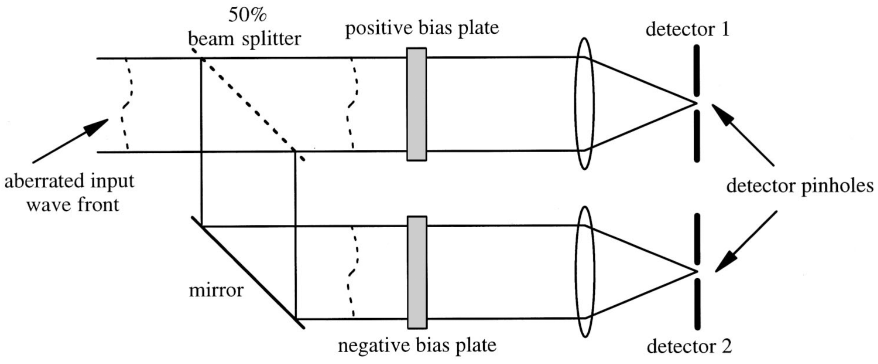

Figure 1.4 – Theoretical implementation of a modal metric wave-front sensor. The collimated light of the detection of path of a microscope is spilt on to two paths, each are then bias by an equal known aberration modes of opposite sign and focused on individual detectors. The original aberration amplitude of the tested mode can then be fitted using the detected amplitudes as a metric (*from Neil et al.* [68]).

In 2000, Neil et al. proposed a modal wave-front sensor which split the detection path of the microscope into two paths with individual sensors and introducing a known aberration bias to each path [68]. They proposed using Zernike aberration modes where the amplitude of each mode could be fitted from the 2 bias measurements (shown in figure 1.4). This was first realised conceptually using an SLM [58, 68], and soon after they implemented it in a two-photon microscope [69].

This method soon evolved to use a single wave-front correction device and a single detection path [70]. The aberration modes were introduced sequentially by the wave-front correction device itself and the metric, the fluorescence intensity, was measured using the system's primary detection path. This was successfully implemented on a confocal setup [71] and was a leap forward in AO technology for microscopy using a single device to both measure and correct wave-front aberrations, fast correction using specimen image metrics to optimise orthogonal aberration modes with no loss of photons other than the element and its conjugating elements. Soon thereafter this technique was implemented on a two-photon microscope [72]. This was somewhat simpler than a confocal implementation as only the excitation path needed to be corrected since in a two-photon system the detector size can be infinite [53] as optical sectioning is inherent of the non-linear excitation of the light [15]

The optimisation algorithms of the sequential modal metric optimisation systems relied on known or calibrated responses to aberration modes and generally used two or more measurements per mode to find the optimal amplitudes. In 2006 Booth proposed to improve the efficiency of these optimisation algorithms two-fold [73]: Firstly, he proposed that the optimisation function for any metric could be approximated as quadratic in the vicinity of its maximum, regardless of its true function [74]. Secondly he proposed that knowing the aberration function, using this approximation or otherwise, the aberration amplitude of a mode could be determined using N+1 measurements where N is the number of aberration modes tested. Further, in 2007 Booth proposed to extend this even to large aberrations [53] using a change of mode basis which better represented the aberration spectrum encountered, such as Lukosz modes [75,76].

In 2008, in the same group, an AO system for structured illumination microscopy was implemented [77]. This system is worthy of note here because of the unique problem it proposed: the aberration mode basis would influence the illumination structures used in the system. Here they proposed a method to detect and correct for aberration cross-talk using the AO optimisation metrics. Here they fitted a function to the metric describe the cross-talk between each pair of aberration modes in order to produce a new orthogonal mode basis. This problem is not unique to this modality, for example in other microscopes aberration mode cross-talk can impose image shifts which can be corrected in a similar manner [29,78,79]. Later this method was applied to completely calibrate an AO system and its aberration mode basis in a microscope [79].

Many more sensor-less AO systems were developed subsequently and in parallel for almost all common modalities of microscopy using a variety of optimisation metrics [80–87]. However relatively few comparison studies have been done to compare the image metrics and correction algorithms. Facomprez et al. [78] highlighted that the number of algorithm iterations required for correction is highly dependent on the initial amount of aberration present. Larger aberrations require exponentially larger amounts of incident photons for correction, which can be a concern if photo bleaching or photo toxicity is to be avoided. The speed of correction of the algorithms for similar metrics varies but speed can often lead to trade-offs such as cross-talk between modes [88,89].

More recently, some groups have been trending away from modal metric optimisation techniques in favour of more complex wave-front correction techniques facilitated by exotic wave-front correction devices [60,90]. Another sensor-less method which evolved known as pupil segmentation facilitated by the binary on-off nature of certain wave-front correctors [91,92].

Direct Wave-front Sensing in Microscopy

Much effort was concentrated into abandoning direct wave-front sensing techniques in microscopy, generally in favour of the more simplified instrumentation associated with sensor-less AO techniques. However, some groups did not follow this school of thought and went about solving the problems of implementing direct wave-front sensing techniques in microscopy. Direct wave-front sensing is a method whereby the phase in the pupil is retrieved via direct measurements. The most common and robust method for achieving this is by use of a Shack-Hartmann wave-front sensor (SHWFS) [67]. The SHWFS was developed for astronomical applications initially to characterise telescope optics and then to detect aberrations when imaging from ground-based telescopes through the atmosphere [33].

In microscopy various guide stars have been employed for measuring wave-fronts using a SHWFS. The first implementation of a SHWFS in a microscope was by Beverage et al. who used fluorescent microspheres as guide stars to characterise the 3D PSF of a microscope [93]. Fluorescent beads have since been used by many groups as guide stars for AO systems in wide-field fluorescence microscopy [94, 95] and laser scanning confocal microscopy [96]. The introduction of foreign objects, such as microspheres, into samples is often difficult and can be damaging to live cells. Some work has been done to facilitate SHWFSs without fluorescent beads such as the introduction of fluorescent proteins into live samples [97, 98]. Some systems use back scattered light from the excitation source for wave-front sensing [99, 100]. Some groups have implemented AO systems with non-linear guide stars for mutliphoton microscopy [101]. More recently Wang et al. used a non-linear guide star with a SHWFS to perform high resolution imaging of an entire zebrafish volume [102].

Other than SHWFS, some effort has been concentrated into other types of direct wave-front sensors. Coherence gated wave-front sensing is one such method [103]. The method relies depends on sources with a short coherence length such that only light back-scattered from the focus will be interfered to measure the wave-front and out of focus light is rejected. Thus it is mainly applicable only to mutltiphoton microscopy techniques [104]. Setups like these have showed promising results for wave-front correction especially in scattering samples [105]. Also worthy of note is another method adapted successfully from astronomy is phase-diversity sensing. This was implemented in a brightfield microscope for software correction of images [106, 107] and also in a physically corrected system [108, 109].

Adaptive Optics for FCS

The sensitivity of FCS to aberrations seems somewhat taboo when compared to the quantity of work in the literature to understand the effects of aberrations on imaging. It is generally acknowledged that optical aberrations have an impact on FCS measurements but to date relatively few works have been carried out to quantify its effects. Enderlein et al. discussed the effects of refractive index mismatch due to single cells showing that the diffusion time can be biased by up 12 % with for a $\delta n < 0.04$ [10]. This is already a considerable bias but generally this will not pose significant issue as FCS metrics are generally reported in relative values and not absolute. However, refractive index mismatches can actually be larger than this even in single cells [110, 111], certainly in tissues [30] and this does not account for the heterogeneity of cells [27, 28, 39]. So for FCS measurements in heterogeneous environments it can be seen already that there are going to be problems.

In the group of Enderlein et al. some research has been done into the effect of spherical aberration on FCS measurements [112] and then compared to the technique of dual focus FCS [113]. Dual focus FCS is a technique where by two overlapping FCS observation volumes are created in a microscope, with a well known separation between their respective centres, and cross-correlation of their fluorescence signals is analysed. The separation between the two volumes is created by using linearly polarised sources, with polarisations perpendicular to each other, that separated by a Normanski prism near placed at the objective back aperture. In order to distinguish each of the volumes in detection, the excitation by each of the pulsed sources in delayed by half their repetition frequency and the detection electronics are synchronised with the excitation pulses. In their work they demonstrate a considerable robustness to aberrations induced by varying the thickness of the cover-slip by up to 10 µm compared to the objective's corrected value. This is the only FCS technique that proposes a solution to aberration bias in FCS due to sample heterogeneity, other than the AO systems presented in this thesis, to the best of the author's knowledge.

Subsequently in our group Leroux et al. developed an AO microscope to better understand the impact of low-order aberrations (up to 4th radial order Zernike aberrations) on FCS and also examine the effect of AO correction [114]. They demonstrated the effect of refractive index mismatch on autocorrelation curves

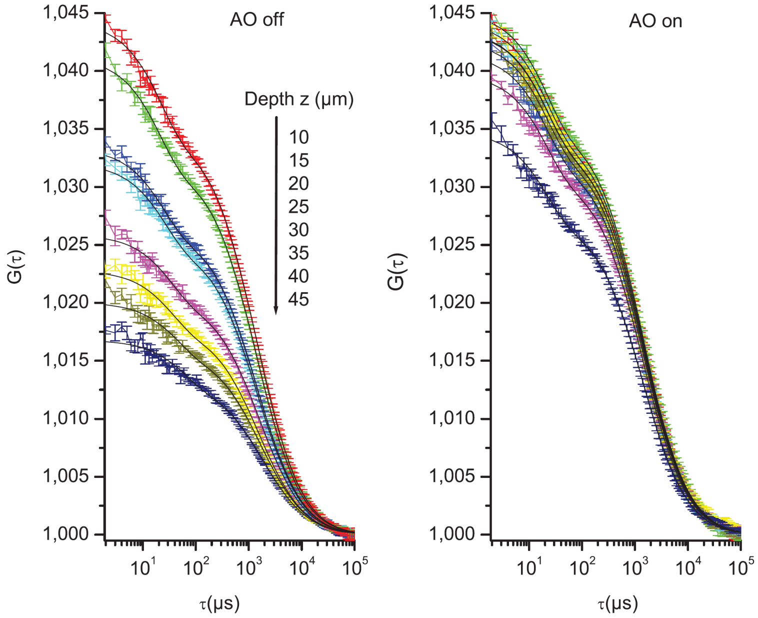

Figure 1.5 – The autocorrelation function (ACF) recorded in 70.4% glycerol solutions, without (left) and with (right) AO. The amplitude of the ACF decreases dramatically with increasing observation depth (from 10 to 45 μm) when the AO is not switched on. The superimposed dark solid lines are the fits performed using equation 1-5.(*from Leroux et al.* [114]).

measured at increasing depths (shown here in figure 1.5 [114])). This effect bias the fitted measurements of τ_D and N mol. However, they succeeded in renormalising these metrics by correcting for only 7 Zernike aberration modes.

Also in this work, they demonstrated a sensitivity of the molecular brightness (the count rate per molecule) which scales with the Strehl^2. This sensitivity is 3 times greater than the sensitivity of the same modes to count rate alone. Not only does this show the strong sensitivity of FCS to aberrations compared to imaging but also demonstrates a very sensitive metric which can be used for AO optimisation.

This sensitivity was further demonstrated by Leroux et al. when performing FCS measurements at various depths behind isolated living cells [115]. Despite the sensitivity of FCS to small aberrations, they showed that, by using adaptive optics, unbiased FCS measurements were possible in complex samples such as spheroids (multicellular aggregates used as tumour models) [116]. In this work they performed FCS measurements in the intercellular spaces in the spheroids by introducing a fluorescent species (Sulforhodamine B) into the culture medium which was small enough to penetrate the spheroid and diffuse in these spaces. These works by Leroux et al. form the basis for the work in this thesis, to further understand factors which bias and complicate FCS measurements in tissue and to determine if these obstacles can be overcome for reliable FCS measurements in tissue in order to provide a new biophysical probe in these environments.

1.5
Outline of the thesis

In this thesis we will discuss the instrumentation, techniques and applications of FCS with AO.

In chapter 2 we look in detail at the implementation of the AO microscope using for FCS measurements throughout this thesis. We examine each optical sub-system in detail and look at the techniques used to calibrate and control the ensemble.

In chapter 3 we analyse the method of modal metric optimisation of a wave-front for FCS measurements. Here we examine in detail the metrics used for the optimisation and calculate the potential wave-front correction accuracy using these metrics in a range of conditions. Here we look to better understand the metric modal optimisation process in typical FCS samples in order to improve the accuracy and efficiency of the AO correction used in this thesis.

In chapter 4 we examine in detail the effects of aberrations on FCS results. Here we propose a method to study the effect of increasingly complex aberrations and asses the viability of AO correction to remove FCS bias in these situations.

In chapter 5 we bring together all the work of the other chapters in order to make FCS measurements in spheroids, multicellular aggregates used as tumour models. Here we use measurements of the hindered diffusion time from the FCS results to determine the volume fraction of hydrogel beads. By calibrating the change in volume fraction with stress and using AO, we make local measurements of pressure in spheroids, otherwise bias or made impossible by aberrations.

Chapter 2
Design and Implementation of an AO Microscope

In this chapter the design process and implementation of an AO confocal microscope will be explained. It must be said from the outset that an implementation of the confocal AO microscope already existed at the start of this thesis, designed and implemented by Leroux et al. [115,116]. At the beginning of this thesis the microscope was rebuilt and we took the opportunity to evaluate its performance and merit for the projects in this thesis.

Much of the optics and opto-mechanics were actually conserved from the previous project but the software and control of the microscope was built from scratch. Nonetheless, we intend to explain and outline the full development of this microscope. We took the opportunity to document and discuss the important elements of the implementation and explain the rationale behind its operation.

The original idea for this thesis was to develop a two-photon AO microscope to complement the confocal described in this chapter. Unfortunately this part of the project was never fully realised and was eventually put to one side in favour of further research using the confocal. As can be seen from the subsequent chapters in this thesis there was yet much to be learnt and gained from research with the confocal before moving to the two-photon setup. The control and software for the two-photon is the same as developed for the confocal, simply adapted to the different instruments.

Here the implementation of the microscope will be looked at in stages: Explanation of the sub optical systems involved, optical design and performance of the sub-systems and the system as a whole, detail of the software and control system, calibration and performance of the system.

2.1
Sub-systems of an AO confocal microscope

Including an adaptive optical device such as a DM, requires careful planning and implementation in order to achieve the best performance possible. It should be acknowledged that modern optical microscopes are already highly developed optical systems, care must be taken to actually not diminish the performance of the manufacturers optical design and lose all value of adding an AO system to the microscope in the first place. In order to get the best performance possible we look at the function and use of each of its parts before looking at the best manner in which to combine them. Below we look individually at the four sub-systems involved in putting together an AO confocal microscope: the microscope base, the confocal system, the scan system and the AO system.

2.1.1
The microscope base

The confocal microscope used in this thesis was designed around a commercial base; an Olympus IX71, an inverted research grade microscope. There are several optical components of the microscope which need to be considered in the optical design, primarily the tube lens. The tube lens of the microscope, its original (Olympus), has a focal length of 180 mm. Its position is fixed at a position 140 mm below (behind) the back aperture of the objective lens. The fact that this distance is fixed means that it will define the pupil conjugations of the microscope to the confocal system, which we will discuss later. The microscope also has a Piezo objective stage mounted on the objective flange behind the microscope objective (Mad City Labs) with 100 µm of travel. This adds an additional 10 mm to the tube lens objective distance which must be accounted for.

Zeiss 63X C-Apochromat	
NA	1.2
Focal length	2.611 mm*
Pupil Diameter	5.75 mm*
Nominal Mag.	63 X
Actual Mag.	68.9 X*
Parfocal Length	45.06 mm
Immersion Medium	Water (1.33)
Cover-slip Corr.	0.14 - 0.18 mm
Field Of View	25 mm

(a)

(b)

Figure 2.1 – Zeiss C-Apochromat Objective. (a) the objective specifications. * denotes a measured values, all others are quoted from the manufacturer. (b) an image of the objective.

The designated objective is a Zeiss 63X 1.2 NA W C-Apochromat. Because the objective is not matched to its microscope and hence its tube lens, this will affect its optical properties. Firstly, its magnification is no longer as stated its design tube lens length (165 mm; Zeiss) is shorter than that of Olympus (180 mm). This affects the nominal magnification of the objective, increasing it to approximately 69X. It is slightly unfortunate to use mismatched tube lens and objectives because Zeiss and Olympus objectives are corrected with their respective tube lenses. Normally the tube lens acts mainly for colour correction and fortunately we only intend to operate with a single excitation and fluorescence wavelength. However, axial colour is noticeable when focusing on samples in bright-field with oculars or a camera. If we were operating at other wave-lengths this effect would have to be accounted for somewhat.

Other than the objective and tube lens there are two windows on the optical path, one between the objective and tube lens and one after the tube lens before the image. These are of unknown material and approximately 5 mm thick. Their effect should be negligible except to elongate image and back focal distance of the tube lens. Finally there is a turning prism in the light path directly below the tube lens to direct light out of the side port of the microscope. The prism adds approximately 30 mm of unknown glass into the optical path between the tube lens and the image plane. This has a significant effect on the image distance of the tube lens. Since it is there by design we can safely assume it has no other effect on the imaging quality of the system.

The image distance from the side-port of the microscope is 102 mm and the objective has a field of view (FOV) of 25 mm at the image plane. This FOV in the focal plane with this objective corresponds to 397 µm. Given a tube lens clear aperture which is 32 mm for Zeiss microscopes and a 5.75 mm objective aperture it's simple to determine the maximum inter objective to tube lens length, L_{IT} before vignetting as:

$$L_{IT} = \frac{|\Delta \oslash| f_{TL}}{\oslash_{field}} \tag{2-1}$$

where $|\Delta \oslash|$ is the difference in the objective and tube lens clear apertures, $\oslash_{field}$ is the field diameter (given), and f_{TL} is the tube lens focal length. For this combination, the maximum value is L_{IT} 203 mm, far beyond the measured distance of 120 mm. Hence, there will be no vignetting due to this objective tube lens combination at the first image conjugation plane.

Another important parameter to determine is the axial position of the exit pupil of the objective and its apparent size. This is done using a camera and a lens. The lens must be chosen so that its combined power with the tube lens of the microscope will create an image of the pupil close to the size of the detector. Then a thin fluorescent sample is placed in the focal plane of the objective and it is excited using the wide-field fluorescence system of the microscope (Olympus, not described here). In this case the sample is 100 nm beads on a cover-slip. The lens (100 mm) is placed near the camera port of the objective on the optical axis, at an arbitrary distance less than 102 mm (the focal point of the microscope). The beads are brought into focus using the z drive of the objective and the camera is scanned along the optical axis to find the best image of pupil (Figure 2.2a). This image is also the circle of smallest diameter. Once this position is found its size can be measured by removing the objective and placing a ruler at the best focus with all the other components fixed (Figure 2.2b). The axial position of an object in best focus relative to objective flange can also be measured. We measured a diameter of 5.75 mm and an axial position very close to the flange of the objective. This diameter is close size of the opening of the back of the objective.

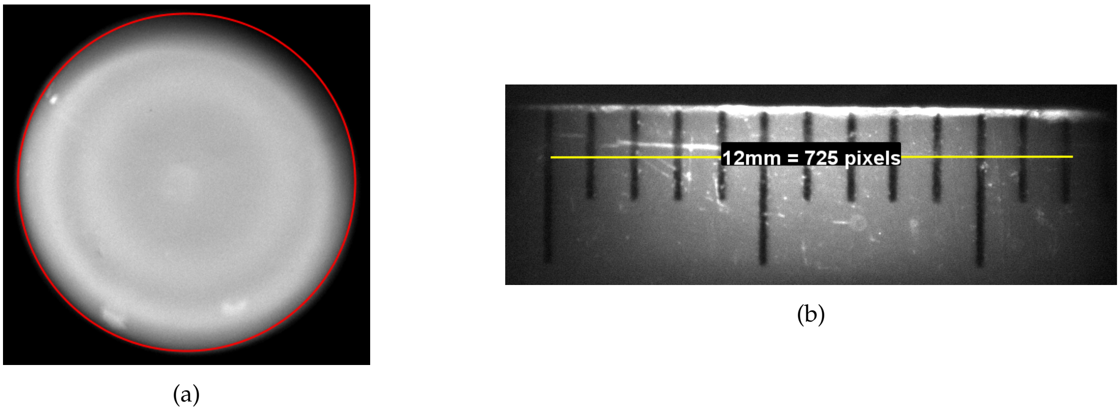

(a)

(b)

Figure 2.2 – Measuring the pupil of the microscope. 2.2a shows an image of the pupil in best focus on the camera. 2.2b shows an image of the ruler in place of the objective at the measured pupil position.

This measured diameter is counter intuitive: for a 2.61 mm focal length objective with 1.2 NA the calculated pupil diameter would be 6.26 mm. Our conclusion was that there are optics inside the objective altering its size and position leaving us no choice but to consider the flange of the objective lens as the axial pupil position to avoid vignetting of the confocal system. In reality there is always much compromise in the conjugate pupil position which we will discuss in the optical layout.

2.1.2
The confocal system

The confocal system used in this thesis is home-built using off the shelf parts from generic optical component suppliers. It consists of the excitation system, the detection system and their respective optical filter. The principal objective of the confocal system is increased spatial resolution in 3 dimensions by use of a spatial filter, namely a pinhole. The resolution gains are truly in three dimensions, contrary to popular belief that the goal is simply improved optical sectioning. There is a much greater potential for lateral, rather than axial, resolution gains for a decreasing pinhole size [117, 118]. However, a pinhole size much smaller than the lateral dimension of the PSF will obviously drastically reduce the collected signal intensity. Therefore a compromise must be found [119].

The size of the pinhole is very critical for FCS to ensure the observation volume is as close as possible to a 3D Gaussian function as is assumed by many FCS fitting functions. To ensure a Gaussian observation volume or PSF, given a diffraction limited confocal system, the detector size should be small and/or the objective back aperture should be slightly under-filled according to Hess and Webb [11]. For our system we have chosen a fixed aperture size, in the form of the entrance of a multimode fibre, with a diameter of 60 µm. We will discuss the justification of this choice in optical layout. Incoming fluorescence light is focused on to this via an achromatic lens.

Perkin Elmer SPCM-AQR	
Detector area	180 µm$^{(1)}$
Time Resolution	<250 ps
Dark Count	500 counts s^{-1}
Dead Time	60 ns
After Pulse Prob.	< 1.0 %
Linearity	98 % $^{(2)}$
Quantum Eff.	70 % @ 700 nm
Output	3.0 V TTL

Figure 2.3 – Perkin Elmer SPCM specifications. (1) detector area of diode, actual detector area is defined by fibre, (2) Typical at count rates below 1 M counts s^{-1}.

A commercial single photon counting module (SPCM) module is used for photon detection (Perkin elmer). SPCMs are ubiquitous in FCS due to the high sensitivity and sampling frequency required for FCS measurements. The main specifications are outlined in figure 2.3. The output signal is pre-conditioned so that the photons can simply be counted by square TTL pulses. The SPCM is ideal for FCS measurements due to its speed and sensitivity but unfortunately less than ideal for imaging purposes; the long dead time means a absolute maximum count rate of $\simeq$ 20 µs^{-1} so to have any contrast the pixel dwell times must be several µs, in a regime where the pixel intensities are acquired sequentially.

The excitation is provided by a diode pumped solid state laser (Cobolt SE, Sweden) at 561.2 nm. This source was chosen primarily as it is a common wavelength for excitation of fluorophores used in biology such as mCherry. Another very useful stable fluorescent molecule, used extensively in this thesis, is Sulforhodamine B, which has a peak fluorescence excitation at approximately 550 nm. Solid state lasers provide a cost effective source that is stable in both frequency and power, essential for FCS measurements. The laser temperature is regulated internally by the controller and the power is tuneable from 2 to 30 mW via USB control.

Unfortunately, past experience in the team was the laser was not stable enough to be coupled in to a single mode optical fibre for spatial filtering, so we did not attempt this again. This would inevitably mean small residual aberrations on a non-common path of the microscope. The laser was expanded 5X in free space using a Keppler telescope comprised of 2 achromats (f = 30 and 150 mm, Thorlabs). Only the centre portion of the beam would be used, this served two purposes; reducing the power and improved intensity profile of the laser beam. The laser was further attenuated by a 1.0 neutral optical density filter plus a variable neutral density filter (both Thorlabs). The USB control of the laser power was a nuisance as the driver was not 64 bit compatible and involved a second dedicated PC. Given the laser was out of warranty at the time, the manufacturer would only update the firmware for a substantial fee and turnaround time of 3 weeks, requiring the entire system to be dismounted and shipped. Despite all the drawbacks the source was adequate for the experiments in this thesis.

The excitation and fluorescence elements were brought together on perpendicular axes at the dichroic filter (Chroma). The filter reflects light at 561 nm at 45° incidence. This ensemble of parts constitutes the confocal sub-system and is the essential part of operation for FCS measurements. Given a suitable choice of lenses and combined with a microscope objective it would form a confocal microscope independently. Before discussing the details of its optical design however we will examine the additional components added to the confocal system to increase its functionality.

2.1.3
Raster scan imaging

A confocal system such as described above excites and detects fluorescence at a single point in (x, y, z) space. This is all that is required for FCS measurements but when working with small structures such as cells, it is impossible to know if the focus is positioned accurately. As such, the microscope was designed with a laser scanning system in order to create images of the objective focal plane. This would also serve to be used for some fluorescence fluctuation techniques which make use of spatial information raster scanning can provide [115,120].

The raster scanning of the laser beam was facilitated by a pair of galvanometric mirrors (GMs) (Cambridge Instruments, USA). The mirrors are mounted at 90° to each other to provide beam scanning along the x and y axes of the objective focal plane. The principal of operation is that a tip or tilt induced in a collimated beam will translate into a spot displacement in the focal plane of the subsequent lens (Fourier plane). GMs are positioned at a plane conjugate to the pupil plane of the objective. These conjugate planes must be telecentric; where the chief rays of all possible image heights intersect. This is essential to avoid vignetting of the beam.

Since there are two scanning mirrors, one for each axis, it is difficult to mount both GMs at a telecentric conjugation. There have been many solutions to this problem, an overview can be found in [121]. However, this is certainly not exhaustive. The solution in this case is the so called compact scanner where the two mirrors are mounted as close as possible to one another along the optical axis. As such, in general neither mirror is at the telecentric plane and it lies somewhere in between the two. In terms of imaging this solution is far from ideal because of vignetting, and especially so in terms of imaging with adaptive optics, which will be discussed later. However the goal of the imaging system here was primarily for accurate FCS volume positioning so this solution was considered adequate. Moreover, the compact arrangement was conveniently already in place from an earlier implementation of the microscope [115,116,120,122].

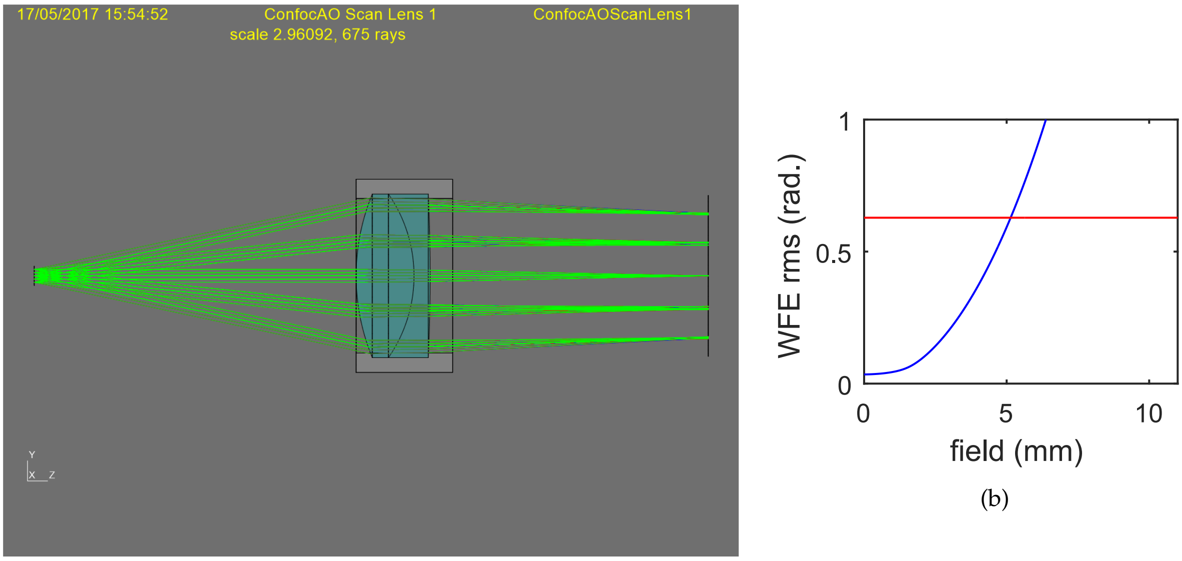

(b)

(a)

Figure 2.4 – Performance of a single f=60 mm achromat as a scan lens. 2.4a show a ray tracing diagram plotted in LASSO. 2.4b shows the wave-front error (WFE, blue) at various radial positions across the field of view at the image plane, where the image plane position has been optimised. The red line marks the WFE corresponding to a Strehl of 0.9.

An important aspect of the design of a raster scan system for a confocal microscope is the optics that are used immediately after the scan system. These optics will serve two purposes; to create a conjugate image plane for the microscope base, and secondly half of the telescope which conjugates the telecentric plane of the objective pupil. This is challenging because of the magnification involved and thus the large field angles at one end. The magnification of the beam size must be large as the galvanometric mirrors are sized purposely small (< 4 mm) for low inertia, and thus higher frequencies. We also assume that the microscope objective and tube lens combination create a high quality plane image up to the specified field size of the objective. Therefore the image created by the scan lens must be as flat as possible and free from aberrations. This is not a trivial task but thankfully there has been much research into such lenses for hundreds of years, in the form of ocular lens, which demand very similar characteristics [123].

We used a ray tracing software solution, LASSO (IPAG, Université Grenoble Alpes), to evaluate the performances of various lens systems as scan lenses. The previous solution for this system was a f = 60 mm achromat (Thorlabs, USA). This will provide very good performance on axis, perfectly sufficient for FCS measurements but the performance very quickly drops off for any field as shown in figure 2.4. Here it can be seen that, even without spatially varying sample aberrations, the area of the FOV over which the image would be diffraction limited is very small. Since the performance here is below par we decided to investigate other solutions for a performance boost. Similar performances were observed in Negrean et al. when testing a single achromat as a scan lens for a raster scan system [124]. They also investigated several other scan lenses including a custom prototype with exceptional performance. We investigated the simpler of these designs.

One notable design tested by Negrean et al. was a simple Plössl lens type scan lens constructed from two off the shelf achromats. The Plössl design is ubiquitous in eye piece design for microscopy and astronomy [123]. The function of a scan lens is in fact very similar to that of an eyepiece; to conjugate a telecentric plane to a fixed distance in space with as large a field a possible and minimal aberration. In the case of the eye there is a major advantage of a curved image plane which drastically increases the FOV. A scan lens must create a flat field.

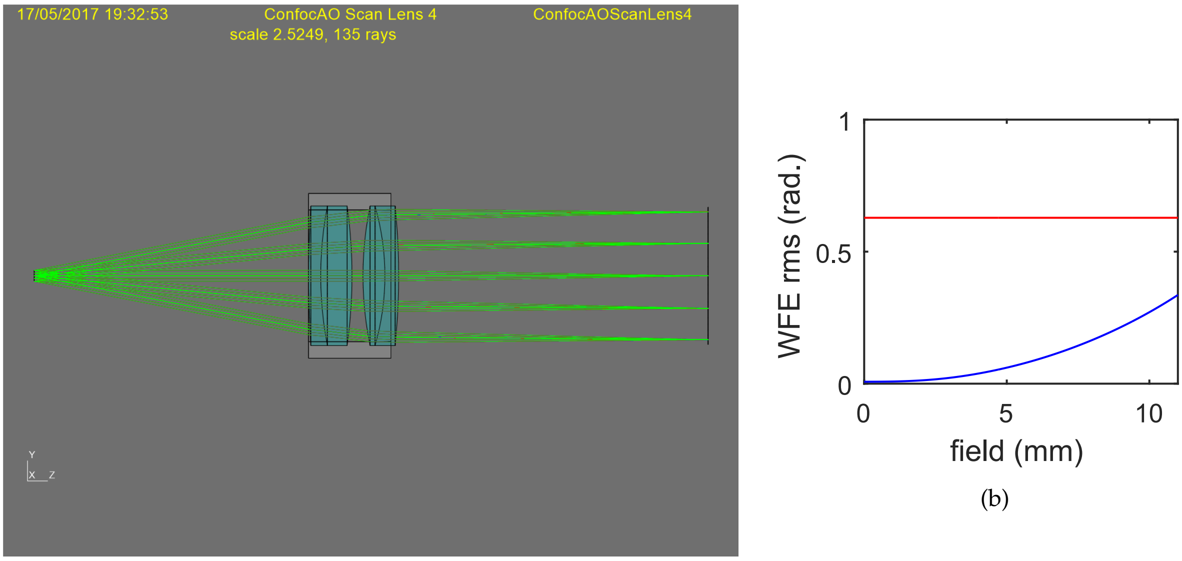

(b)

(a)

Figure 2.5 – Performance of a compound f=60 mm achromat as a scan lens. The lens evaluated here is a combination of f=150 mm and 100 mm achromats (Thorlabs). The first lens is inverted to its usual orientation. 2.5a show a ray tracing diagram plotted in LASSO. 2.5b shows the wave-front error (WFE, blue) at various radial positions across the field of view at the image plane, where the image plane position has been optimised. The red line marks the WFE corresponding to a Strehl of 0.9.

We adapted the design combining two positive doublets (f = 100 mm and f = 150 mm, Thorlabs) to form a lens with a nominal focal length of 61 mm. The lenses are placed with their infinite conjugation sides facing each other a few mm apart, this was optimised in LASSO. As can be seen in figure 2.5 the performance improvements over the simple achromat for the same conditions are impressive.

It may be apparent from the figures that the performance is superior to that measured by Negrean et al. for similar designs but the field angles in our case are smaller (vignetted here by the scan lens mount, $\oslash$ = 21 mm), and the input beam diameter is 2 mm, as opposed to 3 mm in their case. This performance is sufficient for our system giving diffraction limited resolution across the entire FOV, in theory. The axial position of the lens along the optical axis after the scan system is not yet determined as it is defined by the objective pupil / tube lens combination and must be found *in situ*.

2.1.4
Open Loop AO system

With the microscope base, confocal system and raster scan system chosen a full confocal microscope can be put in place. However the goal of this project is to add one more piece to the puzzle, an AO system. Here the AO system was already chosen for the project, an ALPAO DM 97-15.

The DM must be calibrated in place to ensure the best optical performance. This is important as the system will function in open-loop, or feed forward operation. That is to say without direct feedback from a wave-front sensor, as discussed in chapters 1. There are a wide variety of methods to calibrate wave-front shaping devices, with some developed specifically for microscopy [61,77] but we opted for a very classical approach using a SHWFS (ALPAO, France).

The SHWFS is placed on an optical path independent of the microscope, using the confocal laser as a light source. This path can be switched by means of a flip mirror and will be described in more detail with the other optics in the next section. One particular point which is worth mentioning for the alignment of the SHWFS is that the plane of the lenslets must be very well conjugated with the plane of the DM surface. This is important as the SHWFS can be sensitive to intensity variations which bias the wave-front measurements [125].

A simple trick to finding a plane conjugate to the DM surface is to understand that to have an shape deformation which influences solely the phase of the light, one needs to be at the pupil plane of an imaging system. If this is not the case, deformation of the light beam will also result in a change in contrast, being at a plane between the image plane and the pupil plane. This effect is easily noticeable using a DM to align the SHWFS as a deformation of the DM will not induce a change of intensity of the SHWFS spots only at a conjugate plane. We therefore move the centre actuator of the DM to induce a phase change that will produce a noticeable and identifiable contrast profile when outside the pupil plane.

Another important aspect of the DM calibration is to know the exact size of the pupil relative to the DM. This is important to know the phase influence of each actuator on the system pupil, which may or may not be equal in size to the SHWFS or DM pupil. Ideally $\oslash_{\text{SHWFS}} > \oslash_{\text{DM}} > \oslash_{\text{System}}$ given their respective magnifications, but as close to equal as possible. The size to the system pupil, defined by the objective, is measured in the section above. Its size on the DM is then calculated given the magnifications. In our case this was confirmed using LASSO. Ideally the SHWFS would see the DM in the objective pupil [77] but this was not feasible in our case.

2.2
Optical Layout and implementation

Now that we have considered each of the components of the components of the optical system we have to consider how to best put them together to get the best performance possible. First we must consider a general order of each of the components above, then the optics of the connecting telescopes must be chosen to provide the correct magnification for the pupil and the pinhole. Finally, all the components must be arranged in a configuration that provides the practically smallest footprint. There is one major condition on the placement of a DM in a microscope; it must be located at a conjugate telecentric plane to the microscope objective, and hence, the scan system also. Since our microscope is fully custom, we have two choices for this, before the GMs or after them (figure 2.6). Each has their advantages and disadvantages but both have been used successfully in AO implementations. We note here that placing the DM at the pupil plane

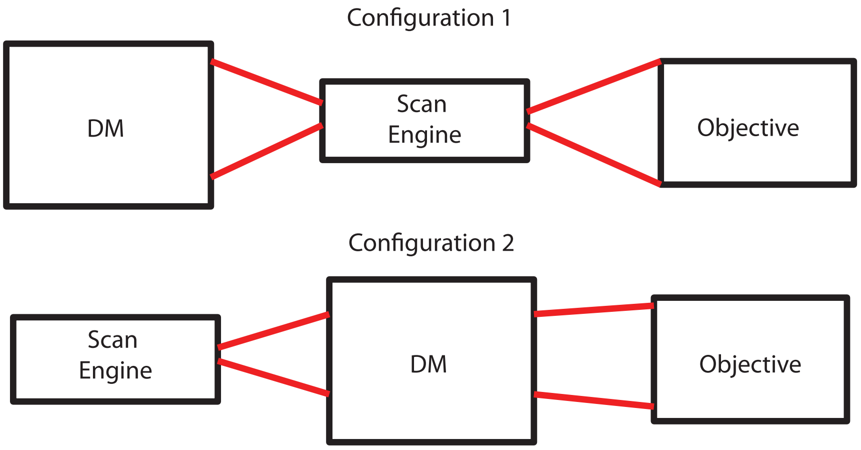

Figure 2.6 – DM configuration options in the confocal system.

is the classical setup for an AO system as it will influence the phase at any field position. Hence, often the AO correction is only valid for a single point and drops off quickly for positions around it [102, 116], or the correction is an average over a defined area [29, 81]. Recently, much work has been done for so-called conjugate AO or multi-conjugate AO systems where the DM is placed at a location out of the pupil plane [126,127] or at multiple pupil planes [128]. This can provide advantages such as increased isoplanatic patch [126] but generally requires multiple time the number of degrees of freedom as pupil conjugated systems and thus add much complexity and cost to the system [129].

Points to consider when choosing the better configuration are:

- relative magnification,
- system aberrations,
- the scan system geometry,
- physical constraints,
- ease of implementation.

The first item to consider is the relative magnification. DMs vary in size and their pupil must be accurately magnified on to the objective pupil in order to obtain best performance. If the magnifications are extreme; the telescopes can end up taking large amounts of real estate, if it's after the scan system the telescopes can introduce more field aberrations. In an ideal world the pupil sizes would be as close as possible, simplifying the optics considerably [130].

If the raster scanner is of a compact geometry it may be advantageous to place the DM after it, such that the DM conjugation be stationary on the objective pupil. In this way the aberrations would not change at all due to beam wandering at the pupil. If a commercial system were to be used, there would generally be no choice but to place the DM between the scan system and the microscope unless the DM could be placed on the laser beam line entry somehow. If the DM were to be placed after the scan system then each of the optics chosen to conjugate the DM would have to be well corrected for the full FOV of the microscope also which could add a lot of extra complexity.

The compromise chosen here was for some simplicity, to place the DM before the scan engine. It would therefore remain similar to the previous incarnation of the AO microscope. This allows for a lot of simplicity when choosing optics as they only need be well corrected on axis. However, this also creates a headache for aberration correction when imaging as the image of the DM at the objective pupil will move about relative to the microscope pupil as neither GM is perfectly conjugate with it.

Once the order of the optical sub-systems is decided the connecting telescopes must be chosen to achieve the correct magnification of the PSF on the pinhole and at the same time, correctly magnify the

	ConfocAO Optics			
	Focal Length	Beam Size	Magnification	PSF FWHM
Objective	2.61	(Pupil) 5.75		0.5
Tube Lens	180		68.95	
Scan Lens	60	(GM) 1.92		34.47
L1	30		34.47	
L2	200	(DM) 12.78		17.24
L3	250		43.1	
L4	50	2.56		21.54
L5	150		129.3	
Pinhole			129.3	64.63

Figure 2.7 – Optics in the ConfocAO system listed with the size of the optical beam at each element and the PSF and magnification where a conjugate image plane appears before the element.

objective pupil on to the DM and the GMs. Most of the magnifications used in the original manifestation of the microscope were maintained [115, 116]. The only real changes were the scan lens and the telescope magnifying the laser. Nevertheless we assessed the entire setup using LASSO to validate the design.

As mentioned earlier, the presence of glass surfaces of non-negligible thickness (other than the lenses) can serve to alter significantly the telecentric conjugations. Therefore calculating the exact positions of the telecentric planes is not trivial and should generally be done in a ray tracing software [130]. Of course there are techniques to find the telecentric planes *in situ* [121] but this should not be left to chance in a complex optical system as they could place them outside the intended mechanical constraints, calling for a redesign later.

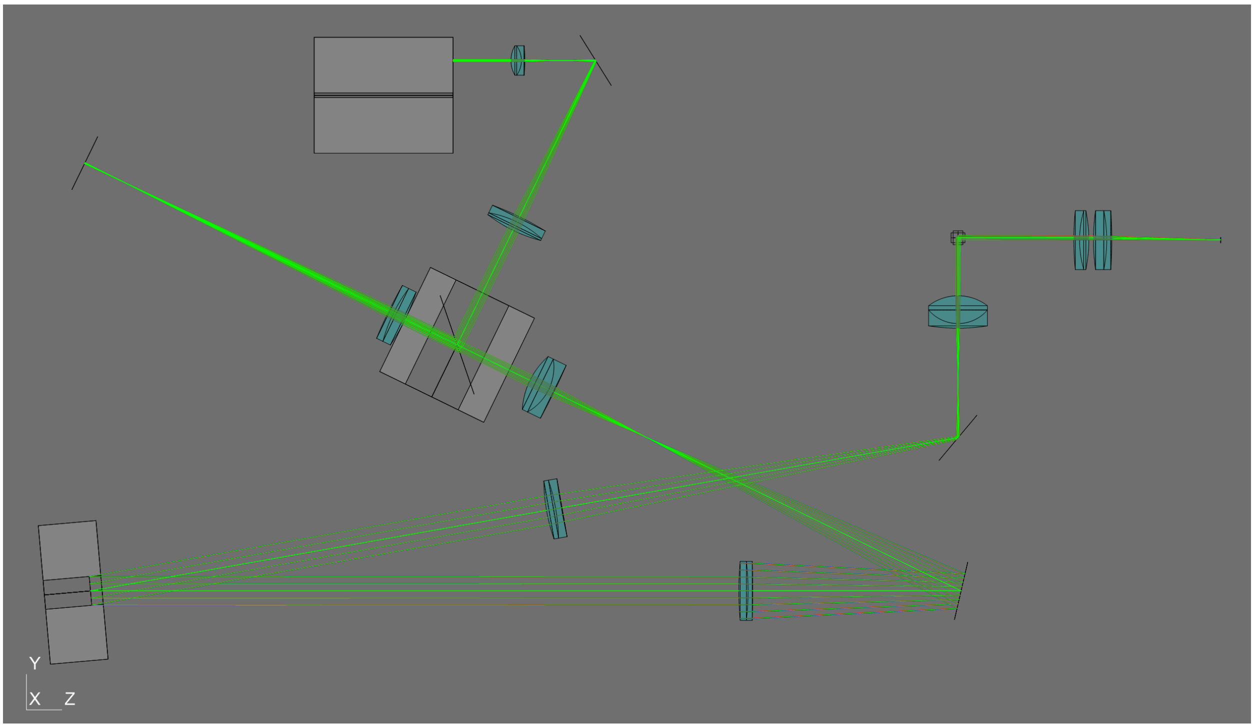

Figure 2.8 – Layout of the confocal system in LASSO from the source up to the scan lens. The pinhole is also simulated here by back tracing the rays from the dichroic element. To evaluate the performance the excitation and imaging paths are evaluated separately

Figure 2.8 shows the evaluated layout of the confocal system until the scan lens. This is the part of the system that will be placed on the breadboard. The SHWFS is placed directly on the optical table and it picks off the beam after the scan lens. We analysed the performance of this system in LASSO and found a maximum wave-front error of 0.48 µm RMS, which consisted mostly of spherical aberration. This is easily corrected by the DM. The wave-front error of the detection path is slightly less than this which indicates non-common path errors. This was expected but fortunately the difference is low enough that it should be negligible. Therefore we should expect near diffraction limited performance for the system, if it is well aligned of course.

2.3
Control and Acquisition

The confocal microscope represents the combination of a significant amount of hardware that must all function synchronously. It must also be adaptable to a variety of experiments which can be programmed by users who may not be very familiar with data acquisition or AO. Therefore the program to run the microscope needs to be carefully planned and implemented in a logical way such that the base program can be interacted with in the same way to perform any experiment.

Previously the microscope was controlled in Matlab (Mathworks) via a series of functions. This allowed a GUI to be built to perform basic acquisitions which was simple and opened up the microscope to a wide variety of users. However, more complicated experiments required these functions to be modified internally or copied in order to avoid altering the 'master' files. This inevitably led to many functions which did more or less the same base functions but slightly modified. This all became difficult to manage when dependant functions were modified and suddenly many of the previous experiments could no longer work. Furthermore the GUI could not be used for any acquisition that was not 'standard' and many functions could end up fighting for control of the same device occupied elsewhere, thus crashing everything. A new software solution needed to be found to organise and simplify things.

It was decided that the microscope control be totally overhauled to create a control engine that was:

- Versioned
- Object based oriented
- adaptable to any experiment
- transferable to new hardware with ease
- user friendly (a very perceptive term!)

Matlab was quickly chosen to be the base language for the engine as it was ubiquitous in the research team at the time, was the previous base for some microscopes in the lab and was also the base for ACE. Matlab supports object oriented programming which would allow for the implementation of a class based structure. With the class based structure a hierarchy could easily be implemented and with objects the number of instances of any objects can be easily controlled. Objects can be shared with many functions or other objects via handles while keeping only one instance. This is highly advantageous, a simple example is changing a value in a GUI for the number of pixels in an acquisition object. When the value is changed in the GUI the object will update and any other objects linked to that object will immediately see the change.

This leads to listeners which can be added to properties to carry out certain function if for example the DM moves. Or methods, functions inside classes that can for example check properties to see if they are valid before changing them. The advantages are far too numerous to list here, plenty of literature on object oriented programming can be found on the Matlab website among other places.

We also implemented a versioning software for version control and to allow superusers to have their own branches of code for more complex experiments and development. This was implemented using Git for windows and used a remote server as the repository (GitLab). This allowed for back compatibility should any problems arise or if redoing experiments demanded old versions of the software, which could be switched instantly using the GUI functions. This also added backup security with multiple off-site backups.

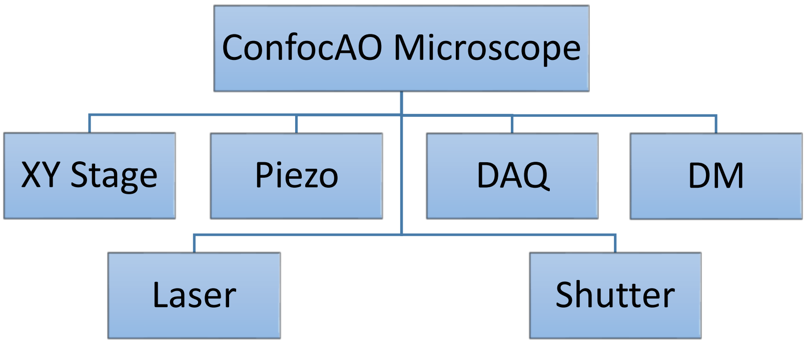

Figure 2.9 – ConfocAO microscope devices

2.3.1
Class hierarchy

At the most basic level the microscope has pieces of hardware that are connected to the PC, the controlling device. Each separate device would be designated its own class and then the ensemble would be managed by a class called the microscope. This hierarchy can be seen in figure 2.9. The key feature here is that this structure is as generic as possible and could be adapted to any set of devices. This is the set designated for this particular microscope so we call it ConfocAO after the ANR project which created it.

Each class would interface with the hardware, manage its particular properties, and implement methods to control the device. The microscope class would then manage the ensemble and manage any properties of the devices that were specific to this implementation.

We have two distinct types of acquisition for this microscope, FCS and imaging. These acquisitions will acquire data in a similar manner but given that they handle the output data very differently we decided it best to have separate objects for each acquisition.

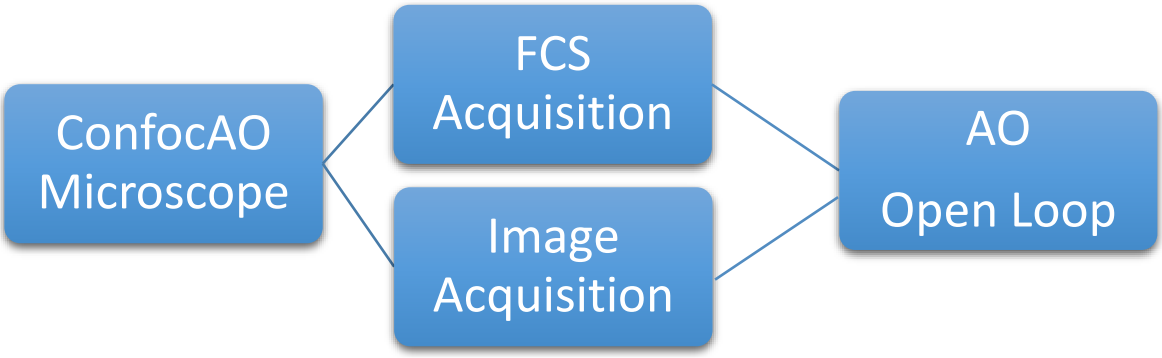

Figure 2.10 – Acquisition Class in the Microscope engine. Either acquisition can take control of the microscope but the microscope will only interact with one at a time. The AO loop class then interacts with either of the acquisition classes depending on the metric required.

2.3.2
FCS Acquisition

The FCS acquisition class is in fact the simpler class to put in place. It's simply point and shoot. The GMs are set to a nominal position and the counter acquires data over a certain interval, t, at sampling intervals Δt. Generally, the FCS data is not acquired all at once and the data is acquired at several Hz. This is to avoid filling the buffer and also to facilitate a real time display of the data acquisition.

The autocorrelation of the data is done using the bin and multiply method of Wohland et al. [131]. Each incoming data set is autocorrelated and the autocorrelation over the entire interval is determined as the mean of the set of auto correlations. This only works for $\tau \ll t_{interval}$ and thus serves only as a real time display. The photon counts are simultaneously saved to a buffer for a full autocorrelation of the entire data set post acquisition. The autocorrelation algorithm was written in C++ as Matlab is very badly optimised for multiple for loops which are inevitable here. The C++ implementation is over 20 times faster than the best optimised Matlab algorithm. There are more recent algorithms for autocorrelation that can be much faster [132–134] but implementation of such algorithms was considered beyond the scope of the thesis. Here we have a solution with real time display and no data loss with the post-processing algorithm.

The FCS acquisition class also handles simple fitting of the FCS data. Here we implement a simple least squares fit assuming normal 3D diffusion for a single species [2]. For more complicated fits we exported the autocorrelation functions to QuickFit 3 (DKFZ, Germany) [135, 136].

Due to the limitations of the data acquisition toolbox in Matlab, the data acquisitions are always in "Free-run" mode. That is to say that the acquisitions occur continuously in a background process and listener executes a function every time data is ready. This is not ideal when we would like to have other operations in between acquisitions, for example, changing the DM shape. Here the acquisition in progress must be rejected to be sure the demanded operation does not overlap with the acquisition. This is inefficient but since stopping and starting a task in the data acquisition toolbox takes over 0.5 s, it is generally the fastest method. This necessitates timers for every auxiliary device in the system for which an acquisition is invalid if a timers value is less than a threshold i.e. the microscope was in a transitory state.

2.3.3
Image Acquisition

The image acquisition class acquires data in much the same way as the FCS acquisition but here there is also spatial data to be processed. The input to the GMs must be patterned to produce an image and the output intensities must be correctly attributed to the GMs voltage, and hence the spatial position at the sample.

Since the images can be large, it is generally inefficient to feed the position vector for an entire image to the buffer and wait the length of time for the acquisition. Some acquisitions may take a number of seconds and waiting this long between acquisitions can be dangerous for the sensitive photon counting equipment i.e. if the signal during the acquisition is high enough to damage the equipment, we won't actually have feedback on this for several seconds. Also, for long term acquisitions it is advantageous for the user to be able to see the acquisition in progress even if the image is not complete.

Therefore we created a GM patterning subclass which handles all these issues. This creates a master pattern of GM positions required to create an raster scan image. This pattern, a vector of positions, must also include the pattern to finish a line and return to the start position for the next line. In general here we use a classic unidirectional sawtooth pattern for the images. This is to say the fast GM samples while moving in one direction only and then returns to the start position of the line as quickly as possible. We set the slow axis to move constantly from line to line, rather than stepping, as the fast axis samples in the perpendicular direction. This creates a very slight tilt with a slope of 1 pixel but we believe this is better than the jitter which could be caused in the GMs due to discrete steps.

The GMs have analogue position feedback signals which can be captured to determine the GM position. This can be useful to create very accurate pixel maps for the intensity data. However, capturing these requires using the analogue inputs of the DAQ, and for each analogue input channel used the sampling frequency is halved as there is only one A/D converter on the DAQ. Despite this nuisance, we can still use these inputs to calibrate the GMs to accurately create raster scan images for all sampling frequencies, pixel sizes and number of pixels.

To calibrate the GMs we need an accurate profile of the step response. The step response can be calibrated and recorded using procedures outlined by the manufacturer in the manual. We measured a step response of 105 µs for an input corresponding to the maximum FOV of the microscope. Using this we can create raster scan patterns such that the GMs move at constant velocity in the image region. These patterns are then verified for a range of conditions using the position sensors of the GMs.

Once the GM patterns were matched to the speeds we found the positions extremely repeatable and accurate (compared to the GM position sensor). We therefore deemed it unnecessary to add the complexity of a position feedback for the imaging. If the project demanded some more ambitious imaging there are some significant gains in efficiency, reduced photo-toxicity and photo-bleaching, and image quality that can be made with GM position feedback through regimes such as circular scanning (D. Debarre, private communication, and [137]).

2.3.4
Open loop AO control

The most complex part of the software engine is the part which controls the AO loop. This class must use and interact with all the previously described objects. Having objects defined for all our acquisition needs makes the design of this class much simpler. First we will describe the general strategy for AO correction in our microscope and then we describe how we implement this.

There are two algorithms which we wish to use in this microscope for the AO loop, both sequential metric modal optimisation algorithms [73]. The strategy is to take a number of measurements of an arbitrary metric obtained from an acquisition while applying a known aberration mode, which we previously calibrated. These measurements are then fitted using a function to determine the optimum amplitude of each mode and finally the calculated correction is tested. The algorithm can be applied in one of two sequences: 1 flat measurement followed by p measurements per mode up to N modes (the so called pN+1 algorithm [78]), or 1 flat measurement per mode plus p measurements per mode (N(p+1) algorithm). The latter is slower obviously but allows the calculated correction of each mode to be checked in turn as the sequence progress. For both algorithms the modes would be tested in sequence (user defined), which cannot be changed on the fly, for simplicity. Also the number of measurements is defined before beginning the sequence.

One feature which was important was the arbitrary correction metric and fitting algorithms. We intended to examine the application of a number of metrics for FCS measurements (chapter 3) so being able to adapt the class was important. With the acquisition classes in place this was simpler: the AO class would start an acquisition of choice using the classes in place and then simply 'listen' for a new output. The AO class then records the metric of interest and sets the DM bias for the next measurement. A pseudo algorithm would look like this:

Algorithm 1: pN+1 Pseudo Algorithm

```
M_0 ← Get Metric (metric value with flat DM)
for $mode$ ← $1$ to $N$ do
    for $meas$ ← $1$ to $p$ do
        Apply Bias($b_i$)
        M$_{(i)}$ ← Get Metric
    end
    $a_N$ ← Get correction value(M$_{(i=1,\dots,p)}$, $b_{(i=1,\dots,p)}$)
end
Apply correction
M$_{NEW}$ ← Get Metric (metric value with flat DM)
if $M_{NEW} > M_0$ then
    Keep correction
else
    Discard
end
```

If the corrections are calculated using arbitrary metrics then the user can define any metric desired based on image or FCS acquisitions. Generally a quadratic function can be used to fit any metric in the vicinity of its maximum [73,74,78]

$$M = M_0(1 - \beta\sigma^2) \tag{2-2}$$

where M_0 is the metric value in the absence of aberrations, σ is the RMS amplitude of the applied aberration on the DM, and β is the sensitivity, the amplitude of the quadratic term. This is used in general but any function can be defined by the user to fit the aberration.

2.3.5
Closed loop AO control

Figure 2.11 – Closed loop class diagram. The closed loop class interacts mainly with the DM and SHWFS, and occasionally with the microscope class to open the laser shutter for example.

The SHWFS and DM were controlled using ALPAO Core Engine (ACE) software. As part of the development team for ACE the author had the opportunity to develop some procedures and algorithms specific to open loop system calibrations. We shall not discuss a detailed hierarchy of the ACE class structure here. ACE's object oriented implementation means that we could easily integrate some of its structure into the class structure of the microscope engine itself and at the same time, share these objects with the higher level controls of ACE, such as LOOP, a class for closed loop control of the DM.

One of the biggest advantages of a class structure not yet discussed here is inheritance. What this means in practise here is that we could take the LOOP class of ACE, which is protected and hidden code generally, and included it directly in our own custom LOOP class for our implementation. Our code would inherit all the properties and functions already coded in ACE and still protected but allow us to add our methods with them, without needing to redefine the entire class. Even if there is a method in place which we would like to customise or replace we simply rewrite it, with the same name and arguments, and it will immediately be recognised as its replacement code.

Therefore our custom class inherited all of ACE's methods already defined and we need only define some special methods and properties specific to our microscope, such as, alignment functions, Zernike calibrations and laser and shutter control.

2.4
Calibrations and performance

Now that all of the elements of the microscope are in place the system must finally be calibrated in a number of ways for best performance. We shall go through these in their logical order, the order in which they should be carried out.

2.4.1
Zernike command matrix calibration

First on the list is calibrating the DM in the system. It is important to calibrate a good DM flat as it required to finish the alignment of the microscope and complete other calibrations. We use the ALPAO SHWFS to calibrate the DM which is positioned as described in the optical layout, with the flip mirror in place.

First order of business is to calibrate the SHWFS itself. The geometry of the SHWFS is set and calibrated at ALPAO so we shall not trouble ourselves to recalibrate the sensitivity of the lenslets here (the distance from the lenslets to the detector). This is an important geometry to be well known, if required a procedure for this can be found in the PhD thesis of CE Leroux [138]. Here we will only concern ourselves with getting a reference wave-front for the SHWFS to account for the optical system.

There are many procedures to get a reference wave-front but the important point is have a reference which is virtually free from aberration. As we did not want to introduce extra elements or sources in the system we used a simple procedure developed in this case by CE Leroux [114–116]. A piece of paper was placed at a focal point of the system between the DM and the SHWFS such that the SHWFS could see it clearly. This would obviously produce a speckle pattern but with the advantage that the aberration information of the source beam would be mostly lost in the process. Then the speckle can be effectively removed using the scan mirrors to scan the spot over a small angle while taking the reference image with the SHWFS. Care must be taken that frequency of the scanners completes a full scan at an integer multiple faster that the integration time of the SHWFS image, otherwise this will create a bias of the spot positions [138].

This image will provide the reference positions for the SHWFS centroids. Using ACE the reference positions can be recorded as a vectors of x and y positions. The centroiding generally used by ACE is simple centre of gravity (CoG) calculation in the window of each SHWFS lenslet. This algorithm is chosen for speed which is of highest importance generally in AO systems for atmospheric turbulence calculation. Here we took the opportunity to integrate a more precise matched filter algorithm into ACE for increased centroiding precision [139–141]. The algorithm in question is the so-called iteratively weighted CoG [142] and is similar to the CoG in the first instance but the pixels are then weighted against a Gaussian model of a spot centred on the lenslet. The position $p(x,y)$ is:

$$p(x,y) = \Big(\frac{\sum xI(x,y)W(x,y)}{\sum I(x,y)W(x,y)}, \frac{\sum yI(x,y)W(x,y)}{\sum I(x,y)W(x,y)}\Big) \tag{2-3}$$

where I are the pixel intensities, x and y are the local pixel coordinates, and W is the model Gaussian spot, with variance σ^2, and;

$$w(x,y) = \frac{1}{2\pi\pi^2} e^{\frac{1}{2\sigma^2}(x-x_c)^2} e^{\frac{1}{2\sigma^2}(x-x_c)^2} \tag{2-4}$$

The process is then repeated but the model is shifted by the previous result. This is repeated until the model and calculated centroids converge. Normally this occurs within 2 to 3 iterations depending on the signal and choice of FWHM for the model. This centroiding algorithm is now integrated as an option in the commercial version of ACE.

Once the spots are found the slopes are calculated in ACE knowing the physical geometry of the SHWFS. If closed loop control is the goal, there is no need to proceed further than this, the DM can be controlled simply by minimising the slopes in the SHWFS knowing the influence of the DM actuators on the SHWFS slopes. This leads us to the influence function measurement of the DM. Each actuator is pushed in turn and the deviation of the SHWFS slopes from the slopes in DM resting position is recorded. This makes up the so-called interaction matrix $\boldsymbol{M}_{int}$ where;

$$\boldsymbol{s} = \boldsymbol{M}_{int}\boldsymbol{c} \tag{2-5}$$

where $\boldsymbol{c}$ is a vector of DM commands and $\boldsymbol{s}$ is a vector of SHWFS slopes.

Setting aside the DM for the moment, as we are not only interested in a flat DM surface, we also wish to create a command matrix for the DM to create known amplitudes of Zernike modes. This requires a reconstruction of the wavefront in a Zernike modal decomposition. This is constructed in much the same way as $\boldsymbol{M}_{int}$: the influence of a Zernike mode over a unitary pupil with a unitary amplitude on the SHWFS is evaluated. This is where it is important to know the pupil mask to use in software which corresponds to the size of the system pupil on the SHWFS. SHWFS lenslets that fall outside this mask should be ignored as the amplitude of Zernike modes beyond the unitary pupil can be very large. Attempting to use DM commands to create such slopes is a waste. The function of each Zernike mode over the unity pupil is evaluated in turn to determine its influence on the SHWFS slopes. Here we get:

$$\boldsymbol{s} = \boldsymbol{M}_s\boldsymbol{z} \tag{2-6}$$

where $\boldsymbol{z}$ is a vector of amplitudes of Zernike modes used and $\boldsymbol{M}_s$ is the translation matrix from Zernike modes to SHWFS slopes. Having calculated $\boldsymbol{M}_s$ and $\boldsymbol{M}_{int}$, we can construct the command matrix to create Zernike modes on the DM, $\boldsymbol{C}_Z$, which is:

$$\boldsymbol{C}_Z = \boldsymbol{M}_s^{-1}\boldsymbol{M}_{int}^{-1} \tag{2-7}$$

As the matrices $\boldsymbol{M}_s$ and $\boldsymbol{M}_{int}$ are not square, their inverse cannot be computed directly. We calculate the inverse using singular value decomposition (SVD) method where we obtain,

$$SVD(\boldsymbol{M}_{int}) = \boldsymbol{USV^*}, \tag{2-8}$$

where $\boldsymbol{U}$ is the unitary complex matrix, $\boldsymbol{S}$ is a diagonal matrix where the diagonal values are the square root of the eigenvalues of $\boldsymbol{M}_{int}$ and $\boldsymbol{V^*}$ is the complex conjugate unitary matrix. This is useful as the relative power of the eigen modes of the DM can be evaluated and its eigen vectors $\boldsymbol{UV^*}$ can be used to visualise the eigenmodes of the DM in SHWFS space. This can be a very useful tool to filter DM eigen modes which have very low eigenvalues. These modes would contribute little to the wave-front but use much of the DM stroke or power. In the case of this system it can be seen that the eigenvalues for modes above 86 are orders of magnitude weaker than the rest of the spectrum and thus are filtered. This is expected as the entire surface of the DM is not fully used. The pseudo inverse of $\boldsymbol{M}_{int}$ can then be constructed as

$$\boldsymbol{M}_{int}^{-1} = \boldsymbol{V^*S'U^T} = \boldsymbol{C}_{dm}, \tag{2-9}$$

where $\boldsymbol{S'}$ is diagonal matrix with the filtered eigenvalues (filtered modes = 0) and $\boldsymbol{C}_{dm}$ is the control matrix for the DM. The same procedure can be used to calculate $\boldsymbol{M}_s^{-1}$, and hence $\boldsymbol{C}_Z$.

Using $\boldsymbol{C}_{dm}$, the best flat of the DM can now be determined by reducing the wave-front error, $\Delta\boldsymbol{s}$, which correspond to the residual SHWFS slopes

$$\boldsymbol{c} = \gamma\boldsymbol{C}_{dm}\Delta\boldsymbol{s}, \tag{2-10}$$

where γ is the loop gain. A γ constant of 0.23 is chosen as we know from simply from trial and error that it produces the wave-fronts with the lowest error. This is repeated for several iterations to achieve the best flat. The command values for the best flat are recorded as a bias vector in ACE.

The command matrix $\boldsymbol{C}_Z$ will then generate the command vectors for the DM, $\boldsymbol{c}$, from a vector of Zernikes, $\boldsymbol{z}$, such that

$$\boldsymbol{c} = \boldsymbol{C}_Z \boldsymbol{z} \tag{2-11}$$

However, to ensure the resulting wave-fronts created have as little residual modes as possible, we take another step to calibrate the Zernike modes.

For the set of Zernike modes intended to be used for open loop control on the DM we calibrate the commands for each mode in turn. For each mode we apply a series of amplitudes of that mode on the DM. Then using the SHWFS we estimate the error between the generated wave-front and the ideal wave-front for each Zernike amplitude. We then reduce this error to its minimum using the control matrix of the DM to reduce the error as much as possible. This is often referred to closing the AO loop as we use the error feedback from the SHWFS to remove the wave-front error. The command vector is computed as a linear fit of the commands at each actuator used to create each Zernike amplitude. These vectors are then saved in place of their corresponding vectors in $\boldsymbol{C}_Z$.

Obviously $\boldsymbol{C}_Z$ can be constructed in this manner without ever needing to use equation 2-7 but the calculation of $\boldsymbol{C}_Z$ is basically free in terms of time compared to the calibration procedure time. Plus, *a priori* knowledge of the commands required to create each Zernike greatly speeds up the calibration process. From this calibration we now have a transformation matrix to create any desired combination of Zernikes in open loop mode in the microscope.

Pinhole alignment

Once the best flat of the DM has been calibrated we are in a position to use the confocal system for the first time. Now the pinhole should be aligned. This is simply done by optimising the fluorescence signal in steps. First using a very high concentration fluorophores or fluorescence slide to see the focal spot of the fluorescence by eye in the system, then from a high concentration SRB sample initially (200nM) to find the coarse position in (x,y,z). Finally a low concentration SRB sample was used to optimise the axial position of the pinhole to obtain the best full FCS curve.

2.4.2
Scan calibration

An important aspect of imaging with laser scanning microscopes is to calibrate the distance at the image plane relative to the GM angle. This can be calculated roughly knowing the focal lengths and conjugation distance of all the optics between the GM and the object plane and using trigonometry. This gives us an estimate of 13.5 µm per degree. A better solution is use ray tracing [143,144] especially since our telecentric planes are not exactly at back focal planes and there are a number of glass surfaces other than the lenses on the path. From ray tracing of the system in LASSO we obtain 15 µm per degree. This corresponds to about 0.02 Vμm^{-1} with these GMs and we use this as a first estimate.

Calibrating the image size from here is then quite a simple procedure. We place a metrology slide at the focal plane of the microscope and scan an image of it. This can be done by either using a fluorescent scale or simply using the reflection of the laser at high power as some of the reflected light will pass through the dichroic and fluorescence filter to form a reflected confocal image at our fluorescence channel. We chose the latter technique. Using this image, the real distance can be measured in number of pixels and the Vμm^{-1} can be adjusted. Our calibration gives values of 0.0218 Vμm^{-1} and 0.0222 Vμm^{-1} for each of the axes. We can't account for this difference but we suspect the compact arrangement of the GMs and errors in the axial telecentric plane conjugations account for some of this.

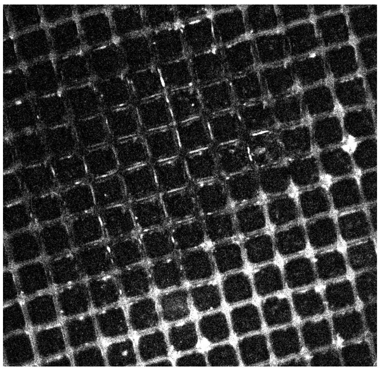

Figure 2.12 – A confocal image of a calibration grid on a metrology slide (Thorlabs, USA) used to calibrate the GMs. This grid is coated in a fluorescent dye. The spacing of the grid lines here is 10 μm and the resolution is set to 0.2 μm pixel^{-1}. Our calibration gives values of 0.0218 Vμm^{-1} and 0.0222 Vμm^{-1} for the X and Y axes respectively. The rotation of the grid is due to the 15 ° roll of the GMs physical orientation relative to the optical axis.

2.4.3
System performance

We assess the performances of the microscope for its intended use for FCS measurements. We also look at its imaging properties and the performance of its AO system. The AO system is obviously complex being the subject of the thesis but here we show simple experiments to assess its operation within the system and gauge its overall performance.

FCS

The priority for this system is accurate and precise FCS measurements. To this end we have optimised this system to be aberration free with a high NA, and a small pinhole to create a small Gaussian FCS observation volume while maintaining sufficient signal from the PSF [11]. We first examine the performance of the system looking at the FCS measurements in standard solutions. That is to say; known concentrations of stable fluorophores with known diffusion coefficients.

To demonstrate the performance of the system we used 10 nM SRB solution in H_2O. Concentrations this small are difficult to prepare to very accurate concentrations so this value should be taken as a reference only. Here we took an FCS measurement after correcting with AO. We averaged 6 measurements of 20 s and fitted the results using equation 1-5. The result can be seen in figure 2.13.

The absolute dimensions of the FCS observation volume can be calculated knowing the diffusion coefficient of the fluorescent molecule [7]. For SRB at 25 °C in H_2O, we have a diffusion coefficient of 426 $\mu m^{-2}s^{-1}$ [145]. The lateral extent of the volume can then be found as [7]:

$$w(x,y)^2 = 4D\tau_D\,, \tag{2-12}$$

where D is the diffusion coefficient. This gives us a value of 0.215 µm. The effective volume, v_{eff}, can then be calculated as [7]:

$$v_{eff} = \pi^{3/2} w^3 S\,, \tag{2-13}$$

where S is the axial elongation factor, obtained from the fit (equation 1-5). This gives us an effective volume of 0.3 fl.

Imaging

The microscope is not intended as a quantitative imaging tool, this is a secondary objective. However it is useful to understand and quantify its performance. To do this we prepare a sample of sub-diffraction limited fluorescent beads (100 nm crimson, Sigma-Aldrich) in a polyacrylamide gel, which has a refractive

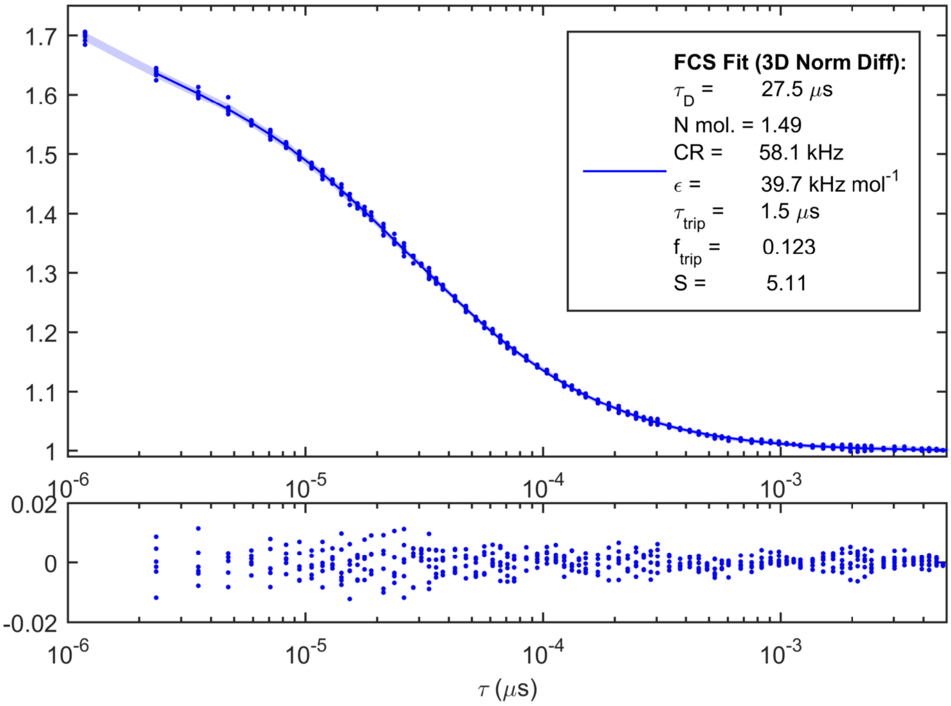

Figure 2.13 – FCS measurement in Sulforhodamine B Solution. An FCS measurement was taken in low concentration SRB solution (10 nM, N meas. = 6, t = 20 s, δt = 1.18 µs). The measurements were fitted using equation 1-5. The system was corrected using AO prior to the measurement. The residuals of the fit are shown below.

index very close to water. This gel creates a 3D sample with point like structures which can be used to characterise the 3D PSF.

Using this sample we capture a stack image of the beads, figure 2.14 shows a slice and two orthogonal slices of the stack. We measured the FWHM axially and laterally over 10 beads and obtained values of 1.3 µm and 0.26 µm respectively. Here there is no AO correction, the DM is corrected to its best flat using the SHWFS but open loop correction was not performed here. There is clear residual coma here which can be appreciated as a banana shape in the axial profiles of the beads and can be seen in the AO loop correction for system aberrations generally.

Adaptive optics

Measuring the performance of the AO in a microscope is not a trivial task as the performance metrics used are not general. The axial and lateral resolution of the system with various mis-matches of refractive index could be used [37] but this involves careful sample preparation with fluorescent beads generally [9]. We have a set of simple experiments that verify the operation of the AO using FCS measurements, which introduce various aberrations for which we can correct using the AO system, and quantify using FCS metrics [11].

The first and simplest way to check the operation of the AO system is to introduce spherical aberrations using the correction collar of the objective. The objective is focused into a solution of weakly concentrated SRB ($\simeq$ nM) in H_2O. The correction collar is adjusted to its optimal position by optimising the fluorescence signal and/or the number and brightness metrics (N/B, described in chapter 3). The AO is then optimised at this position to remove any system aberrations. An FCS measurement is then performed for this position. This task in itself should be performed before every experiment for two reasons: the FCS metrics can be used as metrology metrics for the performance of the microscope and serve as a quality control for the microscope [11], and secondly all subsequent measurements in the day can be normalised to (or simply

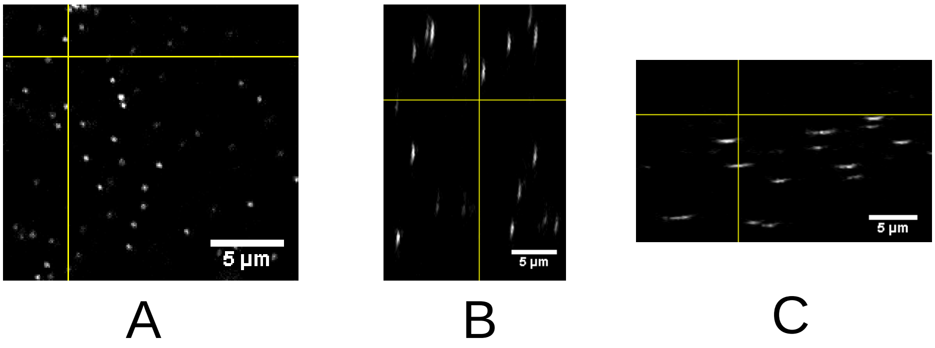

Figure 2.14 – Images of fluorescent latex beads in polyacrylamide gel taken by the confocal. A, image at a plane 4.0 µm behind the cover-slip; B, an XZ profile of the stack; C, a YZ profile of the stack. The mean axial FWHM is 1.3 µm (N = 10) and the mean lateral FWHM is 0.26 µm (N = 10).

referenced by) this calibration measurement.

The correction collar is then purposely adjusted away from the optimal position, to a position for a cover-slip that either is thicker or thinner. Both directions will have the same effect of inducing a small amount of spherical aberration, a combination of zero azimuthal order Zernike modes [36, 37]. We then take an FCS measurement for each collar position. It can be seen that the aberration induced by the incorrect collar positions will bias the FCS measurements by reducing the amplitude of the autocorrelation function and lengthening its decay time [112, 114]. Then for the same positions we optimise the AO system and examine its effect on the FCS measurements.

We should see two things happening; first is that the majority of the bias due to the incorrect collar positions should be removed and the FCS curves should be mostly renormalised. Secondly, the aberrations measured and corrected by the DM should be close to a combination of zero azimuthal order Zernike. If other aberration modes are present this is likely indicative of system misalignment, namely of the DM relative to the pupil, and thus there will be cross-talk of the aberrations [77,79].

A second method to characterise the performance of the AO is to induce a refractive index mismatch in the imaging path. This is much simpler than the case of preparing such samples for imaging metrics where sub-diffraction limit sized object is required, in the case of FCS metrics we need only prepare a solution of fluorophores with a refractive index different to the imaging medium [114], in this case water. Here we prepare a solution of SRB in a glycerol-water mix (about 70 %). The AO system should be optimised in a water solution with the correction collar well adjusted first. We'd like to point out at this juncture that optimising the correction collar is no longer fully necessary in such an AO microscope and the DM can compensate for quite a range of sub-optimal collar values, however it is generally frowned upon to use an AO system to correct for static aberrations which could otherwise be compensated [146].

For this experiment we simple take FCS measurements at various depths behind the cover-slip with the DM corrected for system aberrations and then a second FCS measurement with the DM optimised using the AO loop. Here we should appreciate a similar bias of the FCS curves, as the experiment above, with focusing depth as the refractive index mismatch of the sample induces increasing spherical aberration [24, 35]. We should also find that the AO corrects for this in a similar manner.

2.5
Conclusion

We have developed a laser scanning confocal microscope with a sensor-less AO system.

Chapter 3
AO Metrics and Optimisation for FCS

The majority of microscopes incorporating adaptive optics use a feed forward optimisation system for optimising the wave-front. This system uses a user defined metric generally derived from specimen measurements to determine the best correction shape for the DM. Originally these systems used stochastic algorithms based on quasi random deformations of the wave-front by the wave-front corrector itself to determine the optimal wave-front shape [72]. However such algorithms were generally extremely time consuming and were less than robust as they could often finish in local maximums rather than the true global maximum in the correction spectrum of the deformable element. A significant improvement was achieved when using a modal basis for the aberrations such as Zernike aberration modes [41, 71]. It was demonstrated that microscopes were susceptible to aberrations corresponding to lower order Zernike modes due to small misalignments [147], refractive index mismatches [24, 35] and the typical structures observed using optical microscopes [27,28]. It was demonstrated by many groups that correction of Zernike modes up to the 4th or 5th radial order provided a significant improvement in signal to noise, resolution and contrast, particularly in multi-photon or non-linear microscopes [29, 81, 82].

It took some time however before correction schemes were well optimised for this open loop regime. In the beginning, the aberration correction schemes were based on the simplest of hill climbing algorithms where by each aberration mode would be optimised in turn in a series of loops until the metric converged to its maximal value [42, 72]. A series of measurements were performed for different amplitudes of the known aberrations until the metric converged to its maximum and this was repeated for a desired number of aberration modes. This process would then have to be repeated in many cases if there was any crosstalk between the aberration modes, this is to say if the aberration mode being measured had any impact on the other aberration mode being measured [77]. It would be logical to assume that if the mode basis was orthogonal, like Zernike modes, that there would be no such cross talk but even well designed systems can be far from this ideal scenario. For example, when trying to create Zernike modes using a DM, the eigenmodes of the DM are never a perfect basis for creating Zernike modes and this small crosstalk can be noticed in sensitive systems. This is before even mentioning correct pupil conjugations, pupil size matching, non common path errors, etc. This lengthy process of playing with each mode in a series of loops was inefficient, and sometimes prohibitive in regimes where photons were at a premium due to photo-bleaching or photo-toxicity.

Martin Booth demonstrated that for any aberration in the vicinity of the maximum value of a metric its function with amplitude could be approximated using a simple quadratic fit and therefore, its maximal value [73]. Not only that, but this optimisation could be performed from only a single measurement per aberration mode plus one measurement at zero induced aberration, which guarantees two samples per mode. In hindsight the 1 measure per N modes plus 1 measurement (N+1) is not very robust to noise but the method itself was almost universally adopted for open loop AO microscope systems.

To improve the accuracy and speed of aberration correction and ensure its reliability in presence of e.g. large or complex wave-front distortions, the optimisation process should be adapted to the application and in particular an adequate metric should be chosen. We have previously introduced a metric extracted from fluctuation analysis, the molecular brightness, which dependence on aberration amplitude is well-described by the Strehl ratio squared, similarly to the signal from a point-emitter [114]. Its great sensitivity is advantageous when correcting small aberrations for FCS measurements. Another quantity, the fluorescence photon count, can also be readily measured from a solution of mobile fluorophores and used as an optimisation metric. The use of these metrics may be interest not only for fluctuation techniques but for biological microscopy at large. Indeed, many implementations of sensor-less AO rely on maximising an image-based metric [78, 81, 82, 148, 149]. However, the sensitivity of such metrics depends on the imaged region (small and bright structures affording the highest sensitivity) and varies across the sample. Using mobile molecules for optimisation is an interesting alternative since most living samples either contain endogenous fluorescent molecules or can be easily doped with freely-diffusing fluorophores. Additional advantages are the reduced impact of photo-bleaching when measuring mobile as opposed to immobilised fluorophores, and the possibility of a truly local measurement, while image-based metrics entails spatial averaging.

In this chapter, we compare two metrics that can be used for sensor-less adaptive optics in a solution of fluorescent molecules: fluorescence count rate and molecular brightness. We first investigate their measurement noise and sensitivity to aberrations. In the small aberrations range, the AO correction accuracy is experimentally measured and theoretically predicted, for each metric, from its measurement noise and sensitivity to aberrations. We show that the metric that optimises correction accuracy differs depending on the concentration and brightness of the fluorophores. Then we discuss the properties of these metrics in the case of larger aberrations.

3.1
Definition of fluorescence count rate and brightness

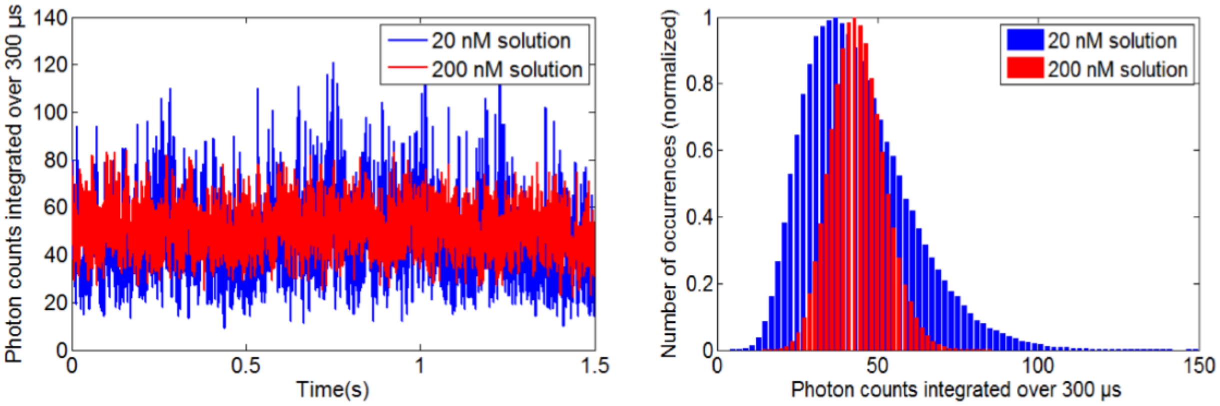

Figure 3.1 – Acquisition of fluorescence at a point in fluorescing solution over time. Left; a plot of the signal intensities over time for two concentrations of Sulforhodamine B solution: a 20 nM solution, a low concentration with bright molecules (*blue*), and a 200 nM solution, a high concentration with dim molecules (*red*). Both solutions produce a similar mean signal but with different variances. Right; the histograms of the signal for the two solutions displaying noticeably different profiles. The both solutions exhibit the same diffusion time and the brightness molecules in the solutions is changed by varying the laser power.

When performing fluorescence fluctuation measurements in solution with a fluorescent species the photons excited in a known detection volume over time are record at high cadence with a sampling δt such that the expected diffusion time of the species is adequately sampled. At each δt the photon counts, k, are recorded over a total record time, T, to get some statistics on the fluorescent species. Two example records are shown overlaid in figure 3.1 left. The photon counts are integrated over 100 µs (δt) over 1.5 s (T). It can be seen that the two concentrations give noticeably different signatures, the lower concentration (blue) has a higher variance and the higher concentration solution (red), even though mean value of both records is very similar. These differences of signature are clearer when examining the second moment of the fluctuations, as shown in the histograms in figure 3.1 right.

There are a number of possible parameters that can be extracted from these records but here, for the purposes of AO correction, we will concern ourselves with only two of these; the fluorescence count rate and the brightness, which have useful properties as metrics for AO as we will demonstrate and discuss here. The fluorescence count rate (or CR for simplicity) simply corresponds to the mean count rate of photons over T ($CR = < k > / \delta t$). Secondly, the brightness ϵ which simply corresponds to the CR per fluorescent molecule, on average. This can be determined from using the mean CR and then determining the number of molecules on average in the fluorescent volume N_{mol}, which can be extracted from the variance of the signal

$$N_{mol} = \frac{< k >^2}{(< k^2 > - < k >)} \tag{3-1}$$

where K is the total photon counts over T. This leads us to the brightness, ϵ, which is

$$\epsilon = \frac{1}{\delta t} \frac{(< \Delta k^2 > - < k >)}{< k >} \tag{3-2}$$

Here we add the additional $< k >$ to remove the contribution of the shot noise from the measurement. This method of determining N_{mol} and ϵ is well known and often referred to as number/brightness (N/B) analysis [150, 151]. It can be used to quickly determine the molecular concentration of a species without requiring an extended photon count record to determine a full autocorrelation curve and fit it. Having said that, in general the full autocorrelation is not required to determine N_{mol}, it can be determined from the first value of the autocorrelation curve $G(\delta t) = < k_i k_{i+1} > / < k^2 >$, and hence ϵ, as

$$\epsilon = < k > \left(\frac{< k_i k_{i+1} >}{< k^2 >} - 1 \right) \tag{3-3}$$

One caveat to this is that δt must not be too short so as to take into account other phenomena such as laser dynamics, rotational dynamics, detector noise and the fluorescent molecule's triplet state. Typically a δt greater than 3 µs is sufficient to both sufficiently sample the diffusion dynamics of the molecules used here (SRB in water) and avoid these artefacts. The effect of δt on these metrics is discussed in [122]. In practise we have found that using the first value of the autocorrelation curve to determine ϵ more robust and we will use it here exclusively in this work.

3.2
Measurement noise

To evaluate each metric in terms of its usefulness for AO it is essential to characterise its fundamental noise and understand the effect of aberrations on the signal to noise ratio (S/N). Here we look at the theoretical predictions of S/N and compare it to our experimental measurements.

3.2.1
Count rate

When talking about the noise on the count rate it must first be noted that fluorescence fluctuation microscopy refers almost exclusively to diffusing fluorescent species. Therefore the measurement noise is not only subject to the shot noise unless the number of molecules is sufficiently large. However, this is almost never the case, as the power of fluorescence fluctuation techniques is to measure low concentrated solutions in the first instance. Even large integration times do not simplify the noise to simply shot noise in the case of weakly concentrated species.

The fluorescence count rate (CR) is determined from the total photon counts, K, over a period, T. To calculate the measurement noise we refer to the derivation presented by Müller [152]. The probably distribution function of K is related to the integrated light intensity W on the detector by Mandel's formula [153] which states that

$$p(K) = \int_0^{\infty} Poi(k, \eta W) p(W) dW \tag{3-4}$$

where η is the quantum efficiency of the detector. This states that p(K) is the superposition of the Poisson distribution (Poi) for each W on the detector.

If we assume the experiment to be stationary then we can say that the integrated light intensity for a measurement time T is

$$W = \int_{-T/2}^{T/2} I(t) dt \,, \tag{3-5}$$

then according to Müller et al. [152], the variance of W for a solution with $< N_{mol} >$ per observation volume and a brightness ϵ is

$$\langle \Delta W^2 \rangle = \epsilon^2 \langle N_{mol} \rangle B(T) \,, \tag{3-6}$$

where $B(T)$ is the binning factor which is dependent only on the temporal shape of the autocorrelation function:

$$B(T) = \int_{-T/2}^{T/2} (T - \tau) g(\tau) d\tau \,, \tag{3-7}$$

where g is the normalised autocorrelation function. A consequence of equation3-4 is that the cumulant value of W is equal to the factorial cumulant value of K of the same order. Therefore we can also relate their variance (second order cumulant) by:

$$< W^2 > = < K^2 > - < K > \,, \tag{3-8}$$

and we can therefore determine the variance of K from that of W.

We see that $B(T)$ depends largely on T. In cases where T is short compared to the diffusion time of the species then B(T) scales proportionally to T^2 and the variance, $\langle \Delta W^2 \rangle$, is proportional to ϵT, the number of photons detected per molecule during T. This is generally the case with N/B analysis measurements. On the other hand, if T is long compared with the fluctuation time then $\langle \Delta W^2 \rangle$ scales with T. This is logical when we think of the variance being proportional to the number of observed diffusion events in a time T.

Using the expressions for $B(T)$ from Müller et al. [152], which assumes normal 3D diffusion and Gaussian PSF we calculate the S/N for a range of cases and then compare these results to several experimental measurements using several solutions of sulforhodamine B (SRB) in water. Figure 3.2 A shows experiments on 2 such solutions with concentrations of 200 nM (1) and 20 nM (2) respectively. It can be seen that the theory is in good agreement with our experiment results here; a fast quadratic increase in the S/N for short T, diminished to smaller linear improvements for longer T.

3.2.2
Molecular brightness

Now we shall look at the noise related to the measurement if the molecular brightness. We recall our definition of molecular brightness from equation 3-3, using the first point of the autocorrelation curve. We hence express the noise on the brightness measurements as

$$\langle \Delta \epsilon^2 \rangle = \frac{\langle \Delta S^2 \rangle}{\langle k \rangle^2} + \frac{S^2}{\langle k \rangle^4} \langle \Delta \langle k \rangle^2 \rangle + \frac{2S^2}{\langle k \rangle^3} \langle \Delta S \Delta \langle k \rangle \rangle \tag{3-9}$$

where

$$S = \langle k_i k_{i+1} \rangle \tag{3-10}$$

To simplify here we have chosen to neglect the last term of equation 3-9 which simply says that the count rate and the autocorrelation are uncorrelated.

Equation 3-9 depends on the variance of $\langle k \rangle$. Here we use equation 3-6 since $\langle k \rangle$ is obtained from the integrated photon counts over T, and $\langle k \rangle = K/N$. The variance of the autocorrelation function itself has been discussed previously by several authors [131,154–156]. The first analytical expression for the variance by Koppel et al. [154] assumed an exponentially decaying autocorrelation function and Gaussian statistics for the fluorescent signal. This would only be valid for large observation volumes and deviates quite

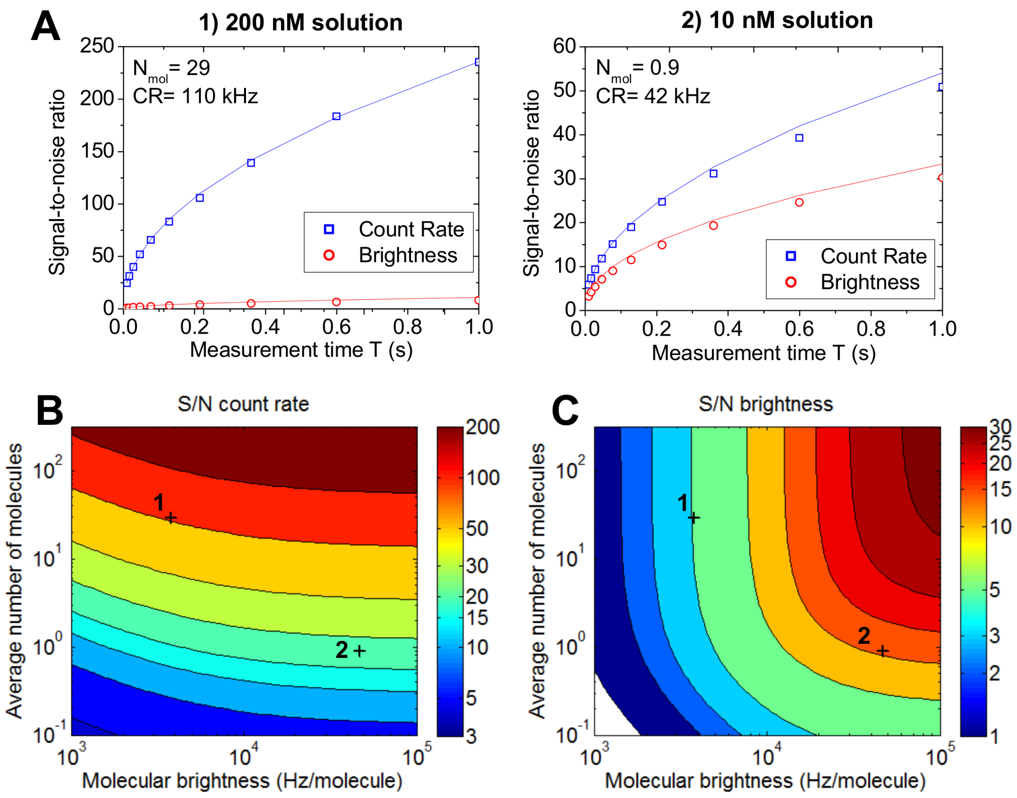

Figure 3.2 – Signal-to-noise ratio (S/N) of measured count rate and molecular brightness in different experimental conditions. (A) S/N measured (symbols) and calculated (solid lines) as a function of integration time T for both metrics estimated on two solutions of Sulforhodamine B of different concentrations. (B) Calculated S/N for count rate measurements and (C) calculated S/N for brightness measurements, as a function of the average number of molecules and brightness (integration time set at $T = 0.1$ s). The two solutions shown in (A) are depicted as crosses in the 2D maps.

significantly from experimental measurements at long time scales but can estimate the SD quite well at short time scales compare to other methods, as shown in Wohland et al. [131]. This method is also simply an approximation and requires *a priori* knowledge of $\langle k \rangle$, K, N_{mol}, the diffusion time and the exact shape of the PSF.

A much simpler method is to use the standard error of the mean on the autocorrelation function, which is justified given that the values of the autocorrelation function are in fact the average of a large number of calculated values for each τ [131, 157]. This method assumes that the count rate and autocorrelation are completely uncorrelated. This method is very simple but again is just an approximation and must be solved numerically or from experimental data.

The best analytical solution to our knowledge is that of Qian. [155] which we have previously used as an estimator for $\langle \Delta S^2 \rangle$, and shown that it is in good agreement with experimental data [122]. Hence, we estimate $\langle \Delta S^2 \rangle$ using equation 6 of [155], which we will not include here for brevity.

Using equation 3-9 and omitting the third term we obtain the following expression which we use to calculate the noise on the brightness:

$$\langle \Delta \epsilon^2 \rangle = \frac{N^2}{K^2} \Big(\langle \Delta S^2 \rangle + \frac{S^2}{K^2} \langle \Delta K^2 \rangle \Big) \tag{3-11}$$

In figure 3.2 we compare our results from measurements of S/N in two solutions and compare these to the analytical results. In figure 3.2 A we compare the S/N results with the count rate for the two solutions. An important factor which can be seen here is that the difference in the S/N between CR and ϵ is much much reduced for weak concentrations with few "bright" molecules. However, CR will always give the higher signal to noise ratio compared to ϵ for the same conditions. If we look at figure 3.2 B we see that the S/N ratio depends mostly on the number of fluorescent molecules but if we look at the same map for ϵ we can see that the S/N ratio also depends strongly on the brightness of the solution. The experimental results for solutions 1 and 2 in A are marked with crosses in B and C for comparison.

3.3
Sensitivity to aberrations: count rate vs molecular brightness

The results above indicate that CR has generally a much higher S/N than ϵ in almost all situations, except in cases of very low concentration of molecules. However this does not tell the whole story as we must now look at how aberrations affect these metrics in tandem. We have previously shown that ϵ is an extremely sensitive metric to optical aberrations, and that is scales with the square of the Strehl ratio [114, 122]. In this way we can say that it is analogous to a guide star; a point emitter whose signal would vary with Strehl^2 in the case of a confocal microscope: this is because it works in epi-fluorescence and the PSF (which defines the observation volume), is a product of the PSF of the excitation beam and the fluorescence beam. There is no coherence between the excitation and fluorescence light but they use identical optical paths and thus experience identical wave-front aberrations [158, 159] This is an important point because in the regime of FCS, with a static PSF volume in solution, the object (the fluorescent solution) is analogous to an infinitely extended source.

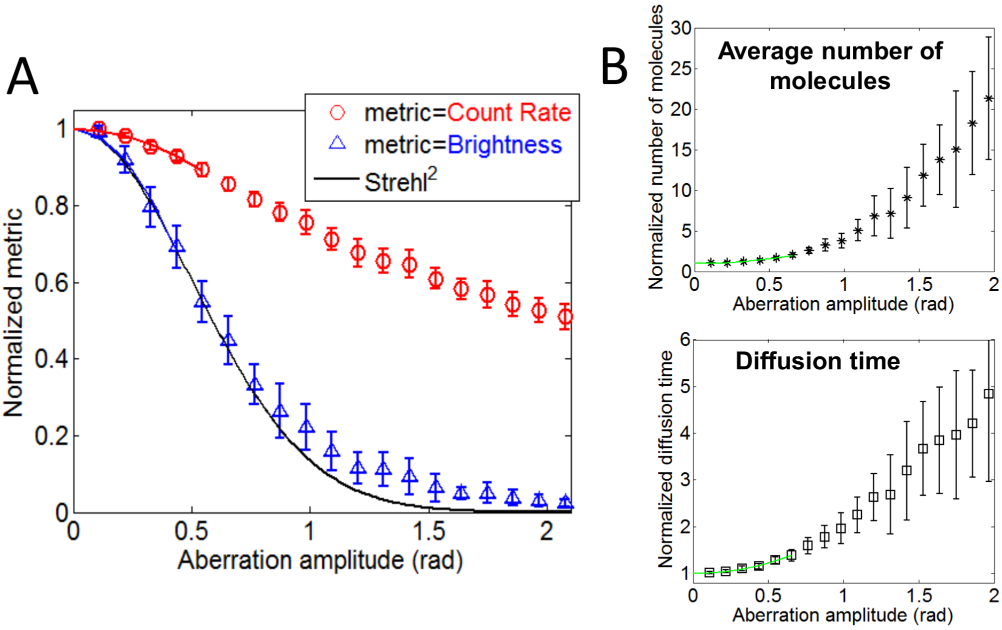

Figure 3.3 – Sensitivity to aberrations (A) Measured value of both metrics (count rate and brightness) as a function of aberration magnitude for random combinations of Zernike modes introduced by the deformable mirror. The sample is a aqueous 10 nM solution of Sulforhodamine B (N_{mol}=1.6). Each point is the mean and standard deviation of measurements obtained with 20 random sets of aberrations. The Strehl ratio squared is plotted as a solid line. Quadratic fits in the small aberration range for both metrics give sensitivity values of 0.37 rad^{-2} for CR and 1.5 rad $^{-2}$ for brightness (B) Variation of other parameters extracted from fluctuation analysis, the number of molecules (*top*) and the diffusion time (*bottom*) as a function of aberration amplitude.

Here we consider these metrics for aberrations only in the case of FCS and not for imaging. Aberration metrics for imaging are also reliant on the structure of the sample, a difficult thing to quantify. Hence, the sensitivity of the metrics changes depending on the structure of the object of interest [78, 81]. This is not the case in FCS where sensitivity of the metrics are dependent only on the quantity of total aberration.

We are considering the metrics of CR and ϵ in this work. We look at the experimental sensitivity of these two metrics to aberrations. In terms of aberrations we will use 11 Zernike aberration modes; we use modes up to the fourth radial order, excluding tip, tilt and defocus which are geometrical aberrations and, in the case of an infinitely extended object, have no effect on the metric except for vignetting in the objective. This choice of 11 Zernike modes is justified in the literature where generally small number of low-order aberration modes are measured and corrected with generally little improvement correcting beyond this [81,149,160].

Figure 3.3 shows the results of our experiments looking at the sensitivity of different metrics to aberration amplitude. In figure 3.3 A the sensitivity of CR and ϵ are compared; we record the metric values when applying random combinations of the 11 Zernike modes with a known overall amplitude. The aberrations here are applied using the DM in the microscope and are applied equally to both the excitation and emission paths of the microscope (The setup and methods are discussed in more detail in chapter 2). The sample used here is a 10 nM SRB solution ($N_{mol} \simeq 1.6$) and sufficiently high ϵ to give a good S/N ratio for both metrics. For each aberration amplitude we obtained 20 measurements with random Zernike combinations. The points represent the mean of these and the error bars correspond to the standard deviations.

Figure 3.3 A demonstrates how much more sensitive ϵ is to aberrations compared to CR. This can be understood when imagining the effect of aberrations on the confocal PSF. Aberrations will cause the objects illuminated by the PSF to become dimmer as there is less light concentrated in the PSF, however, at the same time, the PSF volume is becoming enlarged so more molecules can be observed at any time, countering the effect of the dimming. Hence, the CR is less sensitive.

It would be useful to quantify the sensitivity of the each of the metrics to continue our analysis and so we do this by obtaining a quadratic fit of the metric, M, in the vicinity of its maximum:

$$M = M_0(1 - \beta\sigma^2) \tag{3-12}$$

where M_0 is the metric value in the absence of aberrations, σ is the RMS amplitude of the applied aberration on the DM, and β is the sensitivity, the amplitude of the quadratic term. This function is fitted in the case of CR and ϵ for aberration amplitudes below 0.5 radians (Figure 3.3 A). The use of a quadratic fit is justified in the vicinity of the maximum regardless of the true form of the function [74]. The correspond fits of CR and ϵ vs aberration amplitude give 0.37 rad^{-2} and 1.5 rad^{-2} respectively, giving a $\beta_\epsilon \simeq 4\beta_{CR}$. Recalling the S/N of these metrics from the last section, this is immediately very interesting as cases where S/N would be similar for both metrics, β_ϵ would have a clear advantage as an AO metric in terms of final correction accuracy.

Figure 3.3 B shows two other metrics obtained from FCS measurements which were not considered as metrics for AO for this work; N_{mol} and the diffusion time τ_D. N_{mol} increases quite rapidly with increasing aberration amplitude, denoting a change in the FCS volume. N_{mol} exhibits a sensitivity which varies quite significantly with aberration modes. This is not discussed in further detail here except to say that this is not an ideal characteristic for a metric, especially in terms of comparison to CR and ϵ. The quadratic fit of τ_D yields a sensitivity of -0.90 rad^{-2}. This is less sensitive than β_ϵ and τ_D also requires higher K to determine it accurately, by nature. However, τ_D has a useful property of being an established metric for metrology in FCS instruments [11]. We will use this later to estimate measurement noise.

3.4
Correction accuracy in case of small aberrations

Now that we have established our definitions for sensitivity and S/N for our two metrics of interest, CR and ϵ, we want to examine the accuracy of AO correction using either as a metric under a variety of experimental conditions. We will compare our results to the theoretical performance.

To simulate a wide variety of sample conditions we chose four concentrations of SRB solution corresponding to N_{mol} = 0.5, 2, 8 and 30 in an observation volume of our confocal microscope, under best conditions and well corrected. For these four solutions we can simulate a wide variety of conditions by altering the laser power to vary ϵ between 3 - 80 kHz mol^{-1}.

We looked at the correction accuracy for each condition. The correction accuracy corresponds to the smallest residual wave-front error achievable, averaged of a number of trials (N=50 per condition). The best correction or DM shape was determined under ideal conditions, in an SRB solution with $N_{mol} < 10$ and a $\epsilon > 30$ kHz mol^{-1}, using the usual sequential mode optimisation protocol for a number of loops until the metric converged to a maximum (AO optimisation discussed in detail chapter 2). This bias shape was recorded as the zero position for each experiment and was calibrated before starting each experiment. For each trial a random combination of the 11 Zernike modes, with an overall RMS amplitude of 0.5 rad, was applied to the DM. A true random combination was chosen as there are no statistics on the aberrations encountered in microscopes, on the contrary to ophthalmology [161] and astronomy [162,163]. The residual aberration was then determined as the difference of the final shape of the DM after the correction protocol compared to the bias shape. The applied aberration is known to the user but the AO loop corrects it blindly.

The Zernike aberration modes are corrected sequential, in an order corresponding to their ordering using the ANSI ordering convention. For each mode there are 3 measurements (3N measurements total) one with a flat DM and two with a bias amplitude of the aberration mode with a bias of 0.5 rad chosen for all cases. The unbiased wave-front is re-measured after each mode and the wave-front is updated only in the case of improvement of the metric. This is contrary to the method used in Facomprez et al. for a similar study [78], where the unbiased wave-front is only measured once per loop and leads to (N-1) extra measurements, however our check improves the robustness of the correction to noisy measurements at the expense of correction time and photons. In all cases 3 iterations of the AO loop are used to attempt to achieve best correction. This is justified as can see from figure 3.4 A the mean value generally converges before 3 loops.

Figure 3.4 A shows the evolution of the metrics during a correction loop for 2 different cases (N=50 measurements per case). In the first example N_{mol} is the lowest of the four solutions (0.5) and ϵ is 25 kHz mol^{-1}. Here it can be seen that, on average, using CR fails to find a more optimum solution but using ϵ the wave-front is significantly improved (red line corresponds to the unaberrated case). On the opposite end of the scale in the second example, with high N_{mol} and low ϵ, with CR as a metric an improvement is easily found but there is no improvement for the same case with ϵ. Given these two examples a case to adapt the metric can be seen.

The parameter of interest here though is really the best achievable correction under each condition. Figure 3.4 B shows the best corrections achieved under each of the experimental conditions; each plot corresponds to a solution and each point corresponds to the laser power or ϵ used. Again these plots tell a similar story to figure 3.4 A; with high N_{mol} CR achieves the better correction, with low N_{mol} ϵ generally does better. It is interesting to note that at around 50 kHz mol^{-1} ϵ achieves almost the same performance in all cases and only drops off below this. However, with CR the accuracy is always dependent on N_{mol}.

Figure 3.4 B also shows the theoretical predictions for the AO accuracy in each case (solid lines) which we will now discuss: first we must determine the uncertainty of the mode amplitude at each correction step. As previously discussed, the quadratic approximation is valid here in the case of small aberrations. We assume also that the aberration modes are orthogonal, that is to say that there is no cross talk of the metrics between modes, which is mostly true, any residual cross talk is generally removed in consecutive AO loops (see chapter 2 for a more detailed discussion on aberration cross-talk).

Now we will consider the correction of a single mode of initial amplitude a_m. A number of measurements are performed in order to determine the quadratic fit of the metric in the vicinity of its maximum, since we consider only small aberrations here. Experimentally we have 3 measurements per mode, with a bias amplitude, x_i, which are sequentially introduced into the system, and then for each bias a measure-

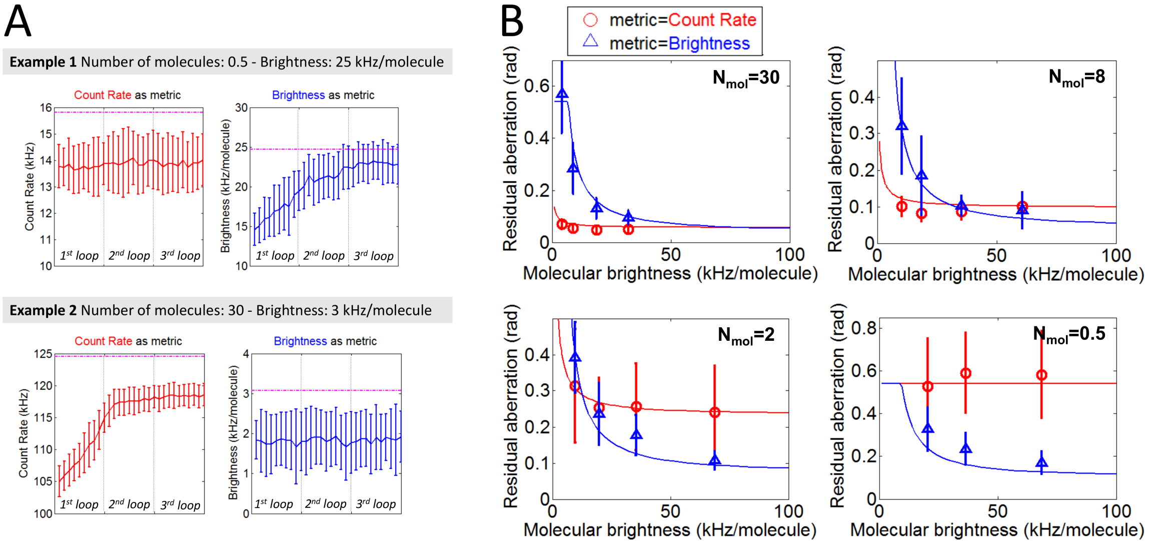

Figure 3.4 – Comparison of AO correction accuracy using either the count rate or the molecular brightness as optimisation metric. (A) Examples of optimisation in either a dilute sample with relatively bright molecules (*top*) or a more concentrated solution with dim molecules (*bottom*). The left graphs depict the count rate measured during AO optimisation using the count rate as metric. The right graphs depict the measured brightness during AO optimisation using the brightness as metric. (B) Residual aberrations measured in four samples with different concentrations (corresponding to N_{mol}=30, 8, 2 and 0.5 molecules in the observation volume) at various laser power. The error bars are the standard deviation of 50 optimisations per point for each metric. The continuous line are residuals calculated with the method presented in the text. The correction is performed on 10 modes using 3 measurements per mode (for bias -50 nm, 0 and 50 nm) and an initial aberration of 50 nm.

ment of the metric, y_i, is performed. We then determine a_m from a least squares fit of y_i as a function of the bias amplitudes:

$$\begin{aligned} y_i &= M_0(1-\beta(\sigma^2-a_m^2)) - M_0\beta(x_i-a_m)^2 \\ &= p - q(x_i-a_m)^2 \end{aligned} \tag{3-13}$$

Here we note that we have a fit function: $y_i = f(x_i, p, q, a_m)$. The accuracy of the estimated values of a_m will depend ultimately on the noise values of y_i which we have determined above.

To determine the variance of a_m, we first write the Jacobian matrix that relates small variations of the measured values y_i to that of the function parameters (p,q and a_m).

$$\mathbf{J}\begin{pmatrix}\delta p\\ \delta q\\ \delta a_m\end{pmatrix} = \delta \mathbf{y}_i \tag{3-14}$$

where the vector $\delta\mathbf{y}_i$ contains the measurements variations and $\mathbf{J}$ is the matrix:

$$\mathbf{J} = \begin{bmatrix} \vdots & \vdots & \vdots \\ \frac{\partial f}{\partial p}(x_i,p,q,a_m) & \frac{\partial f}{\partial q}(x_i,p,q,a_m) & \frac{\partial f}{\partial a_m}(x_i,p,q,a_m) \\ \vdots & \vdots & \vdots \end{bmatrix} \tag{3-15}$$

By inverting $\mathbf{J}$, the variation of the parameters can be expressed as a function of the measurement noise. We note $\mathbf{L}$ the following matrix:

$$\mathbf{L} = \left(\mathbf{J}^{\mathbf{T}}\mathbf{J}\right)^{-1}\mathbf{J}^{\mathbf{T}} \tag{3-16}$$

The variance covariance matrix of the parameters p, q and a_m, noted $\mathbf{\Sigma}_{\boldsymbol{\alpha}}$ is related to the variance-covariance matrix of the measurements,Σ_y, by:

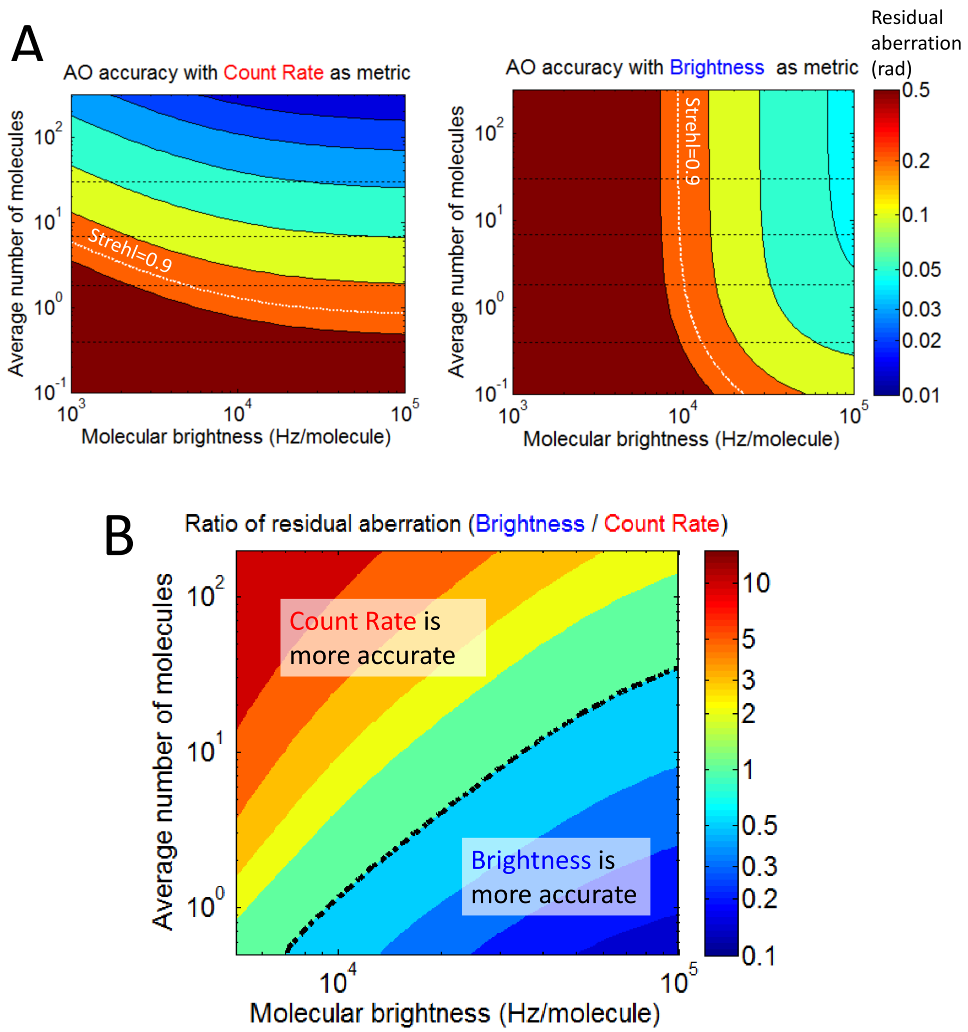

Figure 3.5 – Comparison of AO correction accuracy using either the count rate or the molecular brightness as optimisation metric. (A) Calculated 2D maps of residual aberrations expected with the count rate as metric (left) or the brightness (right) for a range of molecular brightness and number of molecules. The black dashed lines correspond to the samples used in the experiments. The correction accuracy needed for a Strehl ration of 0.9 is shown by a dashed white line. (B) Ratio of the calculated residual with the brightness metric to the one obtained with the count rate metric. When this ratio is smaller than 1, brightness leads to more accurate correction. When it is larger than 1, count rate yield more accurate correction.

$$\boldsymbol{\Sigma_\alpha} = \boldsymbol{L \Sigma_y L^T} \tag{3-17}$$

If the errors on the measured y_i values are assumed to be uncorrelated (the variance-covariance matrix then becomes diagonal), the variance of the estimated amplitude is given by

$$\langle \Delta a_m^2 \rangle = \sum_{i=1}^{N_{\text{meas}}} L_{3i}^2 \langle \Delta y_i^2 \rangle \tag{3-18}$$

where L_{3i} are the elements of the third row of $\mathbf{L}$ and $\langle \Delta y_i^2 \rangle$ the variance of measurement y_i.

Here we see that the error on the estimation of a_m is proportional to the measurement noise of the metric, scaled by some pre-factors that depend on the derivatives of the fit function. In particular, L_3i depends on the inverse of q. Therefore the error, Δa_m, scales proportionally to $(\text{S/N} \times \beta)^{-1}$, where we are reminded that β is the metric sensitivity. Here the dependence of Δa_m on the sensitivity is evident, which explains why we see cases where ϵ is a better metric, despite having a lower S/N (figure 3.5).

Now the entire AO correction process can be simulated for an initial aberration and the expected final residual aberration can be determined. We assume an initial signal and corresponding S/N determined by the initial amount of aberration. At the end of each step the test mode has been corrected to an amplitude statistically distributed around zero with an error corresponding to Δa_m. This process is then repeated for N_{modes}, corresponding to one loop iteration. In this calculation we assume that the initial S/N does not change from one mode to the next within a loop. This is of course not strictly true, especially if the amplitude varies significantly between modes. Here however, since the distribution of mode amplitudes is random, it is statistically likely that the amplitudes are close and is therefore assumed, and in this case updating the S/N once per loop is equivalent to updating it at each mode. In any case, we can see from figure 3.5 that the theoretical results are in good agreement with the experimental values. With this assumption we expect a residual wave-front RMS $= \sqrt{N_{\text{modes}}}\Delta a_m$. At the end of each loop of N_{modes} the S/N is recalculated for the next loop based on the theoretical value obtained and the loop is iterated a total of 3 times to mimic the experiment.

The assumption of the S/N remaining the same from mode to mode would be less valid if the majority of aberration amplitude was contained in one mode, which can often be the case in, for example, refractive index mismatched media where spherical aberration would be dominant [10, 24, 35, 164]. However the result of such a distribution would only improve conditions with even amplitude distribution being the worst case scenario. Attempting to initially correct modes with a low contribution to the aberration spectrum could actually introduce added noise and aberration into the system. This begs the case for *a priori* information on the aberration spectrum which could significantly improve correction efficiency [29].

Finally a fixed RMS wave-front error of E_0 = 2 nm was estimated as the "zero error" for the system to account for instabilities of the wave-front corrector, the non-common path errors of the system and the initial "best" correction of the system aberrations. In figure 3.5 A we see 2D maps of the best correction one can hope for for given initial ϵ, N_{mol} and a fixed initial aberration of 0.5 rad, like in the experiment. Figure 3.5 B shows the ratio of the residual aberrations using either metric to display in which cases CR and ϵ would be optimal. Again we see that cases with low N_{mol} would benefit most from using ϵ as a metric. Figure 3.5 B omits the portion of the maps in figure 3.5 A where neither metric provides any improvement.

3.5
The case of large aberrations

On examining again the metric ϵ we see that it is very well adapted for small aberrations (<1 rad) but for larger aberrations beyond this we find that we struggle to measure anything as the S/N disappears. In fact, for ϵ, the S/N drops to almost zero for an aberration amplitude beyond this. Therefore we must examine different strategies, and metrics possibly, if we wish to correct for aberrations of large amplitude

First we look at the evolution of S/N for the two metrics of interest for large aberrations, that is, greater than the case of 0.5 rad previously considered. This can be calculated theoretically using the expressions derived in section 3.2 for various input parameters. We also investigate this experimentally again using random combinations of aberration modes with known overall amplitude. These aberrations are applied by the DM and for each amplitude we use 20 sets of aberrations. For these experiments we use a single sample of $N_{mol} = 1.6$ with ϵ = 37 kHz mol^{-1} for the best corrected case. The results of this are shown in figure 3.6.

A striking result seen in figure 3.6 A is that the S/N of CR actually increases with increasing aberration and conversely, the S/N of ϵ decreases. Therefore when doing AO correction using CR we lose S/N while improving the wave-front. This is again actually logical when think of a finite number of molecules moving in the observation volume; if the volume is increased due to aberrations the noise due to occupancy of the observation volume is reduced.

We simulated the correction efficiency when correcting for an arbitrary mode with two aberration spectra. The each spectrum the aberrations are evenly distributed over N_{modes} = 10 and 50. The other parameters were set as per the experimental case of figure 3.6 A. Also the quadratic fit of the metric used

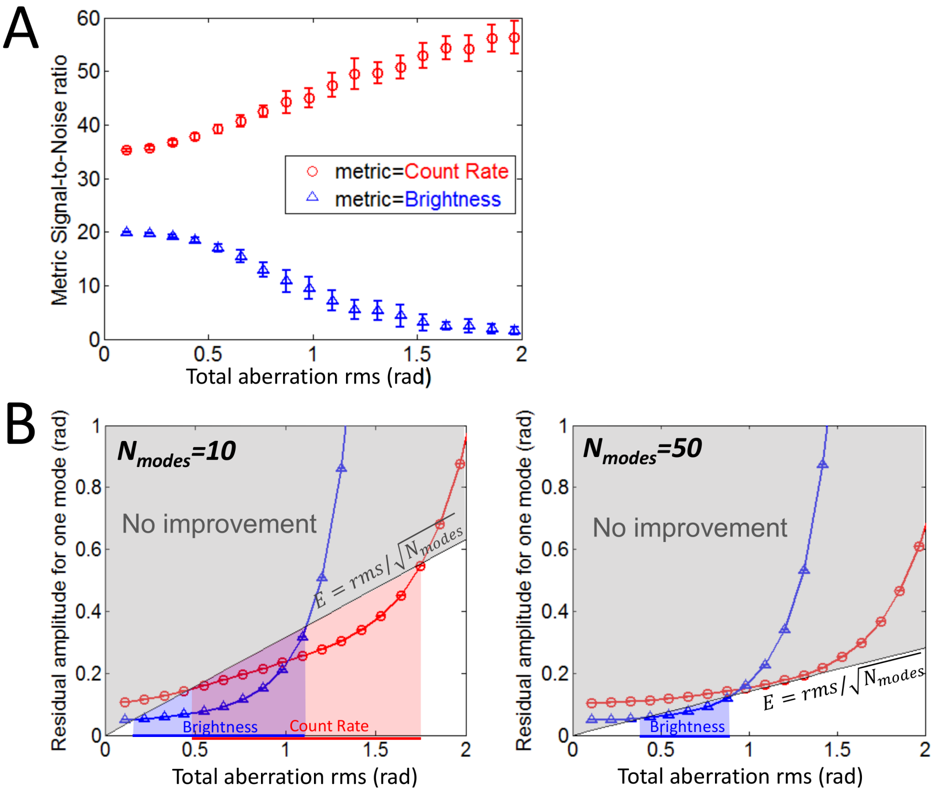

Figure 3.6 – Performance of the two metrics in case of large aberrations. (A) Expected signal-to-noise ratio of Count Rate (*red circles*) and Brightness (*blue triangles*) measurements as a function of total aberration amplitude. These S/N are calculated from measured values of CR, brightness and τ_D (Fig. 3.3) obtained for 20 random aberrations at each value of the total RMS amplitude. (B) Expected error on each mode estimation as a function of the total aberration amplitude, calculated with 3 measurements per mode and 50 nm bias, using either the Count Rate (*red circles*) or the Brightness (*blue triangles*) as metric. If the aberration is uniformly distributed over N_{modes} modes, an improvement can only be obtained if the uncertainty for one mode is below $RMS/\sqrt{N_{modes}}$. The corresponding area is shown for $N_{modes} = 10$ (left) and $N_{modes} = 50$. For all graphs in this figure, the sample we used exhibit 1.6 molecules and brightness of 37 kHz/molecule without aberrations.

in the previous experiment would no longer be valid as we are no longer in the vicinity of the maximum, therefore the fit was changed to a least squares Gaussian one here. Figure 3.6 B shows the results of this. If the wave-front aberration were distributed evenly over $N_{\text{modes}} = 10$ then the wave-front error of each mode would be $\text{RMS}/\sqrt{N_{\text{modes}}}$, and it can be seen that either metric can provide an improvement over different ranges up to 1.8 rad. However, if the wave-front error is distributed over $N_{\text{modes}} = 50$ then the hope for improvement reduces dramatically. However, using ϵ as metric provides a small opportunity for improvement. This is true only for the case of this solution however.

Coming back to the point of large aberrations in general though, we do not generally expect to have aberration spectrum with equal amplitude for each mode. If the overall aberration amplitude is relatively large then CR is clearly the advantageous metric, ϵ will not work efficiently beyond 1 rad RMS aberration, even with good S/N. CR can be used far beyond this given sufficient S/N.

3.6
Conclusion

The work presented here in this chapter was done in order to better understand the modal metric optimisation process for the AO in our microscope for FCS measurements. Here we have defined our metrics and investigated their noise and their sensitivities to aberrations. Using this information we were then able to predict the best possible wave-front correction achievable under various conditions using either metric for small aberrations (<1 rad RMS) and large aberrations. We also investigated a range of these conditions experimentally and we found that our predicted values calculated from theory matched the experimental values.

This work was investigated mainly for the case of performing FCS measurements in aberrating samples. The requirements of AO in FCS are much different from those in imaging microscopy, particularly that FCS measurements are often perform in objects with little or no spatial contrast. Therefore not all classic AO metrics are transferable or useful here. We showed that the metrics readily obtained from FCS measurements, particularly CR and ϵ, are suitable as a metrics for AO. Moreover, the metrics unique to FCS actually show a higher sensitivity to aberrations. This increased sensitivity means they can perform better as AO metrics in certain situations.

Still, there is no clear advantage of using either CR and ϵ. Best results for AO correction seem most likely when using both metrics together. For example; an initial loop with CR follow by subsequent loops with ϵ as a metric. We showed that CR has the advantage of increasing S/N with increasing aberration amplitude and remains sensitive to aberrations at large amplitudes. Therefore it would be better adapted to work in more aberrated situations and first test. However, as the S/N decreases with decreasing aberration it is unlikely to offer further improvement beyond one loop iteration. On the other hand, the S/N of ϵ increases with decreasing aberration, therefore further loop iterations using ϵ as a metric would be beneficial and likely to correct increasingly smaller aberrations. Added to this, ϵ can be, in some cases, a more sensitive metric allowing for more accurate wave-front correction, particularly in cases with low N_{mol} in the observation volume.

Chapter 4
The impact of aberrations on FCS measurements

Here we examine the effect of aberrations on FCS in confocal microscopy. The effects of aberrations on confocal and multi-photon microscopes has been examined experimentally by some groups, generally for imaging, whereby the typical aberration modes and amplitudes found in biological samples were examined [27–29,39]. There have also been theoretical examinations of the evolution of phase perturbations behind successive homogeneous layers with varying refractive indices [36,37], or amongst objects [73]. This work and others [102] have shown that aberrations in biological samples can have large amplitudes and also vary rapidly, spatially, within the samples. This scenario is a nightmare for AO: it calls for large number of degrees of freedom (modes), correction at each individual point, and thus when imaging the effective area of correction (isoplanatic patch) becomes very small.

The problem of aberrations is further exacerbated by the problem of scattering. Recently groups have demonstrated that focusing light through scattering samples is possible, even highly scattering objects such as a layer of paint can be corrected for using spatial light modulators and techniques somewhat similar to AO [165–168]. The impact of scattering on FCS measurements was previously investigated by Zustiak et al. [169], who observed that highly scattering media had little effect on FCS metrics although much fluorescence signal was lost.

Here we look at the effects of aberrators on FCS measurements. We look at the effects of low order aberrations increasing up to complex aberrations, approaching pure scattering. We also look at the transition between these two regimes. It is essential to understand the effects of aberrating specimens on the metrics of FCS to have an estimation of the error in measured FCS metrics when performing measurements in complex samples such as tissue.

4.1
Methods

To estimate the effect of aberrations with varying spatial complexity we propose a set of simple experiments: we examine the evolution of FCS metrics as we focus through and/or behind aberrating layers. To simplify, we aim to use pure aberrators. That is to say that the objects used to induce phase aberrations are composed of completely transparent material (on the scale of the object size at least), demonstrate low attenuation and scattering of light at the wavelengths concerned, and cause aberrations purely due to changes in refractive index relative to their surrounding media. As usual, the immersion medium and solution media are H_20 based and have a refractive index close to reported values of 1.330 for water [170]. The optics of the microscope objective already account for the presence of the cover-slip on which the samples resides. The position of the objective correction collar is optimised for maximum brightness in a standard solution before each experiment to minimise any residual aberration [171]. The correction collar is then maintained at this position for the duration of the experiment. Finally, the system is corrected for any residual aberrations with the AO using a standard sample of SRB. The procedure for this is outlined previously (Chapters 2 and 3).

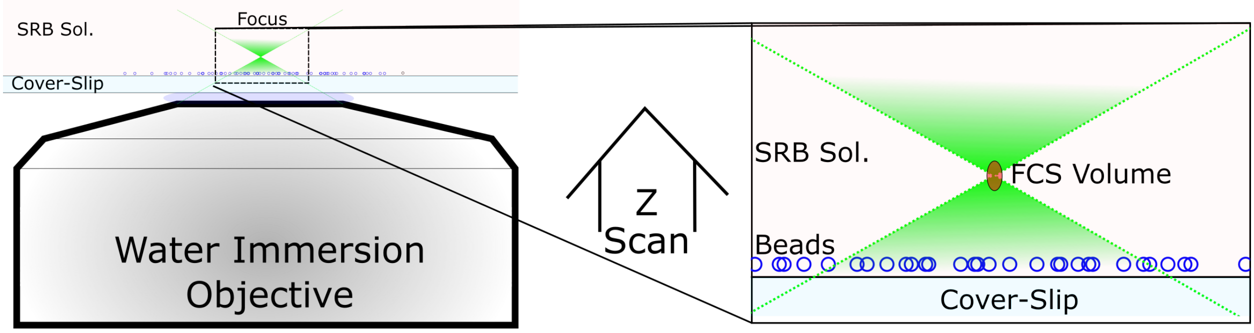

Figure 4.1 – Layout of experiments with aberrators (beads): On the left we see a simplified setup of the objective focusing into a solution of fluorescent molecules (SRB) behind a cover-slip. A homogeneous layer of aberrators is adhered to the cover-slip. The objective focus is scanned in the axial z direction from the cover-slip into the solution to a distance of several tens of diameters of the aberrators. An FCS measurement is performed at each position in z. This is repeated for several lateral positions in (x, y). On the right; a close up of the beam focused at a position behind the aberrators.

For each position in (x, y) FCS measurements are recorded at various distances in z through and behind the aberrating layer. Immediately before this, we calibrate the z position of the cover-slip for each position. This is a necessary step as the experiments can take many hours and this compensates for any focal drift or variations which can occur. We do this by recording the count rate at small intervals from a few μm below the cover-slip to a few μm above the height of the sample. This indicates not only the position of the cover-slip but is also an indicator of the proximity of an aberrator to the (x, y) sampling position.

However we cannot be certain of the position of the aberrators. Therefore, before beginning each experiment, a confocal image of the sample is taken at a height above the cover-slip which shows the position of the objects, i.e. at the characteristic half height of the sample. From this image we chose N points in (x, y) distributed in the field of view where we will perform the z stacks. These points should encompass the range of positions relative to objects one would likely encounter, i.e. in free space, or fully/partially obstructed by an object. These positions are recorded as stage positions. The approximate position of the cover-slip is also recorded at this time.

The FCS measurements at each point in z are generally carried out over a short interval (5-10 s) and averaged up to 3 times. The intervals here can be relatively short because we work with high molecular brightness's (30 - 60 kHz/mol., in control sample). The z range varies depending on the sample type; in general, tightly spaced sampling points close to the sample interfaces with increasing distance between sample points with increasing distance from the sample. It can be seen from trends in the results below that our choice of interval here is justified.

Since we will be using pseudo 2D samples resting on the cover-slip of known refractive index, the phase aberration induced at each position can be estimated from an image of the specimen and knowing the cross-sectional area of the light beam that traverses it. In this way, the phase perturbations that will be encountered at each position in (x, y, z) could be linked to their effects on the FCS metrics.

We make the assumption that the aberrators create a 2D phase screen and the FCS metrics at z positions below the characteristic height of the aberrators should not be considered as a consequence. First, an estimation of the cross-sectional area of the light beam at the sample plane needs to be determined. This can be determined by simply knowing the effective NA of the objective and the z position of the focus; this will give the cross-sectional beam area for each position in z. The radius of the cross-section of the objective beam, r_B, at the plane of the sample is determined by

$$r_B(z) = z \tan\left(\sin^{-1}\left(\frac{NA}{n}\right)\right), \tag{4-1}$$

where n is the refractive index of the imaging medium and and NA is the numerical aperture defined as:

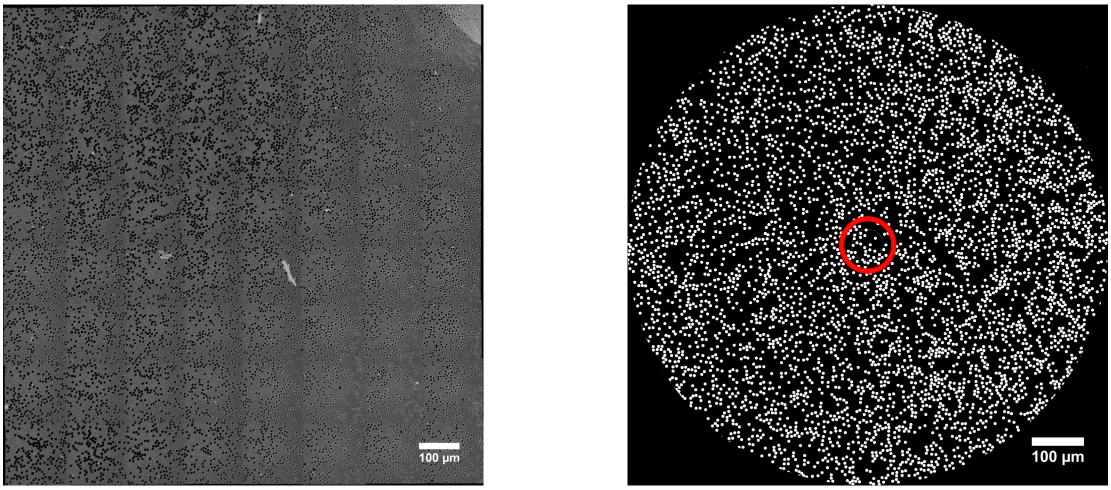

Figure 4.2 – (a)The confocal mosaic image after pre-processing (background removal and flattening) (b) The binarised mask created from the mosaic image. The large circle corresponds to a z position of 220 μm where as the smaller red circle corresponds to a focus depth of 20 μm.

$$NA = n\sin(\alpha)\,, \tag{4-2}$$

where α is the angle of the marginal ray. This can then be used to map the beam cross-section onto an image at the sample plane.

Due to the large NA of the objective, the cross-sectional area is considerably larger than the FOV of the objective at large z positions. This necessitates using a mosaic image of the entire area covered by the beads at large z. In practise, the mosaic image is obtained immediately before the ensemble of FCS z stacks. Knowing all the possible (x,y,z) positions for the experiment, a single mosaic can capture all possible beam areas as the distance between the sampling positions is relatively small. Thus we chose to use (x,y) positions for the FCS measurements which are close together. A $\leq$ 150 μm range in (x,y) compared to 1 mm beam area corresponds to a total mosaic area of $\simeq$ 1.15 mm . This translates to a single extra row of images in a mosaic compared to 25 mosaics of 1 mm diameter. An example of the mosaic image and the masks obtained is shown in figure 4.2.

In order that these images could be used as 2D phase masks, the images must be transformed. The exact procedure for this actually depends greatly on the object being imaged; some objects appear as dark spots in the images, like the beads in figure 4.2, others only the edges can be seen in the confocal image. No matter the case, we were able to use simple tools in Fiji (Imagej) to locate the objects. In the case of the 6 µm beads in figure 4.2, we used simple thresholding to create a mask showing the locations of the objects. This is possible as the objects appear as dark circles in the images since the beads are non fluorescent and the penetration of the fluorescent molecules into the polystyrene is poor. From this mask we centroided the locations of each of the objects to use for reconstruction of the 2D phase maps later.

In parallel with these experiments, J. Derouard at LIPhy was creating simulations to calculate the effects of the aberrators here on the molecular detection efficiency (MDE). The MDE is analogous to the PSF of the confocal system, and more specifically is the collection efficiency function (CEF) [172] of the system multiplied by the excitation intensity volume [8]

$$MDE(r',z) = CEF(r',z)I(r',z)\,, \tag{4-3}$$

where r' is the radial coordinate at the sample plane, z is the axial coordinate and $I(r',z)$ is the excitation intensity volume function. These simulations and experiments are ongoing and a full account of his results will not be given here. However, some of his observations from his experiments offer some detailed insight into certain experimental results related mostly to the polystyrene beads experiments. These will be discussed with the relevant results below.

4.2
Results

Here we present the results of these experiments using different types of samples. These experiments began with various sizes of polystyrene beads. The metrics examined in the experiments below are the count rate (CR), diffusion time (τ_D) and number of molecules (N mol.). All of the metrics are normalised to their values in H_2O, which is calibrated at the beginning of each experiment. τ_D and N mol. have been normalised inversely to τ_0/τ_D and N_0/N for the figures below as it normalises the direction of improvement similar to CR/CR_0.

4.2.1
Polystyrene Beads

The first model used in these experiments are polystyrene beads. These were chosen simply due to their well-defined characteristics and availability. Another major advantage is that the size is well controlled in a batch which is highly advantageous for modelling purposes. The typical refractive index of polystyrene in the range of wavelengths used in the microscope is 1.61. This is of course high in the range of refractive indices likely to be encountered in a biological sample [30, 32]. Objects exhibiting such high refractive indices can be found in many cells and tissues, particularly lipids and structures in the nuclei. Initially the goal is not to mimic cellular structures but to produce aberrations whose amplitude and complexity can be well controlled.

The bead sizes we used were 3, 6 and 15 μm. The mean metrics recorded from the ensemble of (x,y) positions can be seen in the figures 4.3, 4.4 and 4.5 for the 3, 6 and 15 µm. beads, respectively. The error polygons in each figure correspond to the standard error on the mean for non-identical measurements in (x,y).

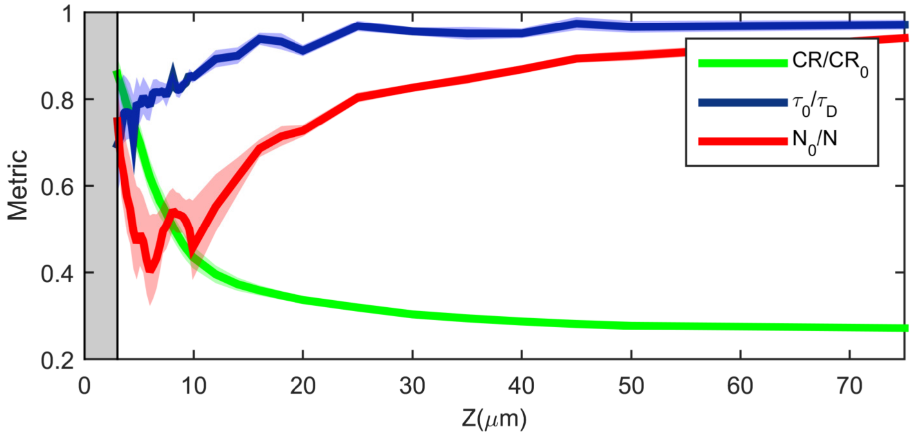

Figure 4.3 – FCS metrics focusing behind 3 µm polystyrene Beads. Plot of the FCS metrics recorded with varying z distances behind an aberrating layer. z = 0 µm corresponds to the position of the cover-slip. The grey area marked is the mean depth occupied by the sample. The mean values for the (x,y) positions with equal z are plotted for; count rate (green), τ_0/τ_D (blue) and N_0/N (red). The shaded areas indicate their errors corresponding in this case to the SEM. All measurements are normalised to their value in H_2O.

If we first look at the impact of the aberrations on the τ_D and N mol, we similar trends across the varying bead sizes. The maxima of the perturbations on N mol. occurs at a depth proportional to approximately twice diameter of the bead for all diameters of beads examined. Most interesting though is the fact that the metric is re-normalised at large depths, as to say that aberrations of a certain complexity have no effect on N mol. This trend is also clear for τ_D which renormalises at an even faster rate.

If we look at the count rate a very well defined trend can be seen across all sizes of beads that scales with the size of the beads. In general, the count rate decays exponentially to stable value at distances greater

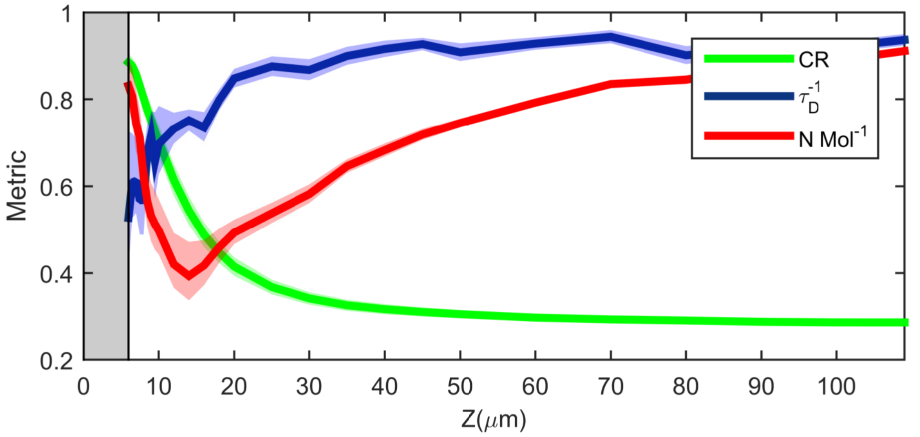

Figure 4.4 – FCS metrics focusing behind 6 µm polystyrene Beads. Plot of the FCS metrics recorded with varying z distances behind an aberrating layer. z = 0 µm corresponds to the position of the cover-slip. The grey area marked is the mean depth occupied by the sample. The mean values for the (x, y) positions with equal z are plotted for; count rate (green), τ_0/τ_D (blue) and N_0/N (red). The shaded areas indicate their errors corresponding in this case to the SEM. All measurements are normalised to their value in H_2O.

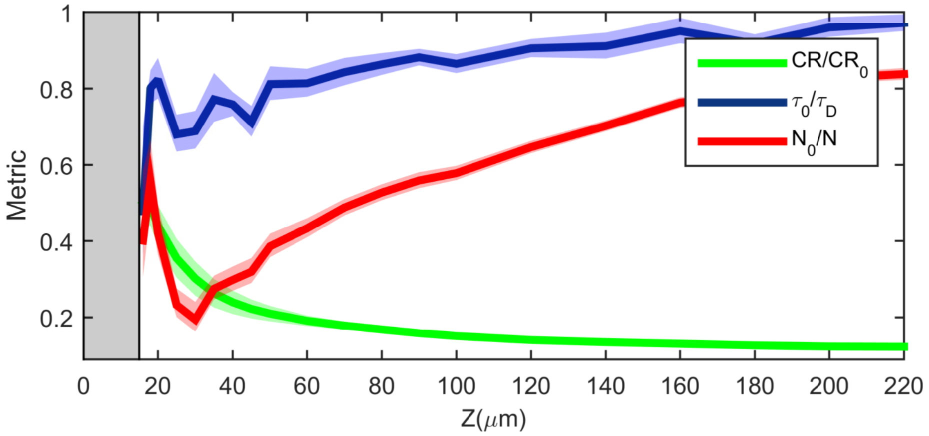

Figure 4.5 – FCS metrics focusing behind 15 µm polystyrene Beads. Plot of the FCS metrics recorded with varying z distances behind an aberrating layer. z = 0 µm corresponds to the position of the cover-slip. The grey area marked is the mean depth occupied by the sample. The mean values for the (x, y) positions with equal z are plotted for; count rate (green), τ_0/τ_D (blue) and N_0/N (red). The shaded areas indicate their errors corresponding in this case to the SEM. All measurements are normalised to their value in H_2O.

than 10x the diameter of the beads. The effect of the bead layer on the CR at large distances is expected as aberrating layer acts as a scattering layer. The effects at large distances beyond the beads can be explained by Mie scattering. J. Derouard calculated the scattering cross-section, σ_{SC}, of the polystyrene beads used here, given a planar wave-front, $n = 1.61$ for the polystyrene beads and $n = 1.333$ for the surrounding medium (SRB in water). He found an asymptotic value for σ_{SC} of $\simeq$ 2.2 for beads larger than 2 µm diameter. This of course varies depending on the bead size, as shown is his calculations in figure 4.6. This means that the effective scattering cross-section of the beads will correspond to approximately twice their geometrical cross-section.

If we compare this, for example, to the experiments with the 6 µm beads, shown in figure 4.2. For all z beyond 30 µm we found a mean coverage rate, τ_{cov}, of 0.19 per beam area. We examine the count rate at these distances diminishes to $\simeq$ 0.29. If we were to consider the beads as pure scattering objects with a scattering cross-section σ_{SC} who has equal effect on both the excitation and fluorescecne beam we can say:

$$I = I_0(1 - \sigma_{SC}\tau_{cov})^2, \tag{4-4}$$

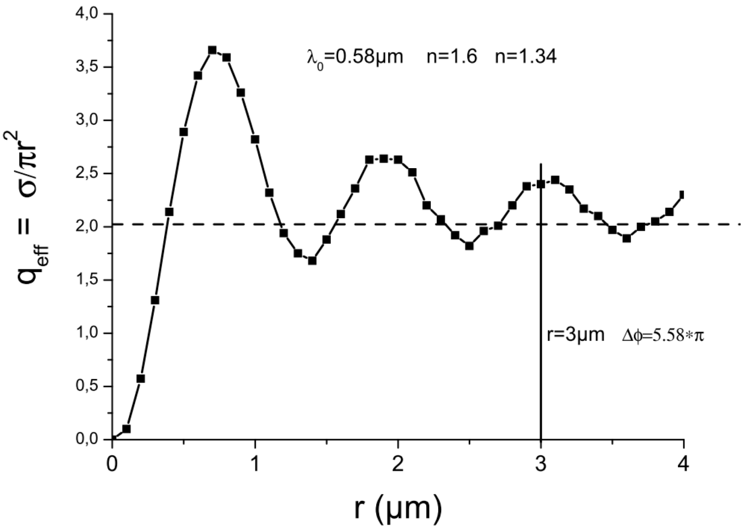

Figure 4.6 – Effective scattering cross section of polystyrene beads. The scattering cross section (q$_{eff}$ here, σ_{sc} in the text) of beads with radii, r, up to 4 µm is shown. The reafractive index of polystyrene was taken to be n = 1.61 and n = 1.333 for the surrounding medium with a λ = 0.58 µm. *Figure courtesy of J. Derouard*

where $\sigma_{SC}\tau_{cov}$ corresponds to the effective scattering cross-section of the beads. This gives us a value of I = 0.295 for the 6 µm beads, not at all distant from our experimental value of 0.29. This gives us an idea of what is happening to the MDE as the aberration complexity increases. As this complexity increases towards a medium which can be described by scattering, the scattered light becomes completely lost and no longer contributes to the actual form of the PSF and only as background. This is similar to effects seen in 2-photon imaging experiments of brain tissue where, even with AO, the experiment reaches a point where the a background intensity due to scattered light reduces the contrast to almost zero. On the other hand, the observed resolution up to this point is not limiting [60].

We also examined the similarities of the trends in CR for all the bead sizes. In figure 4.7 we have taken the CR data from each experiment and normalised the z distances to the corresponding bead diameters. It can be seen that the data from the 3, 6 and 15 µm beads (blue, red and green circles) is almost superimposable with a difference in offset from zero. Here we fit the data using an exponential fit:

$$\mathrm{CR}^* = Ae^{(-\alpha x)} + \mathrm{CR}_0(1-\sigma_{sc}\tau_{cov})^2, \tag{4-5}$$

where$A$, α and τ_{cov} are free parameters, σ_{sc} is taken from the calculated values of figure 4.6 and CR$_0$ = 1. For the 3, 6 and 15 µm beads we find values of 0.208, 0.192 and 0.295 for τ_{cov}, respectively. These values are the same as the determined experiment values determine from the confocal images (0.209, 0.189 and 0.291 for the 3, 6 and 15 µm beads, respectively). Their corresponding α are 0.576, 0.653 and 0.784, and A is 1.05, 1.20, 0.89. We do not have a robust physical interpretation for these parameters here; A is likely a normalisation factor, whereas α is likely linked to the amplitude of the phase perturbation as this would determine the transition rate from the aberrating to the scattering regime.

The diffusion time in FCS is often used, justifiably so, as metric to characterise the quality of a PSF [7]. Despite the amplitude of the aberrations and impact on the count rate, it is curious that the diffusion time is perturbed so little in comparison. The trend is clear, the fits of the corresponding FCS curves used in the data do not exhibit large residuals and are relatively consistent over 25 sample points, as can be seen from the shaded error bars in the figures. Like N mol., τ_D also renormalises after a certain distance except much sooner. This is to suggest that τ_D is only influenced by aberrations of relatively low order. These results are similar to those of Zustiak et al. [169] except that here there is only a single aberrating layer, yet at depth the impacts of both experiments are similar; high signal loss but relatively unperturbed τ_D. They do not,

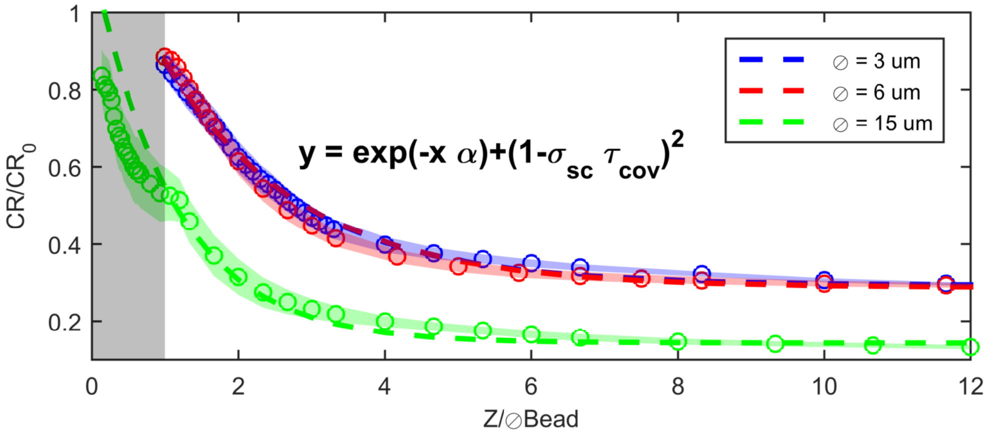

Figure 4.7 – CR trends for polystyrene beads. The CR data (circles) from the polystyrene bead experiments with 3 µm (blue), 6 µm (red) and 15 µm (green) diameter beads. The z values are normalised to the diameter of the beads. The data points correspond to the mean values and the shaded areas their respective errors, similar to figures 4.5, 4.4 and 4.3 above. These values area fitted using a least squares fit of the equation shown, for A, α and τ_{cov}, where σ_{sc} are fixed using their corresponding values from figure 4.6.

however, seem to observe the same perturbations we observe here when close to the aberrating layer. This is most likely due to the averaging effect of the particles diffusing and low enough concentrations. Their measurements are taken over long time scales ($\simeq$ 200 s), therefore statistically, given the concentrations used, their observation volume would be isolated from aberrators. There is still an effect on τ_D as the concentration increases and the occupation time of aberrators close to the observation volume becomes larger. We decided to investigate these trends further with different samples.

4.2.2
Polyacrylamide Beads

These results prompted for similar experiments using samples with refractive indices closer to those generally used to characterise live mammalian cells and their aggregates, such as tissue and spheroids. This would also permit using larger objects. Here, we chose polyacrylamide beads which were conveniently readily available in the group. The beads used have a much larger distribution of size than the polystyrene beads used above, even when filtered. This poses problems for direct comparison with numerical simulations and analytical calculations but we already have the polystyrene bead experiments results for this purpose.

The beads used here were synthesised in our group at LIPhy by M. Dolega. A detailed protocol of their preparation can be found in [173]. The beads can be synthesised with varying degrees of cross-linking and are generally used as pressure sensing devices [173, 174]. Homogeneity of stiffness is paramount to these experiments and size is less important. This is useful in our case as the optical properties of a batch of beads should be very similar, however, because of this their size varies quite significantly. We filtered the beads in stages to try and obtain a relatively homogeneous size for each experiment but this is not trivial. Their size distribution will depend on the stiffness of the beads as softer beads will 'squeeze' through spaces stiffer beads would not. Stiffer beads mean higher bisacrylamide concentrations which begin to change the refractive index to unknown values.

There have been few studies published on the refractive index of low density polyacrylamide, however one such study reports using polyacrylamide of a similar stiffness range to that used in this study [175]. They report a refractive index of 1.349.

To begin, the same experiments protocol used for the polystyrene beads was use. The results can be seen in figure 4.8. In some respects the results can be regarded as similar. The trends in each of the metrics follow

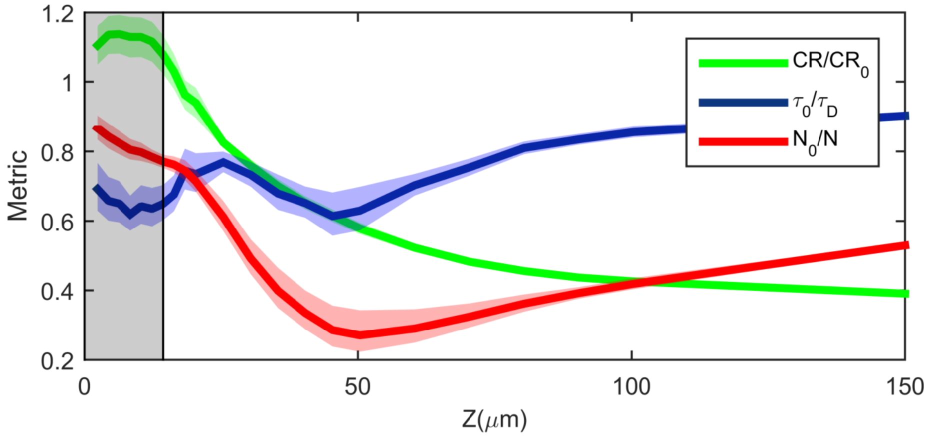

Figure 4.8 – FCS metrics focusing behind 12 μm PAA Beads. Plot of the FCS metrics recorded with varying depth behind an aberrating layer. 0 μm is the cover-slip. The grey area marked is the mean depth occupied by the sample. The mean values for all the (x, y) positions are plotted for; count rate (green), τ_0/τ_D(blue) and N_0/N mol. The shaded areas indicate their errors corresponding in this case to the SEM. All measurements are normalised to their value in H_2O.

a similar geometry with respect to their change with increasing depth. However some of the differences are not intuitively expected and are quite surprising.

In the case of the PAA beads, the phase perturbations are in general smaller in amplitude and certainly of lower complexity, owing to the size of the beads. However, the bias on the diffusion time is up to 5x compared to a control, i.e. generally much larger than the perturbations seen using the polystyrene beads.

Now these samples are starting to tell a story. It seems that the lower phase gradients and frequencies, induced by the polyacrylamide beads, have strong impact on the metrics of N mol. and τ_D. Conversely, the count rate decays at a much slower rate.

4.2.3
Sparse cell layers

Now that we have examined the impact of phantoms with a range of refractive indices and sizes corresponding to cells, we moved to look at the impact of (in vitro) cell samples on the metrics. Here we will replace the phantoms with sparse cell layers. The experiments were carried out using the same protocols as per the previous experiments although the time for each experiment needed to be reduced as the sample evolves with time. In this case the sample is alive and will move and multiply during the experiment. There is no rational solution to counter this, other than to kill the cells, but then the entire constitution of the cells will change and certainly their optical properties will no longer be the same.

Therefore there are some precautions to be considered for these experiments. Firstly, that no experiment should take an excessively long time because this will skew the statistics of our results. We have seen from the experiments with the phantoms that the impact on the metrics depends on the coverage factor of the specimen, τ_C. If the experiment is allowed to continue more than two to three hours there will certainly be more cells present at the end of the experiments compared to the start and hence a larger τ_C.

Secondly, and a more practical precaution, is the immersion medium. We use a water immersion objective and, as we all know, water evaporates! Water evaporates surprisingly fast at 37 °C when the ambient air is between 20 and 24 °C and the humidity is that of an air-conditioned room. This limited our experiments to less than 3 hours. Our objective could hold a little over 1 ml of water and this would generally be considerably diminished after 2 hours. That having been said, we did not seek more complicated solutions such as different immersion media. We managed to gather enough information in this window, however some data was lost in these experiments if, for example, we forgot to replenish the immersion water immediately before an experiment.

The cells used in these experiments were Madin Darby Canine Kidney Cell line (PTA-6500 [176]) altered to express red fluorescence. These were generously provided by V. Petrolli at LIPhy. Their nuclei were red fluorescent and this can be seen in the confocal images (figure 4.9 B). This has the potential for cross-talk with the SRB molecules but, since they were localised to the nuclei, this is relatively easily avoided, and all metrics below the height of the aberrating layer should not be considered for the purpose of these experiments anyway.

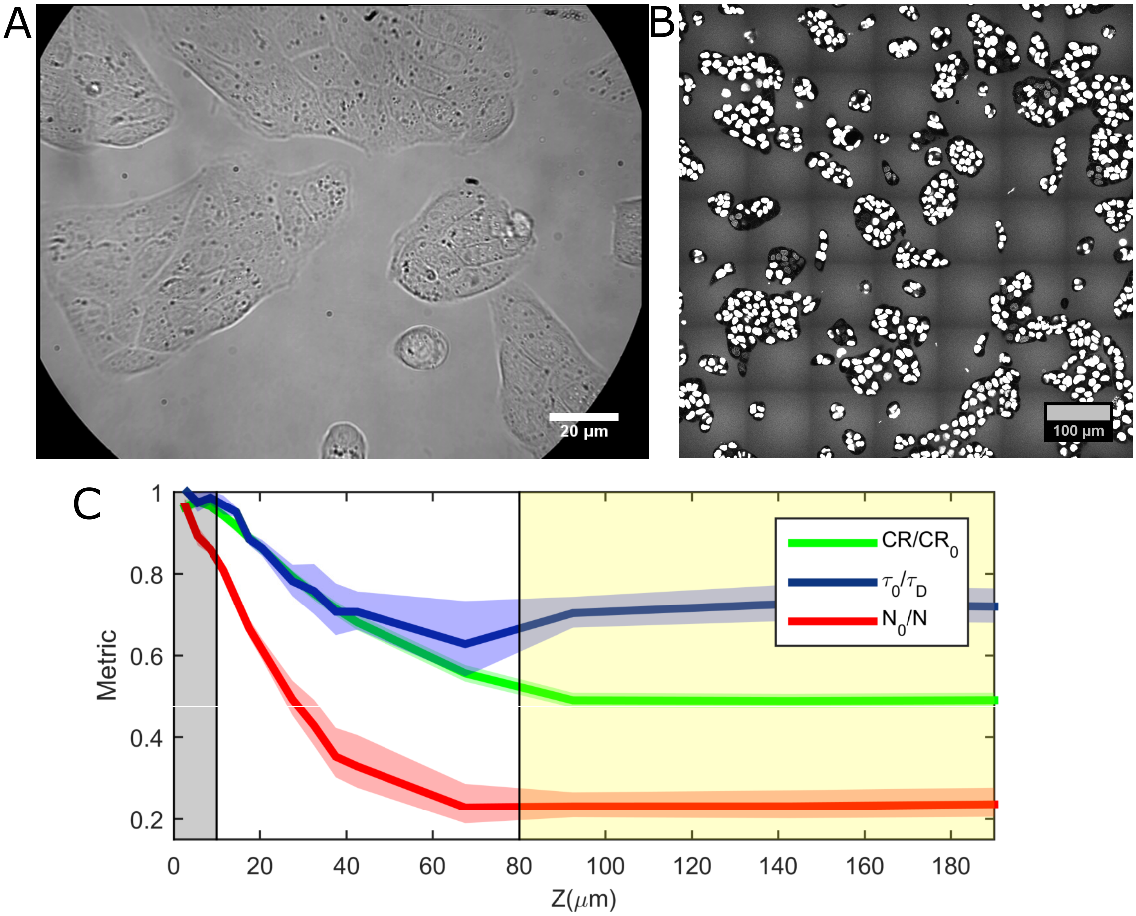

Figure 4.9 – Experiments with sparse epithelial cell layers. **A)** A bright-field image of the sparse epithelial cell layer. **B)** The confocal mosaic of the epithelial cell layer. The image encompasses an area that covers the beam cross-sections for every (x, y, z) position of the FCS measurements. **C)** Plot of the FCS metrics behind the cell layer. 0 µm is the cover-slip. The grey area marked is the mean depth occupied by the sample. The mean values for all the (x, y) positions are plotted for; count rate (green), τ_0/τ_D (blue) and N_0/N (red). The shaded areas indicate their errors corresponding in this case to the SEM. All measurements are normalised to their value in H_2O. The yellow area on the right corresponds to locations with low S/N due to high background fluorescence from the culture medium.

The results of one of these experiments are shown in figure 4.9 C. Images of the sample in bright-field and confocal can be seen in figure 4.9 A and B, respectively. It can be seen that the impacts on the FCS metrics exhibit a somewhat similar trend to the phantoms used above but nothing that the phantoms could reproduce individually themselves. It seems, as can be seen from the images, that there is a superposition of structure scales. There are small, highly diffusive particles within the cells (<5 µm), the structures of the cells themselves (10-20 µm) and the structure of the sparse aggregates of cells (>30 µm). The profile of the CR (figure 4.9 C, green) would give the impression that the CR falls to roughly half its value but unfortunately this value is biased. We only realised in retrospective analysis that the culture medium itself was somewhat red fluorescent and this, along with the red fluorescence of the nuclei, produced a significant background intensity. This is a nuisance but still, these experiments still managed to give some very interesting results when we involved AO correction in the equation.

4.3
Impact of AO

In the case of the polystyrene beads, the regime where AO could be useful for FCS measurements is very small: there is a small range beyond the sample where there is a large perturbation of the FCS metrics but beyond this range the effects on N mol. and τ_D diminish to zero. The signal to noise ratio could of course be improved but it is clear from the reconstructed phase perturbations (taken from images such as figure 4.2, reconstruction by J. Derouard not shown) that a SLM with a large number of degrees of freedom would be required to see useful gains. The case of the PAA beads is much more interesting.

The PAA beads already more closely resemble a typical sample that would be used in live cell imaging with a refractive index close to that of water. The PAA beads also create perturbations of the FCS metrics that are more significant compared to the polystyrene beads, an added challenge. However, the spatial frequency of these aberrations is typically much lower than those induced by the polystyrene beads. Much of these can, in theory, be corrected by a DM such as the ALPAO DM 97-15 of our microscope.

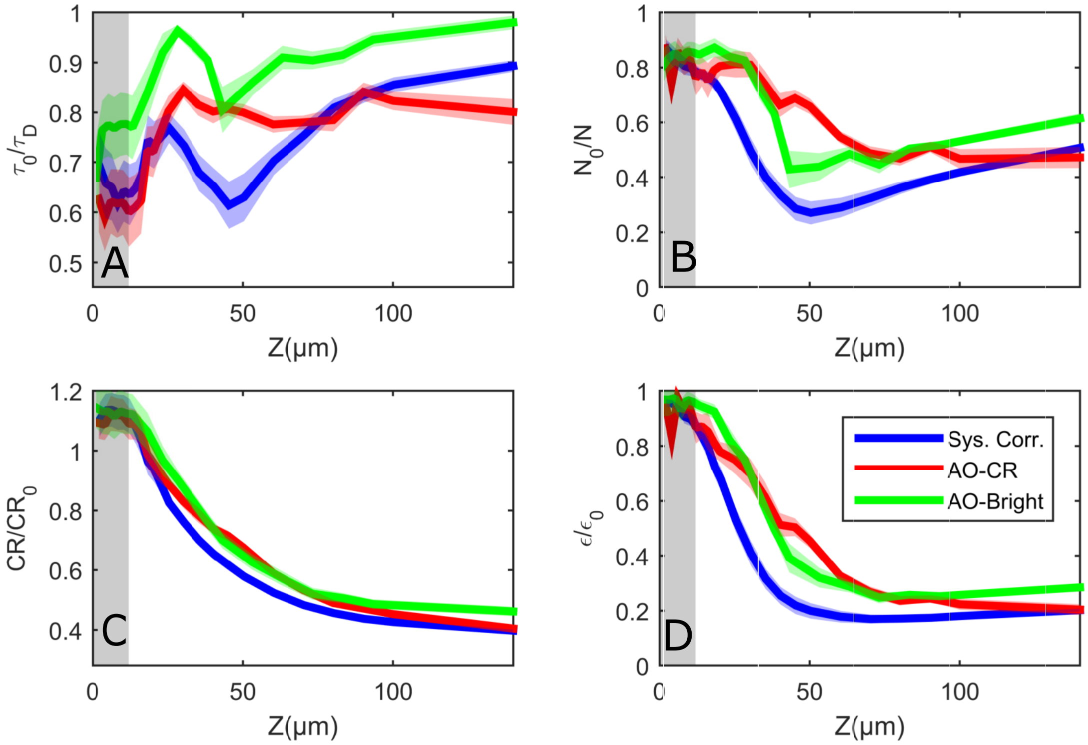

Figure 4.10 – Comparison of FCS metrics using AO with different optimisation metrics. The mean metric of FCS measurements when focusing behind 12 µm PAA Beads. The FCS measurements were taken first with the system correction (blue). The experiment was then repeated optimising the AO at each FCS position using CR as a metric (red). This was repeated again using ϵ(molecular birghtness, green) as a metric for the AO. **A)** τ_0/τ_D, **B)** N_0/N, **C)** CR/CR$_0$, and **D)** ϵ/ϵ_0. Metrics were averaged for non-equal (x, y) positions at equal z and the shaded area corresponds to the SEM.

The PAA beads used in this case were the 12 µm beads, the same as those used in the earlier experiments, and exhibit a size of typical mammalian cellular structures (5-15 μm). The experiments were carried out exactly as before with 10 z stacks at random points in the sample. This time the experiment was then repeated but using AO correction at each sampling point. At each FCS sampling position the DM was first set to a system calibration. This calibration is carried out before all experiments in a control sample of 10nM SRB in water. The system was calibrated using the first 27 Zernike aberration modes of the Noll index, minus the geometrical aberrations; tip, tilt and defocus (Z_1, Z_2, Z_3).

The AO correction at each sampling point was also carried out using the same 24 Zernike modes corrected iteratively over 3 loops in the usual manner (a detailed discussion can be found in chapter 2).

In the first instance, the AO correction was carried out using the brightness as a metric and subsequently using the fluorescence intensity as a metric. Each of these metrics had their own merits and disadvantages which can be observed in figure 4.10.

Firstly, the AO shows a clear improvement in all cases except in the case of the intensity where it is very marginal. In the case of simply improving the signal to noise ratio of fluorescence signal, the advantage of the AO here is not apparent, the gains are very modest. The FCS metrics tell a much different story, where the gains are immediately obvious. In the case of the measured diffusion time when using the brightness as a metric, the diffusion time is recovered in the majority of cases except where the perturbation is largest. The diffusion time at values less than 20 μm will in general be higher than the normalised value as some of these measurements occur inside the PAA beads where the diffusion time is significantly elevated compared to the diffusion time in water.

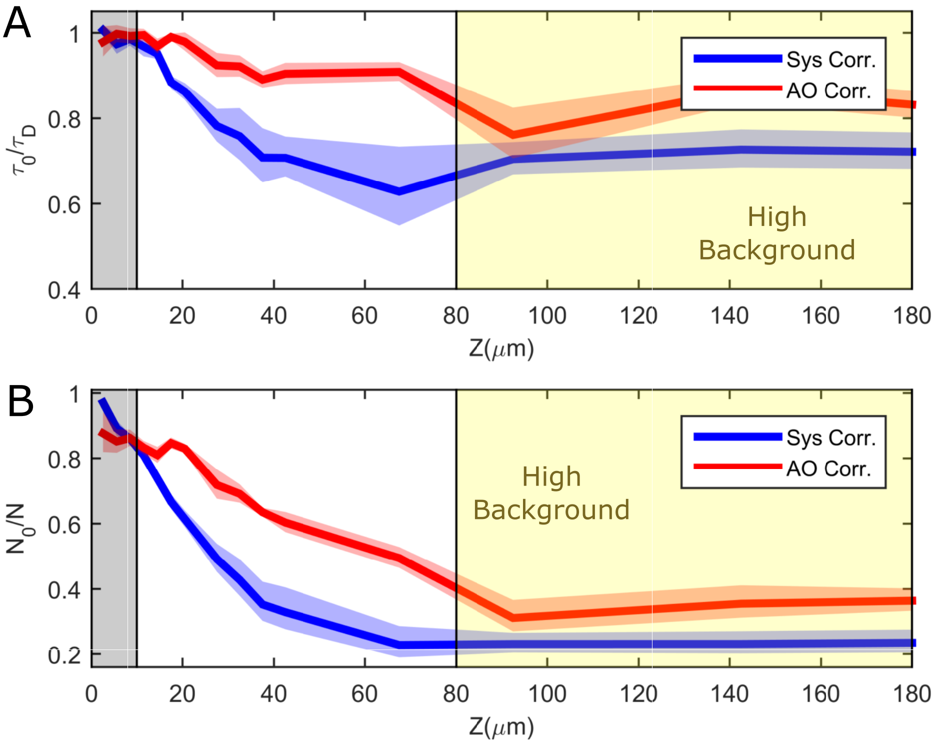

Figure 4.11 – Comparison of FCS metrics behind cells with Full and System Correction. **A)** The mean $\tau_)/\tau_D$ of FCS measurements when focusing behind sparse epithelial cell layer, shown in figure 4.9. The FCS measurements were taken first with the system correction (red) and then AO optimised (blue) at the measurement location. **B)** The mean N_0/N mol. for the same FCS measurements. The yellow area on the right corresponds to locations with low S/N due to high background fluorescence from the culture medium. Metrics were averaged for non-equal (x, y) positions at equal z and the shaded area corresponds to the SEM.

Using the CR as a metric, the gains are once again apparent but, interestingly, the metrics rarely improve to the same level as when using ϵ as a metric, with one notable exception: where the low order aberrations are largest at about 3x the bead diameter beyond the beads ($\simeq 50\mu m$). In this case the flux shows somewhat better improvements in all metrics and certainly less variation. This is likely due to the aberrations being too large to be efficiently corrected using ϵ as a metric and shows the need for specific metrics for FCS measurements to get the highest correction accuracy, and would argue that a combined metric would be the best option for these experiments (again, see chapter 3 for a detailed discussion.)

The nicest result here is the drastic improvement of τ_D when using AO. At many locations it is renormalised to within 2 µs of its value in water (27.5 µs in this case). It falls short in locations where the aberration amplitude is clearly largest, but some of this may be improved using a hybrid AO metric or 2 AO metrics in sequence. It also notably falls short close to the sample but, as previously mentioned, the bead size varies and some of these measurements may be inside PAA Beads where τ_D is naturally increased. This result is most interesting: it obviously not necessary to correct all possible phase aberrations to have unbiased FCS measurements.

Next we performed a similar experiment using the cell layer described in figure 4.9 as aberrators. In this case we changed the experiment somewhat in order to optimise it and get the maximum number of measurements in the window of time allowed. There were two FCS measurements performed at each measurement site; one with system AO correction and a second after full AO optimisation at the measurement site. Also, the AO optimisation was changed up in line with our findings from chapter 3 and demonstrated with the PAA beads here.

We used a 2 metric correction system which simply meant we would optimise first using fluorescence signal as a metric for the AO, for one loop only, and then we would switch the metric to ϵ to achieve the maximum correction accuracy possible. This is justified as can be seen from figure 3.6, where we see that the S/N of the CR actually increases with aberration and is therefore adept at correcting large biases. Once a correction is determined, the S/N of CR diminishes and further improvement is unlikely, especially if conditions point to it having a low correction accuracy (figure 3.5). However, if there is a small concentration of bright molecules then continued correction using ϵ may be fruitful especially considering the S/N of ϵ increases with decreasing aberration amplitude. The PAA bead experiments with AO justify this (figure 4.10); ϵ as a metric achieves the highest accuracy, whereas using CR as a metric allows an improvement in high aberration amplitude situations where ϵ shows little improvement on average.

The results of these measurements are shown in figure 4.11. The improvements in terms of τ_D are the most impressive here. It can be seen that for much of the experiment, where there is sufficient S/N, τ_D is almost completely renormalised. Beyond 80 µm the S/N is significantly reduced, most likely due to the contribution of the culture media and the fluorescence of the nuclei of the cells (This can be seen in figure 4.9 B). Nonetheless, this does not completely impede the performance of the AO, which is this case gives a 5 times improvement of ϵ and τ_D is significantly improved.

4.4
FCS Metrics Vs Aberration Complexity

All of the experiments we have shown above indicate that phase aberrations beyond a certain complexity do not significantly affect the FCS observation volume. We know from the experiments here using AO that a large portion of the enlargement of the observation volume can be corrected with relatively few Zernike modes (N=24), but how many Zernike modes would be required to effectively remove the bias?

To begin answering this question, we returned to some experiments we had been conducting to understand the sensitivity of FCS metrics to aberration modes in chapter 3. In figure 3.3, we see that for low order aberration modes (up to 4th radial order Zernike modes) the FCS metric of molecular brightness is up to 4 times more sensitive than the fluorescence signal. There however, we did not discuss the sensitivity of τ_D and N mol. (shown in figure 3.3(B)) which can be seen to be also very sensitive to the aberrations used.

Here we continued these experiments further and looked at the sensitivity of FCS metrics of CR, ϵ, N mol. and τ_D up to the 8th radial order Zernike modes. Our DM can generate modes up to this complexity, and beyond. However, the more complex the mode, the more likely there will be cross-talk between the modes simply because the DM is not a Zernike function generator. It can generate certain Zernike modes very well but the higher the mode complexity, the less likely a DM actuator will be well aligned with the Zernike function nodes and the residual aberration contribution becomes important. Therefore we examine only modes that have low residual aberration, which we measure from the calibration (see chapter 2 for details).

For each Zernike mode tested, we generate a series of bias amplitudes, b_i, (n = 15, b_{max} = $\pm$1.6 rad). For each bias we take an FCS measurement (T = 10 s) and fit the obtained autocorrelation function using normal

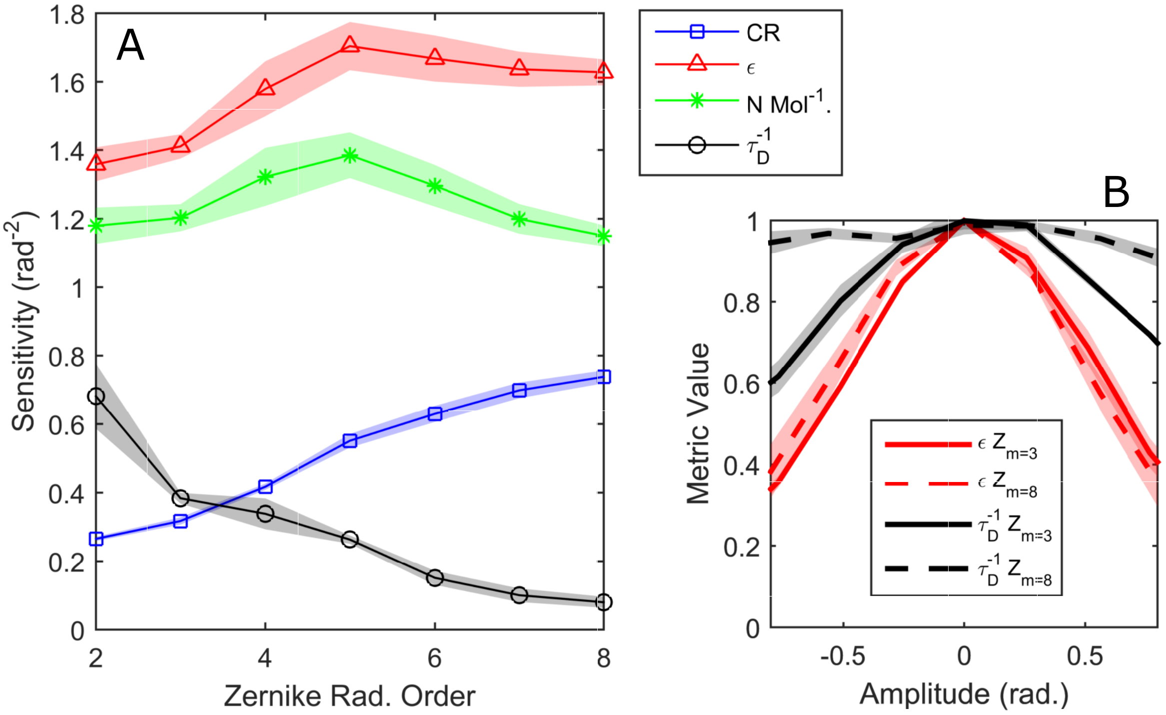

Figure 4.12 – The sensitivity of FCS metrics to aberrations. **A)** Plot of the sensitivity of CR/CR_0 (blue, sq.), ϵ/ϵ_0 (red, tri.), N_0/N mol. (green, *) and τ_0/τ_D (black, o) to increasing radial order Zernike aberrations. The values correspond to the mean sensitivities over all azimuthal orders within each radial order from m=2 to m=8. The shaded areas correspond to the SEM. **B)** Comparing the sensitivity of ϵ/ϵ_0 (red) and τ_0/τ_D (black) for Zernike radial orders m=3 (solid lines) and m=8 (dashed lines). As before, the values correspond to the mean and the shaded area their corresponding error (SEM).

3D diffusion function [2]. We use a brightness at zero aberration (ϵ = 45 kHz mol^{-1}) high enough such that the S/N is sufficient to determine the metrics for almost all aberration amplitudes. One may argue that the diffusion model is no longer valid in such regimes as the observation volume geometry is completely distorted, however we found that fitting this model was actually more robust than using the amplitude and FWHM of the autocorrelation curves, for example. There is no diffusion model available in the literature which accounts for observation volume distortion due to aberrations, to the best of the author's knowledge.

To determine the sensitivity of each metric, M, for each mode we fit a quadratic function to the metric values in the vicinity of its maximum using equation 3-12, as described in chapter 2. The region where the function is quadratic varies from metric to metric. This can be appreciated from figure 3.3, where the most extreme is the brightness, which can be described as quadratic only for aberration amplitudes <0.5 radian. We therefore use metric values less than this for the sensitivity fits of all the metrics. Figure 4.12 shows the sensitivity values of each radial order of Zernike mode. Here the values for the sensitivity of each radial order correspond to the mean sensitivity of modes with equal m. The shaded areas correspond to the SEM of the sensitivities.

Figure 4.12 shows some interesting trends in the metrics. Firstly, that the metric of ϵ has a consistently high sensitivity across the spectrum of aberration modes tested. This again demonstrates its value as an AO metric, with Strehl-ratio like behaviour, having a consistent function for all aberration modes. More important in terms of the impacts on the experiments in this chapter are the trends in the other three metrics. Most noticeably, we see a diminishing sensitivity of τ_0/τ_D to increasingly complex aberration modes. In fact, for the 8th radial order (Z m=8) the sensitivity of τ_0/τ_D has dropped practically to zero. This can also be seen clearly in figure4.12 B where the metric value is almost static for aberration amplitudes up to 1 radian (black dashed line), whereas for a low radial order, $m = 3$, the sensitivity is quite important. For comparison, we have shown the sensitivities of ϵ for the same radial orders.

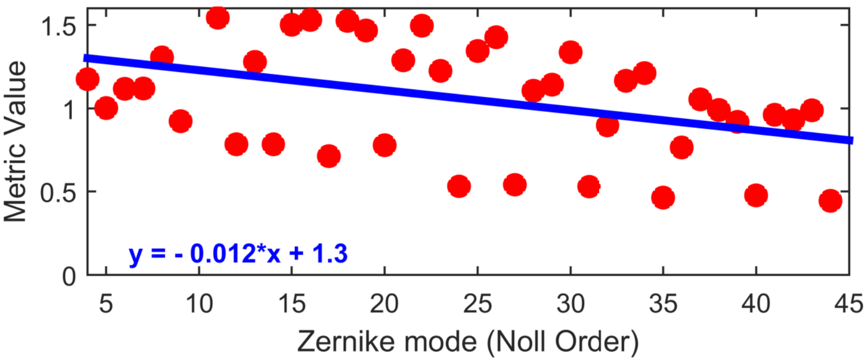

Figure 4.13 – Sensitivity of N_0/N mol. The sensitivity of N_0/N mol. is plotted versus increasing Zernike index (red). The Zernikes are ordered using the Noll index. A linear fit of these values is shown (blue).

Also interesting to note in figure 4.12 A is the increasing sensitivity of CR for increasing m, which appears to be linear. This is logical as increasing aberration complexity will scatter light at increasing angles such that it can longer be collected by the optics at all. Finally, a trend which we expected was a decrease in sensitivity of N_0/N mol., in a similar fashion to τ_0/τ_D, but this is in fact not so apparent. There is a slight decrease in sensitivity but if rather than grouping the sensitivities in radial order, we plot them instead versus increasing index, we start to see the diminishing trend, shown in figure 4.13 (red). A linear fit of these sensitivities indicates that the sensitivity of N_0/N mol. will diminish to zero at Zernike mode 112 (x axis intercept). This would correspond to the 14th radial order.

These trends in sensitivity of N_0/N mol. and τ_0/τ_D are in agreement with our experiments shown above, particularly the polystyrene beads (figures 4.3, 4.4 and 4.5), where we see τ_0/τ_D re-normalise to within 0.9 at a characteristic distance beyond the sample, and N_0/N mol. also re-normalise but at a much longer distance. These correspond to spatial frequencies of the phase aberrations in the Fourier dimension of $\simeq 2\, r^{-1}$ for τ_D and $\simeq 3.5\, r^{-1}$ for N mol, where r is the radial coordinate of the aperture.

4.5
Discussion

The results of the experiments in this chapter have given us some quantitative answers into the effects of aberrations and scattering of FCS measurements and some understanding into the frontiers between the two regimes.

If we look at the case of the polystyrene beads we could certainly draw some relations between the recorded FCS metrics versus depth. In this case, the τ_C relates to the quantity of light attenuated at large distances. It's clear from *a priori* that the larger the beads the larger the relative phase amplitude deviations. It can be seen from the polystyrene beads that the large amplitude, low order aberrations (i.e. close to the beads) have the greatest impact on τ_D. However, regardless of their initial amplitude, once the spatial frequency of the phase aberration reaches a threshold, it no longer has an impact on the measured τ_D. This is clear from almost all the experiments above.

It is difficult to jump to conclusions here on the actual effect of the aberrations on the PSF geometry and intensity. In this work we worked exclusively with the normal 3D diffusion model [2]. However, it has been shown that this model is only valid when the observation volume is near Gaussian [11]. In the presence of aberrations the observation volume will distort significantly [10]. However, the work shown here does show effectively the bias on this observation volume compared to the well corrected case. We believe that the bias of aberrations on FCS measurements is often underestimated; we have shown, here and previously [115], the effect simple transparent organisms, such as single cells and sparse cell layers.

Unfortunately, in the case of the experiments looking at the sensitivity of increase Zernike aberration orders, there is questionable reliability of the Zernike modes produced by the DM. There is a significant variance in the sensitivity of the modes here to certain aberrations (Figure 4.13)and this variation follows somewhat the pattern of the fitting error of the DM for high order Zernike modes. There is no need for a DM to produce such high order Zernike modes, as we mentioned above, thus they are not designed to do so with high fidelity. The trends in our results for τ_D and N mol. are clear and we believe that a similar test with any orthogonal mode basis would show the same results. We did not have time for such experiments in the scope of this thesis.

It is also unfortunate there was not time to further compare the experimental results to the work of J. Derouard. The author would like to express a sincere thanks to J. Derouard for his contributions and sharing his insights on the experimental results. The author would also like to thank V. Petrolli for providing and preparing the cell samples used in this chapter.

4.6
Conclusion

In this chapter we have examined the effect of aberration layers with controlled complexity and amplitude, on FCS measurements. We have shown that increasing spatial frequency of phase aberrations has a diminishing effect of the FCS metrics of N mol. and τ_D. We have related this to the radial frequency of the aberrations using Zernike modes and demonstrated that phase aberrations with a radial frequency > 2 r^{-1} have no impact on τ_D and > 3.5 r^{-1} have no impact on N mol. This is of course only valid for the optical geometry used in this thesis but this geometry is also typical of microscopes used for FCS in live biological specimen. We have also shown the effectiveness of AO in removing the bias of aberrations on these metrics, even for only a fraction of the demonstrated sensitivities.

Chapter 5

Quantitative Stress Measurements using FCS with AO

In this chapter we describe a new method to quantify the absolute pressure inside growing multicellular aggregates.

In our group, much work has been devoted to determine how an external compressive stress affects the the growth of multicellular aggregates, such as spheroids (tumour models [177]). This question is relevant in oncology; where tumour growth is limited by the surrounding stroma and tissues, and also in developmental biology; growing tissues apply pressure on their neighbouring organs and they in turn feel a reaction.

Previous works have shown that even a gentle mechanical compression (up to 5 kPa above atmospheric pressure) has a strong impact on the overall growth of spheroids composed of cancerous cells [178, 179] In particular, compressive stress arrests the cell proliferation in the spheroids as the cells approach the end of G1 phase [180]. Further, although this effect is global, it is markedly increase towards the core of the spheroid. This is counter intuitive as the pressure is applied from the exterior and physically one would expect the zones of highest pressure to be closest to the edges.

More recently in our group, Dolega et al. proposed a novel technique for localised pressure sensing in spheroids using micro-fabricated polymer beads [173]. In these experiments they could extrapolate information on the local pressure inside the spheroids by calculating the strain on soft fluorescent polymer beads using wide-field fluorescence imaging.

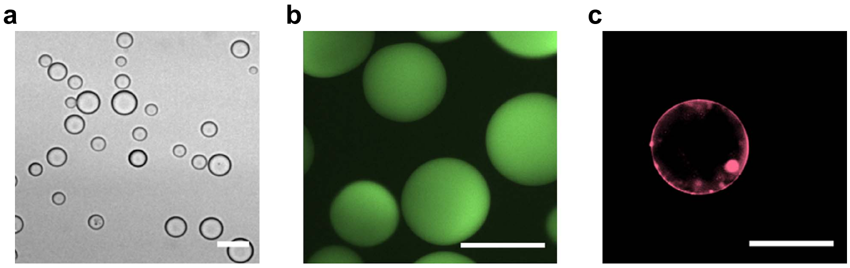

Figure 5.1 – Characterisation of polyacrylamide (PAA) beads. (a) Bright-field image of polymerised PAA beads after filtration. Scale bar, 50 mm. (b) Fluorescence image of PAA micro-beads containing trapped large polymers fixated with FITC; scale bar, 50 mm. (c) Fluorescence image of coating of PAA beads with Cy3-Fibronectin; scale bar, 50 mm.(*from Dolega et al. [173]*)

For these experiments micro pressure sensors were developed which exhibit measurable changes in their physical properties in proportion to the osmotic pressure they experience. These micro-beads were first developed in order for their changing strain to be observed using regular wide-field fluorescence microscopes [173]. Figure 5.1 (a) and (b) show bright-field and wide-field fluorescence images of an examples of such beads, respectively. Dolega et al. showed that for a known osmotic stress, applied using increasing concentrations of large dextran molecules [181], the beads would exhibit a regular, predictable and easily measurable strain.

It can be seen from figure 5.1 (a) that the size distribution of such beads is quite large. In fact, the manufactured size of the bead does not affect the strain measurements. What is important is that the cross linking of the bead's constituent polymer is homogeneous. A detailed protocol of their preparation can be found in the same work.

The stiffness of the fabricated beads can be estimated quite accurately by knowing polymer volume fraction [182].

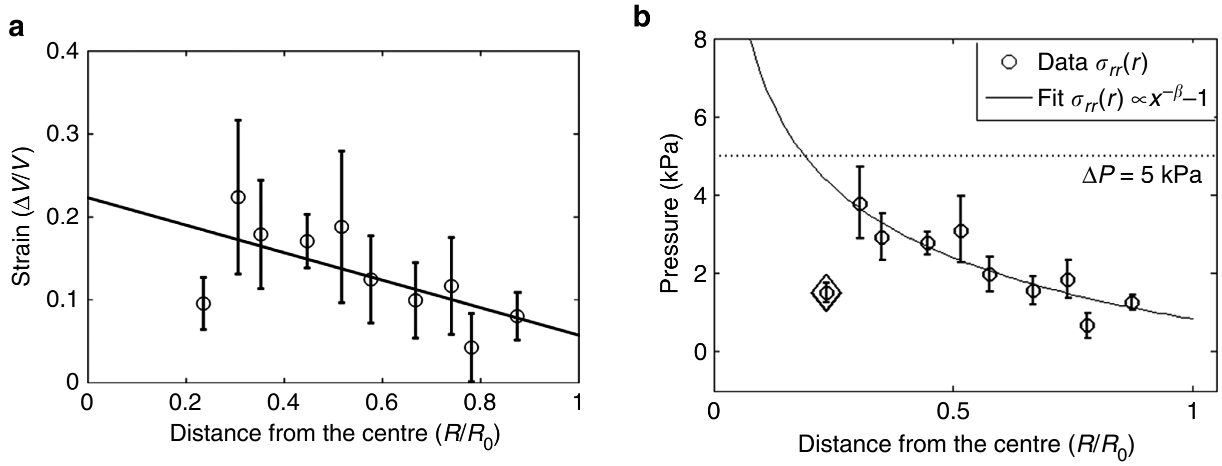

Figure 5.2 – Pressure distribution in CT26 spheroids upon 5 kPa compressive stress. (a) Strain profile of micro-beads $|V(P)-V_0|/V_0$) along the radius of the spheroid. Data points are grouped together in bins, with the error bar being a s.e.m. and the position being an average position within the bin. The solid line is a linear fit to all experimental data points and it indicates an increasing strain towards the core of the spheroids. (b) Pressure profile obtained with a stress/strain calibration curve of PAA micro-beads. The solid line represents a fit of r^{β} with $\beta = -0.21 \pm 0.1$. Error bars are s.e.m. The point for $r^{\beta} \simeq 0.22$ (losange) has been omitted in this fit.(*from Dolega et al. [173]*)

The calibrated beads were then introduced into spheroids. This was done by allowing the spheroids to proliferate around the beads which were coating in Fibronectin. From here the beads could be imaged in fluorescence imaging and their maximal cross sectional area was measured. Then the spheroids were compressed by adding marcomolecules (Dextran) to the surrounding media. As the Dextran is of large moleculur weight it does not actually enter the spheroid [173]. It exhibits a mechanical stress proportional to its partial osmotic pressure. The bead strain could be measured from the change in cross-sectional area in wide-field fluorescence images. The dextran molecules used are large enough that they could not enter the spheroids themselves [178]. From the measured strain the local stress can be calculated for each of the beads. From the measured data they were then able to demonstrate the mean pressure profile along the radius of spheroids of this cell type (CT 26, mouse epithelial colon cancer cells). These results are shown in figure 5.2.

Interestingly in these experiments, the pressure profile in the spheroids is increasing toward the spheroid core. Although this pressure amplification is counter intuitive, it is in direct agreement with previous observations [178–180], where increased cell apoptosis and arrested cell proliferation are observed toward the spheroid core.

The main limit of this approach is that it can only measure stress relative to a previous state of a somewhat mature spheroid. It is based on measurements of before and after states of the beads. The mechanical stress is then deduced from the relative variation of the strain, provided that the bulk modulus of the beads, κ, is well known (it is calibrated in this case). In addition, there is the presumption that the spheroids apply no mechanical pressure on the beads when there is no exterior stress on the spheroid itself.

This is a nuisance but the method does not allow access to the absolute stress measurement, only relative.

This is the main motivation for the following work described here. To introduce an alternative method to measure the bead stress and to have absolute measurements of the stress.

5.1
Diffusion Time as a pressure sensor

Polymer hydrogels, such as polyacrylamide, form porous gels in water through which water molecules and certain solute can freely diffuse as long as the solute is small enough [183]. It has long been known that the diffusion rate of a solution in a hydrogel is dependent on the volumetric fraction of the polymer [182, 184,185]. Also, since the hydrogel is porous, it is also compressible. It is this property that makes it extremely useful for measuring micro-strains in biological systems such as those described above [173] but also many others, even for single cell interactions [186] and even for larger strains given a suitable model [187].

In all the cases where the compressibility of the hydrogels is used as a bio-mechanical sensor, the observed strain of the gel is used to estimate the stress [173, 186, 188]. In the authors opinion, the beauty of these techniques lie in their simplicity: imaging is a ubiquitous, simple and accessible technique, all that is need to deduce the stress is some calibrations and careful post processing. However, there is another pathway to deduce the stress, measuring the diffusion within the polymer.

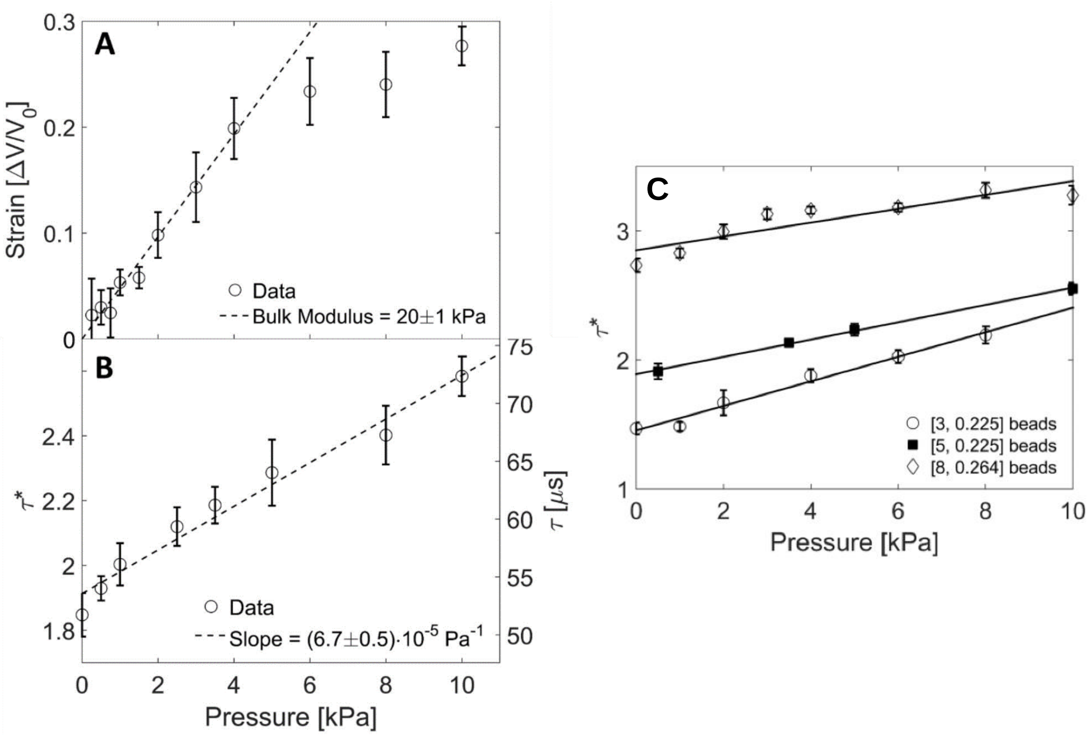

Figure 5.3 – Calibrating τ_D^* for an applied stress. **A)** The calibration curve for the strain of the PAA beads versus the applied mechanical pressure. The strain was measured using wide-field fluorescence images as detailed in [173]. **B)** The calibration curve for τ_D^*, measured inside the PAA beads, versus the applied mechanical pressure. A linear fit of these values gives a slope of 6.7 x10^{-5} Pa^{-1}. **C)** The calibration curves of $\tau_D^*$for bead stiffnesses of 3 kPa (circles), 5 kPa (squares) and 8 kPa (diamonds) are shown. The data in A and B correspond to the 5 kPa Beads.

As we pointed out, it is already well known that the diffusion rate of a solution in a hydrogel is dependent on its volumetric fraction. When the gel experiences a stress, its global volume will be altered and therefore the internal diffusion will also be altered. In our group we already had a technique in place to measure the diffusion within certain materials; FCS. Therefore our team set about investigating could the stress experienced by a body of hydrogel be deduced from FCS measurements of the diffusion time within the hydrogel.

The first method to examine the effect of stress on the diffusion time measured by FCS, τ_D, was to prepare a layer of hydrogel on a cover-slip, rather than a 3D structure. A known osmotic pressure was then introduced by placing dextran solutions of increasing concentrations on top of the hydrogel layer. The osmotic pressure induced by dextran solutions is well known [189, 190] and has been previously calibrated [181]. In a second set of experiments, the same method of inducing osmotic stress is also then used on the hydrogel beads to be used as pressure sensors, to see if there are any effects of gel geometry. The FCS measurements were then taken by focusing the microscope at a position close to the centre of mass of the beads. The microscope was calibrated in the usual way, as detailed in chapter 2, and system aberrations were removed by calibrating the DM in solution outside the beads. A number of FCS measurements were performed periodically outside the beads to measure the τ_D of SRB in H_2O, which we use as a normalisation factor. Each FCS measurement consisted of at least 3 averaged FCS curves with integrated over 5 to 20 seconds depending on the S/N.

The resulting FCS curves were fitting using either custom scripts for least square fits in Origin or QuickFit 3.0 [136]. The diffusion model used for the fit is 3D normal diffusion [2] and accounting for the triplet state of the molecule. In general we fixed the triplet decay time, τ_{Trip}, of the molecule for the laser power used and estimated its value from the calibration curves. This is not an exact science here, τ_{Trip} is not well sampled with our microscope, even though it does have an effect on our autocorrelations. Fixing τ_{Trip} is an effective solution, even for an estimate, and the triplet fraction is left free. All other parameters of the FCS fit are also free.

The results from the calibrations of the diffusion times vs osmotic stress on the beads are shown in figure 5.3 (a) and (b). Figure 5.3 (b) shows the response of the 5 kPa stiffness beads, which correspond to a volumetric fraction of polyacrylamide of 0.225. We can see that the response is very linear up to 10 kPa osmotic pressure with a uniform response of the τ_D where the error bars here represent the standard error over at least 10 beads per data point. Also apparent from figure 5.3 is the apparent saturation of the strain of the beads before 10 kPa but the diffusion time has a linear response throughout. The slope of a linear weighted fit of these points gives a sensitivity of 6.7 ± 0.5 x10^{-2}kPa^{-2}. The error here is estimated from the fit and in reality the error on the sensitivity measurements would be higher given the variance of the τ_D measurement. The error propagation was considered beyond the scope of this work.

We performed this same experiment with 3 different stiffness's of beads (figure 5.3 (c)) and found a similar linear response of τ_D to the applied osmotic stress. Logically, we found that the softer beads are more sensitive however the variance of τ_D was higher.

As an alternative method to measure the effect of mechanical stress, steel beads of known size and mass were place on a flat layer on the polymer adhered to a cover-slip. Figure 5.4 (a) shows a schematic of the experiment setup. The beads used were quite large, up to 1 mm, so the sample had to be scanned using the stage of the microscope. The centre of the beads were first located using the confocal system and then a 1D scan was performed in the gel along the diameter of the bead. For each horizontal position a z scan was performed taking N/B measurements at regular intervals from the cover-slip to the top of the hydrogel. This gave information about the profile of the indentation of the bead in the gel, and thus the strain (Figure 5.4 (b)). This info could be deduced from the fluorescence signal alone as the significantly higher τ_D of the solution in the gel, compared to outside, provides the contrast. It can be seen that the regions under the bead exhibit even higher intensities, corresponding to further elevated τ_D due to compression by the bead.

Then for each radial position of the scan an FCS measurement was performed at a height of about 28 µm above the cover-slip, corresponding to the white line in figure 5.4 (b). The resulting diffusion times are displayed in figure 5.4 (c) on the right axis, overlaid with their corresponding strain at each position, plotted on the left axis. The central position here exhibits a sudden increase in τ_D compared to its neighbours, this

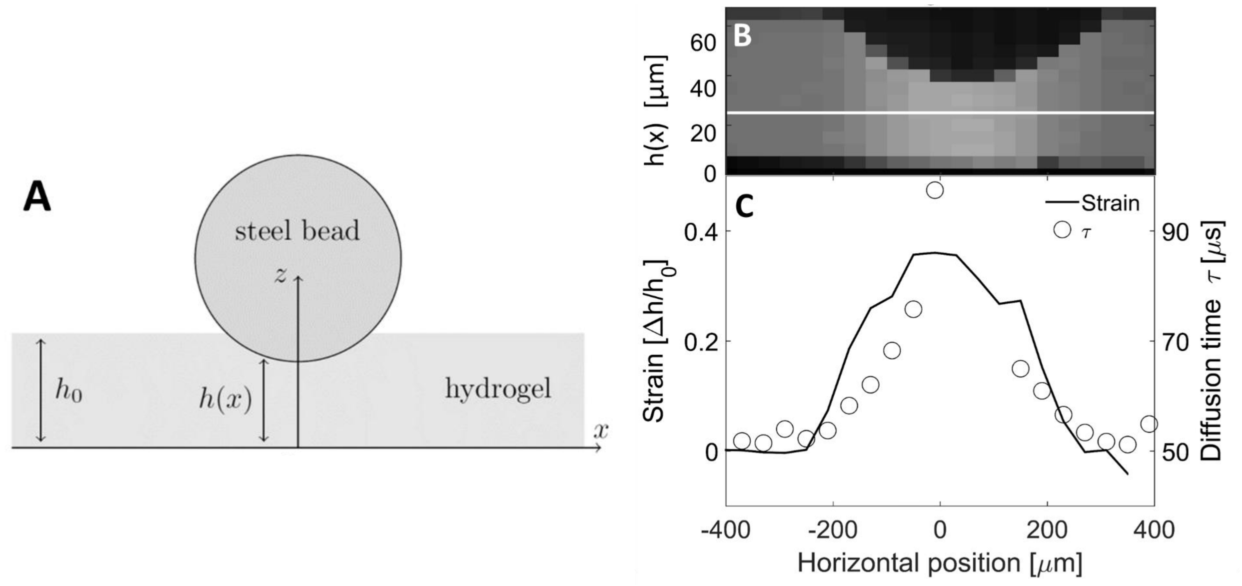

Figure 5.4 – FCS to measure compression of a steel bead on PAA. (a) schematic drawing of the experiment; a steel bead is placed on a layer of polyacrylamide of height h_0 on a cover-slip, the gel is observed from below with the microscope. (b) A pseudo image of the gel in XZ plane, at each horizontal position (x) an intensity profile is measured along the optical axis (z). (c) Also at each horizontal position an FCS measurement is taken at z = 25 μm (white line in (b)) and the measured τ_D is plotted for each position (x). The strain on the gel is also plotted for comparison. This experiment was carried out by F. Ingremeau.

is likely due to collapse of the polymer structure at this position. We can see a clear relationship of the strain and τ_D here.

Figure 5.5 shows a plot of τ_D versus the volume fraction for all the experiments shown above. Here it can be seen just how predictable the response of τ_D is to the change in volume fraction of the polymer, regardless of whether it is due to osmotic stress (beads or flat), mechanical stress, or no external stress. A very linear trend can be seen here in the region between 3 and 8 % volume fraction.

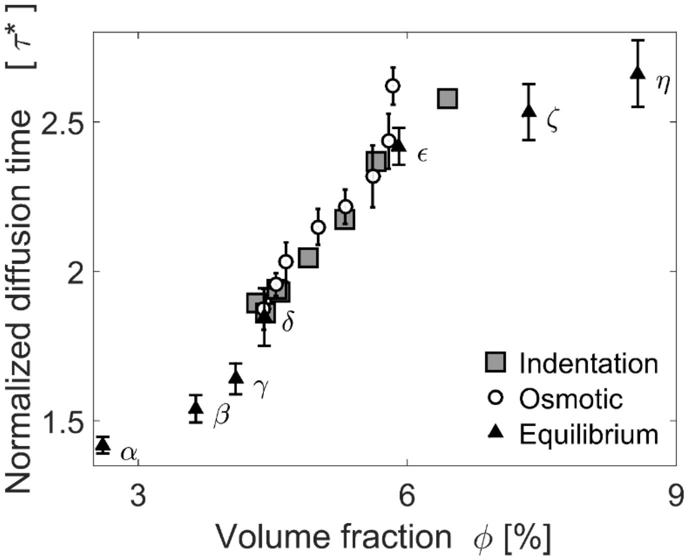

Figure 5.5 – Calibrating τ_D^* for an applied stress. τ_D^* of SRB as a function of the volume fraction ϕ of PAA. The PAA volume fraction has been varied in three different ways: (i) with a mechanical compression, by imposing a mechanical indentation, as shown in figure 5.4 (filled squares); (ii) via an osmotic compression, as reported in figure 5.3 (empty circles); (iii) using different formulations to vary the mass concentration of PAA (filled triangles).

These results have an important implication; regardless of the experimental conditions, τ_D gives us direct access to the volume fraction of the polymer an intrinsic property of the material. This bodes very well for the use of FCS and PAA beads as local pressure sensors in, for example, spheroids. Where in the imaging technique of Dolega et al. [173] each bead must be tracked careful to have relative strain measurements, with the τ_D measurements, the volume fraction can be determined from any bead (or more precisely, any population of beads). This would allow for much increased volume of measures as individual beads do not need to be tracked. This would be highly advantageous for experiments in spheroids and other tissue immediately reducing certain complexities and giving direct access to stress measurements at any time during tissue growth. However, there are many caveats. FCS is a delicate technique as we have shown many times in this thesis. With that in mind; can we get reliable FCS measurements everywhere we want to actually put the beads?

5.2
FCS measurements in spheroids

The next step is to use FCS to measure the absolute local stresses in spheroids.

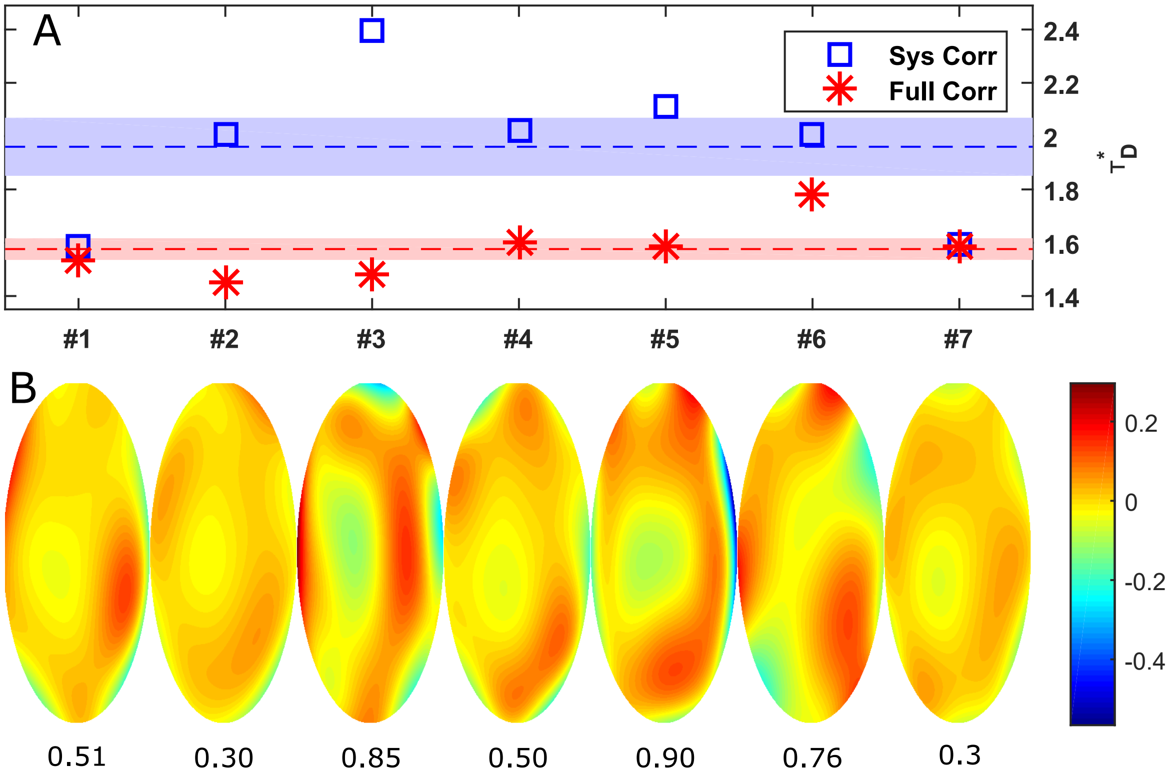

Figure 5.6 – Measurements of τ_D in PAA beads inside spheroids. (a) Measurements of τ_D inside 7 different PAA beads inside spheroids with the DM correcting for system aberrations (blue) and again after correcting for the aberrations at the FCS measurement site (Full correction, red). τ_D is normalised to its value in water in the same conditions. The mean values of the respective measurements with system and full correction are shown as dashed lines with their respective errors (SEM) shown as the shaded area around them. (b); the wave-front corrections corresponding to the numbered bead measurements above them. The reconstructed wavefronts from the measured Zernike modes (N=24) correspond to the difference between the system and full wave-front correction. The RMS values of the wave-fronts in radians are marked below each wave-front.

The spheroids we observe in these experiments were prepared principally by M. Dolega, following the protocol described for their preparation in [173] and [181]. Here we used the Myf cell lines(mouse embryonic fibroblast derived). Previously CT26 cells were used in the group [173,178,179] (amoung others) and serve as a great model for tumours in many respects, but optically they are a nightmare. They exhibit very high scattering relative to other cell lines the author used in observations in this thesis. The Myf cell line alleviates this problem very slightly, but enough that they gave us many useful measurements, although this is certainly not the sole reason we use them in the group.

The PAA beads used as pressure sensors are, in fact, the same beads are used in the experiments in chapter 4. They are highly transparent and have a refractive index very close to that of water (n=1.349 for 10.9 kPa [175]). We found from many experiments to calibrate the volume fraction vs τ_D in the beads that the beads induce very small optical aberrations when the observation volume is placed near their centre. In fact the observation has to be considerably outside the centre portion of the beads before there is enough perturbation of the optical path to bias the FCS measurements.

In short, this was not a bias large enough that AO could compensate for in the case of the calibration measurements described in the previous section. Even the spherical form of the beads did not bias the FCS curves until the observation volume approached the border of the bead and in this case it would be difficult to distinguish between; the effects of the optical interface within the observation volume, the effect of optical aberrations, and the inhomogeneity's of the material which could occur closer to the interface. All this said, aberrations or not, the most reliable measurements would always logically be from the centre of the beads, and also from the point of view of consistency.

However, once the beads were inside the spheroids, the situation is a lot different. The difficulty of high resolution optical measurements in spheroids is known in the group since the first experiments to measure diffusion of the extra-cellular matrix in spheroids using FCS by Leroux et al. [116]. It is in this situation that the bias of FCS measurements due to optical imhomogeneieties becomes clear and power of AO to combat this becomes apparent.

Figure 5.6 (a) shows τ_D measurements from 7 different beads inside a set of Myf spheroids, with the AO correcting for system aberrations alone (blue) and with full correction for the point of measurement (red). It can be seen from this data the bias introduced by the cell layers surrounding the beads. Measurements 1 and 7 for example correspond to beads which were close to the cover-slip and thus there was no significant bias due to aberrations. The other beads were at depths in the sample corresponding to 10-40 µm behind the cover-slip, relatively close to the surface in terms of the spheroids studied here, which were about 150 µm in diameter in the case of this particular experiment.

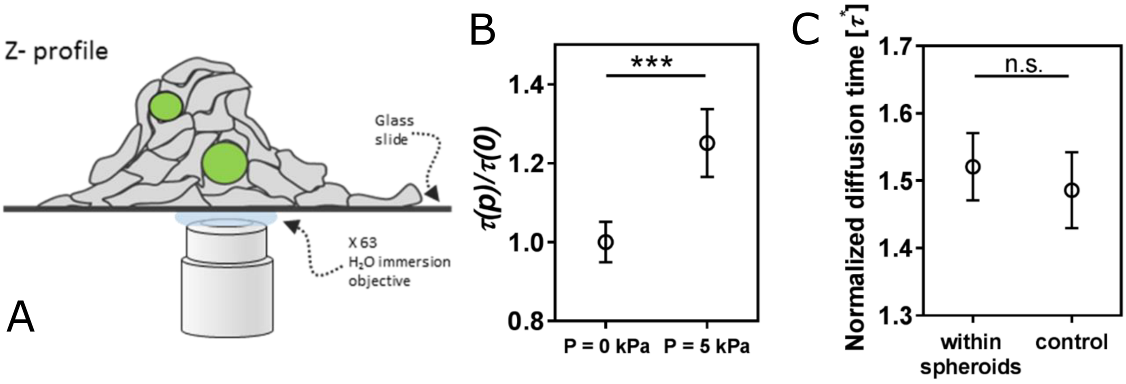

Figure 5.7 – Measuring the internal pressure of spheroids. A) Schematic representation of the spheroids observed. The spheroids were allowed to settle overnight on cover-slips before FCS measurements. This was done to ensure most stable conditions optically. B) Effect of externally applied isotropic compressive stress. Graph presents the normalised diffusion time ($\tau(P)/\tau(0)$) obtained within the beads incorporated within spheroids at P = 0 kPa ($\tau(0)$) and the same beads after an external stress of P = 5 kPa ($\tau(P)$) was applied. N=5; C) Measuring the pre-constraints imposed by the spheroids. Here we show the mean τ_D^* in between cells (within spheroids) or beads outside the spheroids (control). Some of these measurements are displayed in figure 5.6. (Error bars correspond to SEM. N=8 for the control; N=16 for beads within the spheroids). Error bars (SEM). For B) and C) we have used an unpaired t-test and obtained a p = 0.1336 (n.s.) for C) and p = 0.0001 (***) for B).

The amplitude of the aberrations biasing the measurements shown here is by no means large but their effect on τ_D measurements in considerable. Figure 5.6 (b) shows reconstructed phase maps from the measured Zernike aberrations at each position. Their corresponding RMS amplitude in radians is displayed below each wave-front. Figure 5.6 (a) shows also the mean τ_D measured in each case and their corresponding error (calculated as the square of the mean). From these few measurements the normalised diffusion time, τ_D^*, would be biased to 1.9 ±0.1 from the corrected measured τ_D^* of 1.58 ±0.04. Not only is the error more than doubled but without AO the measurements of τ_D^* would lead us to believe that there is an important pretension on the beads in the spheroids, up to 2 kPa in the case of these beads. In this case the external osmotic pressure on the spheroids is 0 kPa. In all cases of measurements in spheroids the AO was optimised using fluorescence intensity as a metric. This was chosen as the number of molecules was relatively high (N mol.>20) and often the measurements could have low count rates (see chapter 3 for a detailed discussion).

Figure 5.7 shows the combined results of our experiments in spheroids. In figure 5.7 (a) we show a schematic of the observation geometry and the spheroid. The spheroids were placed on Poly-L-lysine coated cover-slips overnight to stabilise them. A consequence is that they lost their spherical shape but this was intentional to provide a more stable sample for the proof of concept experiments, not only optically, but also to stop the spheroids moving during experiments. Figure 5.7 (b) shows the measurements of the change in τ_D^* from the case of no external pressure $\tau(0)$ to having an external osmotic stress of 5 kPa applied using dextran solution $\tau(p)$.

Figure 5.7 (c) shows the experiments on the spheroids with no osmotic pressure and compared to beads within (inside) and around spheroids (control). Here we see the pre-tension internally is in fact negligible, but this measurement would only be possible due to the application of AO. Looking at figure 5.6 we see that without AO τ_D^* would have overestimated to $\simeq 2$. Using this information and the calibration curves for the 3 kPa beads (figure 5.3), the pre-tension here would have been estimated as $\simeq 6$ kPa. We do not have the system AO correction case for comparison in the case of the spheroids undergoing mechanical stress. This would obviously double the measurement time, requiring twice the number of FCS measurements, which we could not afford here.

5.3
Discussion

The results shown here demonstrate a method of absolute pressure measurements inside spheroids. Using these experiments we managed to show definitively that the pre-tension of the spheroids is < 1 kPa. This is currently the limit of the precision of this technique using the 3 kPa beads.

These results would not have been possible without AO. In the group we were not fully aware of the significance of AO for these quantitative measurements until we began to compare our results here; with a AO correction optimised to the system and after full AO correction optimised at the measurement site immediately before acquisition. Not only does the AO significantly reduce the noise on the τ_D^* measurements (from one bead to another) but it significantly reduces the bias on these quantitative measurements.

The measurements here correspond to relatively shallow depths in the spheroids (< 40µm) when compared to the measurements of Dolega et al. [173] in which spheroids up to 500 µm in diameter were characterised for almost their full diameter. Given, the aberrations measured at the shallow depths here, and their impact on τ_D^*, we can safely say that one could never hope to have meaningful FCS measurements for full spheroids, such as Dolega et al., without AO even if the S/N was there to see what's happening. In their experiments they used objectives with low NA and wide-field illumination, thus removing the problem of coherency. Although the fluorescence signal is equally scattered as in confocal, due to the low NA they are only dependent on low angle light which has a far higher likelihood of being detected at the expense of lower resolution. This is not limiting in their case however.

This brings us swiftly to the biggest problem encountered for these measurements, optical scattering. FCS geometries require well corrected, high NA objectives to achieve the small observation volumes required for the technique's sensitivity. This is exactly contrary to the conditions required for effective volume imaging where the common tactic is to lower the NA of the excitation geometry significantly to reduce scattering, at the cost of lower resolution.

One could combat this problem on two fronts in order to reduce scattering and keep the resolution required for FCS: use AO systems to combat the lower order aberrations which perturb the FCS volume, and switch to two-photon scheme.

The advantages of a TPEF system would be two fold; firstly much reduced scattering of the excitation beam due to its longer wave-length, generally in the near infrared range (0.8 - 1.4 µm). Secondly, a much increased detector area and no physical stop, such as the pinhole for optical sectioning, as the sectioning is a natural product of the non-linear excitation regime [15]. A two-photon microscope was originally intended for the project but eventually this had to be abandoned due to time constraints.

There are other technical constraints which also limited our ability to take this experiment further under this geometry. The number of modalities used in these experiments was an issue in terms of time per experiment. For each τ_D^* measurement a bead first had to be found. This meant finding a spheroid which also contained one or more beads in bright-field observation. Then we have to switch to wide-field fluorescence to see the beads (green fluorescent). We should note here that the microscope has one objective with a 300 µm FOV, enough for one spheroid at a time and that the filters, cameras, ports and sources for wide-field viewing are all manually controlled. Once a bead of interest was located the camera port had to be switched to use the confocal (manual control) and all sources had to be switched off and wide-field filters rotated out of the way. Once in confocal mode the locating of the bead in (x, y, z) has to be verified. The bead is green fluorescent with low concentration SRB flowing through it, the spheroid has SRB diffusing in its extra-cellular matrix. Here we only see one channel, the SRB. The contrast of the bead is now therefore extremely low, generally only its shape can distinguish it in confocal.

Once the observation volume is positioned the AO must be optimised. These experiments were done while we were still doing the experiments of chapter 3 to understand the best way to optimise the AO system. Also, our algorithms are not highly time optimised. Though the measurements per bias per mode are quick (20-200 ms), it takes many modes and loops to verify best correction (N=24, generally for 2-3 loops). We can expect 10 - 20 s for this step at least. Finally the FCS measurements must be carried out, this takes at least 30 s. Some of these experiments also suffered from photo-bleaching effects so given the time taken to overcome all the technical setup, most of the usable photons could be used up. Sometimes we can change the power to compensate but again the power control of the laser is manual. Then everything has to be recorded and stored correctly. With two people this can be done in parallel of course.

5.4
Conclusions

Here we have presented a method to have possible direct stress measurements inside spheroids and tissues using measurements of τ_D in calibrated pressure sensors, PAA beads. We demonstrated that the known changes in volume fraction, which we induced in the polymer using various techniques, is proportional to the changes in measured τ_D due to the hindered diffusion of fluorescent molecules within the polymer. We also demonstrated that although the technique gives direct access to an absolute measurement of the volume fraction of the polymer that it can be easily bias by optical aberrations. Here we used AO to correct for this bias and also reduce the noise in the measurements. However, even with AO, this technique is still quite limited leaving aside the technically issues discussed here. The measurements inside spheroids were all taken at depths < 60 µm, which is often only a fraction of the radius of the size of spheroids generally of interest in the literature (100 - 1000 µm radius). It remains to be seen if technologically advances in FCS measurements in aberrating and scattering environments can push for viable measurements in these conditions. Certainly some enhancements could be expected from readily available techniques such as two-photon FCS to reduce scattering somewhat, and possibly more from advanced optical techniques to combat scattering and aberrations [60, 90], but will these gains be enough to answer the questions of the local physiological effects of pressure on growing tumours?

Most modern research microscopes have optimisations and electronics to overcome a lot of the technical issues mentioned. To have truly quantitative measurements these are the technical problems that need to be address. This requires a lot of development and resources on the observation side which we underestimated greatly here. Nevertheless we managed to obtain the first measurements of their kind with the system, which would only be possible due to the development of this system and the combined effort of the entire team, the microscope developed in this thesis here, and before [114–116, 122], is only part of the puzzle.

The author would like to acknowledge here the massive effort of the entire team in achieving these results. This project began long before this thesis with the combined research of A. Delon and G. Cappello on their respective projects before the idea to combine their research came about through the work of C.E. Leroux. The results in this project presented represent a milestone in their large research effort of which the author is proud to have helped contribute. The author would also like to acknowledge the immense effort of M. Dolega in driving much of the work presented in this chapter, and provided a liaison for every aspect of the project. Also F. Ingremeau for his scientific contributions and FCS measurements.

Chapter 6
Conclusions

In this thesis we have examined the methods and applications of adaptive optics for fluorescence correlation spectroscopy. We have examined the materials involved in implementing AO in FCS systems, looked at the design of such systems, characterised the methods and metrics used in AO system for FCS, quantified the effect of aberrations on FCS measurements while demonstrating and quantifying the effectiveness of AO to counter these aberrations, and finally demonstrated a practical use for AO FCS where we demonstrated that the bias of aberrations of the FCS measurements would significantly bias quantitative measurements without using AO.

In chapter 2 we looked at the implementation of an open-loop adaptive optics system in a confocal microscope. The implementation in question here, ConfocAO, already existed in a similar form [115, 116, 122] however since a rebuild was necessitated near the beginning of this thesis project we took the opportunity to assess the development of the entire system and implement some improvements. We examined the optical performance of the experiment using LASSO, a ray tracing solution developed in the IPAG lab (Université Grenoble Alpes). We then discussed the implementation of a control and software engine to facilitate the experiments of this thesis and hopefully more going forward. Finally we discussed the methods to calibrate and characterise the microscope and the AO system, and demonstrated its performances.

Originally it was not intended for this system to be used for this thesis. The original idea was to develop a multi-photon microscope with an AO system and much time of this thesis was devoted to its implementation. However it did not see its development completed, except for the control and software which is now used in ConfocAO. This was due to an unfortunate sequence of delays with materials which also were delaying other parts of the project where other members of the team were already far advanced in their respective research. In retrospect it was a very prudent decision to abandon its development in favour of continued research using ConfocAO as it led to the results of chapters 3, 4 and, arguably most importantly, 5, as it involved the combined resources of the entire team, and the understandings gained from the other research shown here.

In chapter 3 we examine the metrics used for AO optimisation in an FCS instrument. The case study here is very specific but results we have shown here demonstrate its value for our understanding of the AO optimisation in an FCS system. Here we examined two FCS metrics specifically, CR and ϵ, both of which can be determined in real time and thus make them useful for AO. We characterised the noise of both metrics experimentally and related this to the theoretical expectations. Crucially here, for low concentration fluorescent molecules, we found that the noise on CR is not simple shot noise, which impacts its use as a metric significantly in FCS when compared to other modalities [78]. We then looked at the sensitivities of both metrics for low order aberrations and measured the accuracy of AO corrections using either metric. We showed the theory was in agreement with out experimental results and demonstrated two different regimes which, for highest accuracy, favoured either CR as metric (in the case of high concentration dim molecules,) or ϵ (in the case of low concentration bright molecules.)

In the case of larger aberrations (> 0.5 rad), in general it is more advantageous to use CR as a metric for AO, especially since the S/N of ϵ is massively diminished for aberration amplitudes beyond 1 rad RMS (figure 3.3). Yet there are certain intermediate cases where ϵ can still be more accurate because the S/N of ϵ increases with diminishing aberration, which is opposite to the case of CR. Thus it is more likely gains can continued to be made with successive loop iterations.

However, rather than using just either one of these metrics, it should be apparent that the best accuracy and most efficient correction can be had by using a combination of the two metrics. We used a simple combination in some experiments in this thesis, for example in figure 4.11. Here the combination was simply to correct rapidly using CR to test for large amplitude aberrations where quick gains could be had, and then ϵ was used in subsequent loops to gain the highest accuracy. This tactic was also employed in chapter 5.

Such a tactic is very simple and could obviously be improved upon much further, especially with the emergence of more robust metric optimisation algorithms [191, 192]. Also, the use of combined metrics for AO optimisation has also been demonstrated successfully in a STED microscope [84]. However, the metrics of CR and ϵ are simple and requires only the presence of a diffusing fluorescent molecule, which is quite common place in fluorescence microscopy! Given *a priori* knowledge of the noise statistics of the two metrics, which can be easily determined for many situations, as we showed here, a weighted two metric modal optimisation scheme could be imagined.

In Leroux et al. [114] the use of FCS metrics as metrics for AO was likened to having a guide star at any point in the sample where a diffusing fluorophores is present. This implies not only that we have a point to optimise the AO but also that we have a measurement of the quality of the wave-front, which is yet another useful property of ϵ. Given that we know to a certain accuracy its dependence on the total RMS amplitude, we can determine to a degree the likelihood that the correction is well optimised. Further, given that ϵ is mostly only sensitivity where the Strehl > 0.9 , it is a useful indicator of the total residual aberration even in relatively unknown specimens. This could be developed as a fast metric for such.

In chapter 4 we examined the effect of aberrations on FCS metrics. Here we used a simple technique to create phase aberrations with varying amplitude and spatial frequency in order to study their effects. It was already known from the literature that low order aberrations have a strong biasing effect on FCS [10, 114], but that, on the contrary, light scattering has a very small impact on FCS [116, 169]. Here we wanted to gain an understanding of the transition between these two regimes.

Through our experiments we were able to observe the transition between these two regimes by propagating a phase screen to various distances from the focal point of our microscope beam. We observed that the characteristic size of the aberrators determined the propagation distance at which the aberrating regime transitioned to the scattering regime. Once in the pure scattering regime, continued evolution of complexity had no further effect on intensity attenuation and had little to no effect on FCS metrics of N mol and τ_D which renormalised to their unaberrated values at constant coverage ratio.

Through this and further experiments looking at the sensitivity of FCS metrics to individual Zernike modes we were able to quantify the maximum aberration complexity which would have an effect on τ_D and N mol which is 2 r^{-1} and 3.5 r^{-1}, respectively, where r is the pupil radius. This determines the maximum complexity of aberrations necessary to correct in order to have unbiased measurements of these metrics. We performed experiments using AO correction in the same samples and showed that even correcting only a fraction of the predicted necessary modes (N=24) that τ_D could be renormalised to within 10% of its unbiased value in the majority of cases. N mol. is not normalised to the same degree but this is to be expected as it is sensitive to aberrations with up to twice the complexity compared to τ_D.

These results bode very well for the possibility of performing FCS measurements in samples with both a complex spatial aberration structure and scattering properties. Given a certain optical geometry we can determine the degree of wave-front correction required in order to have a given degree of certainty on the FCS metrics of N mol. and τ_D. This also has implications for imaging using AO as the same parameters will determine the distortion of the PSF, where the limit of the impact of aberrations on the volume of the PSF can be determined and modes with increasing complexity beyond this limit will only affect the S/N.

In chapter 5 we used FCS to perform quantitative measurements in spheroids where they would otherwise be largely bias without the use of AO. In this chapter we apply the knowledge obtained from the experiments of chapter 3 and 4 to gain access to in situ measurements of the intrinsic properties of tissues under stress.

Here we used compressible material with a weakly concentrated, freely diffusing fluorophores (SRB) inside, which could also freely diffuse in and out of the bead. Therefore, the only hindrance to the molecules' diffusion would be the polymer volume fraction. We showed a very linear relationship between the polymer (polyacrylamide) volume fraction and the measured τ_D via FCS (Figure 5.5). The relationship is constant regardless of whether the volume fraction is determined by the composition of the polymer at synthesis or whether the volume fraction is artificially induced via stress. This makes FCS ideal for volume fraction measurements of the polymer and hence, the external stress on the polymer which can be calibrated.

Although the measurements of τ_D are relatively unbiased in the PAA beads used in these experiments by themselves, we have shown that the complex aberrations induced by only a small layer of cells surrounding these beads can significantly bias the τ_D measurements. An example of such measurements can be found in figure 5.6 where we see that the τ_D would be biased by a factor of 1.25 even though the measured phase aberration in all cases is small (< 1 rad RMS for 24 modes). In the case of these measurements the estimated stress would be bias by 2 kPa without AO.

The results of these experiments are very promising for continued experiments using FCS as an optical sensor for pressure. There are definitely some issues to be ironed out if the method is to become a protocol to be used as such. Some of the more technical issues were outlined in the discussion in chapter 5 relating to equipment. These issues were unfortunate and could be resolved with some further development and equipment but this is not always a luxury a research team can invest in. Hopefully with the advent of some commercial AO systems coupled with commercial microscopes much of these technicalities could be overcome, paving the way for a viable protocol. Other than these technical issues there are other questions that need to be addressed; what is the certainty of the AO correction? This is important if we take for example the same set of measurements, can we be certain that the residual bias due to the uncorrected modes is not significant?

This relates back to the research of chapter 3 where we talked about the *in situ* sensitivity of an aberration mode being used as a metric for the correction quality. It could be said that τ_D is an excellent metric to determine the quality of an observation volume (PSF) [7, 11] however this is no good to us when we wish to quantify effects that interact with τ_D in the first instance. An often employed tactic in sensor-less AO is iterate the correction until the metric converges. This is a sound tactic given that we can quantify the number of degrees of freedom (aberration modes) that are required, and a tactic regularly employed in experiments this thesis, but this is wasteful. Not only does this require many photons, even in a photon rich environment the time sacrificed to test all modes is significant. This is partly why in this thesis we mainly limited ourselves to 24 aberration modes, beyond this the gains were too rare to justify the investment of time. However, with a well defined metric to determine the residual the correction could be halted as soon as a threshold is achieved.

Having a well defined metric to determine the residual aberration also requires aberration modes that are very orthogonal and normalised in terms of a metric. There has been significant efforts in the literature to produce normalised orthogonal aberration modes for a given metric [77, 79], however, depending on the modality used, these procedures can be somewhat complicated and time consuming compared to the gains to be had from the procedure (D. Debarre, private communication). Indeed, for 24 aberration modes alone, using the technique in [77] would require 264 couplings to be investigated times the number of measurements used per coupling and the number of couplings scales with the square of the number of modes. Initial experiments in our lab into decoupling of modes were not fruitful and since the cross-talk effect was determined to be sufficiently low as not to hinder the AO correction in our experiments shown here, it was not pursued further. However, the author believes it would be advantageous to have an aberration mode basis based on the geometry of the DM, such as in Thayil et al. [79], in order to investigate metrics for total residual aberration.

Given the bias effects of aberrations on FCS measurements, these results should certainly serve as a warning for potential bias when performing FCS measurements in a complex specimen. Also, the benefit of an AO system for FCS measurements is mainly that it opens up access to FCS measurements in specimen previously thought prohibitive due to aberrations.

Bibliography

[1] D. Magde, E. Elson, and W. W. Webb, "Thermodynamic fluctuations in a reacting system—measurement by fluorescence correlation spectroscopy," Physical Review Letters **29**, 705 (1972).

[2] S. Aragon and R. Pecora, "Fluorescence correlation spectroscopy as a probe of molecular dynamics," The Journal of Chemical Physics **64**, 1791–1803 (1976).

[3] E. L. Elson and D. Magde, "Fluorescence correlation spectroscopy. i. conceptual basis and theory," Biopolymers **13**, 1–27 (1974).

[4] F. A. Thomas, I. Visco, Z. Petrášek, F. Heinemann, and P. Schwille, "Introducing a fluorescence-based standard to quantify protein partitioning into membranes," Biochimica et Biophysica Acta (BBA)-Biomembranes **1848**, 2932–2941 (2015).

[5] D. Wöll, "Fluorescence correlation spectroscopy in polymer science," Rsc Advances **4**, 2447–2465 (2014).

[6] K. Bacia, E. Haustein, and P. Schwille, "Fluorescence correlation spectroscopy: principles and applications," Cold Spring Harbor Protocols **2014**, pdb–top081802 (2014).

[7] S. Rüttinger, V. Buschmann, B. Krämer, R. Erdmann, R. Macdonald, and F. Koberling, "Comparison and accuracy of methods to determine the confocal volume for quantitative fluorescence correlation spectroscopy," Journal of microscopy **232**, 343–352 (2008).

[8] R. Rigler, Ü. Mets, J. Widengren, and P. Kask, "Fluorescence correlation spectroscopy with high count rate and low background: analysis of translational diffusion," European Biophysics Journal **22**, 169–175 (1993).

[9] R. W. Cole, T. Jinadasa, and C. M. Brown, "Measuring and interpreting point spread functions to determine confocal microscope resolution and ensure quality control," Nature protocols **6**, 1929–1941 (2011).

[10] J. Enderlein, I. Gregor, D. Patra, T. Dertinger, and U. B. Kaupp, "Performance of fluorescence correlation spectroscopy for measuring diffusion and concentration," ChemPhysChem **6**, 2324–2336 (2005).

[11] S. T. Hess and W. W. Webb, "Focal volume optics and experimental artifacts in confocal fluorescence correlation spectroscopy," Biophysical journal **83**, 2300–2317 (2002).

[12] J. Widengren, U. Mets, and R. Rigler, "Fluorescence correlation spectroscopy of triplet states in solution: a theoretical and experimental study," The Journal of Physical Chemistry **99**, 13368–13379 (1995).

[13] J. Mertz, *Introduction to optical microsopy* (Roberts and Company Publishers, Colorado, USA, 2010).

[14] C. J. R. Sheppard and M. Gu, "Image formation in two-photon fluorescence microscopy," Optik **86**, 104–106 (1990).

[15] W. Denk, J. Strickler, and W. Webb, "Two-photon laser scanning fluorescence microscopy." Science **248**, 73–76– (1990).

[16] M. Eigen and R. Rigler, "Sorting single molecules: application to diagnostics and evolutionary biotechnology," Proceedings of the National Academy of Sciences **91**, 5740–5747 (1994).

[17] S. Maiti, U. Haupts, and W. W. Webb, "Fluorescence correlation spectroscopy: diagnostics for sparse molecules," Proceedings of the National Academy of Sciences **94**, 11753–11757 (1997).

[18] E. L. Elson, "Fluorescence correlation spectroscopy: past, present, future," Biophysical journal **101**, 2855–2870 (2011).

[19] S. W. Hell and J. Wichmann, "Breaking the diffraction resolution limit by stimulated emission: stimulated-emission-depletion fluorescence microscopy," Opt. Lett. **19**, 780–782 (1994).

[20] E. Betzig, G. H. Patterson, R. Sougrat, O. W. Lindwasser, S. Olenych, J. S. Bonifacino, M. W. Davidson, J. Lippincott-Schwartz, and H. F. Hess, "Imaging intracellular fluorescent proteins at nanometer resolution," Science **313**, 1642–1645 (2006).

[21] C. J. R. Sheppard and M. Gu, "Aberration compensation in confocal microscopy," Appl. Opt. **30**, 3563–3568 (1991).

[22] D. Day and M. Gu, "Effects of refractive-index mismatch on three-dimensional optical data-storage density in a two-photon bleaching polymer," Appl. Opt. **37**, 6299–6304 (1998).

[23] M. Schwertner, M. J. Booth, and T. Wilson, "Simple optimization procedure for objective lens correction collar setting," Journal of Microscopy **217**, 184–187 (2005).

[24] S. Hell, G. Reiner, C. Cremer, and E. H. K. Stelzer, "Aberrations in confocal fluorescence microscopy induced by mismatches in refractive index," Journal of Microscopy **169**, 391–405 (1993).

[25] P. Török, P. Varga, and G. Németh, "Analytical solution of the diffraction integrals and interpretation of wave-front distortion when light is focused through a planar interface between materials of mismatched refractive indices," J. Opt. Soc. Am. A **12**, 2660–2671 (1995).

[26] A. Egner and S. W. Hell, "Equivalence of the huygens-fresnel and debye approach for the calculation of high aperture point-spread functions in the presence of refractive index mismatch," Journal of Microscopy **193**, 244–249 (1999).

[27] M. Schwertner, M. Booth, and T. Wilson, "Characterizing specimen induced aberrations for high na adaptive optical microscopy," Opt. Express **12**, 6540–6552 (2004).

[28] M. Schwertner, M. J. Booth, M. A. A. Neil, and T. Wilson, "Measurement of specimen-induced aberrations of biological samples using phase stepping interferometry," Journal of Microscopy **213**, 11–19 (2004).

[29] J. Zeng, P. Mahou, M.-C. Schanne-Klein, E. Beaurepaire, and D. Débarre, "3d resolved mapping of optical aberrations in thick tissues," Biomed. Opt. Express **3**, 1898–1913 (2012).

[30] F. P. Bolin, L. E. Preuss, R. C. Taylor, and R. J. Ference, "Refractive index of some mammalian tissues using a fiber optic cladding method," Appl. Opt. **28**, 2297–2303 (1989).

[31] F. Charriere, A. Marian, F. Montfort, J. Kuehn, T. Colomb, E. Cuche, P. Marquet, and C. Depeursinge, "Cell refractive index tomography by digital holographic microscopy," Opt. Lett. **31**, 178–180 (2006).

[32] G. J. Tearney, M. E. Brezinski, J. F. Southern, B. E. Bouma, M. R. Hee, and J. G. Fujimoto, "Determination of the refractive index of highly scattering human tissue by optical coherence tomography," Opt. Lett. **20**, 2258–2260 (1995).

[33] R. K. Tyson, *Principles of Adaptive Optics (3rd Ed.)* (CRC Press, Boca Raton, FL, 2011).

[34] J. Liang, D. R. Williams, and D. T. Miller, "Supernormal vision and high-resolution retinal imaging through adaptive optics," J. Opt. Soc. Am. A **14**, 2884–2892 (1997).

[35] M. Booth, M. Neil, and T. Wilson, "Aberration correction for confocal imaging in refractive-index-mismatched media," Journal of Microscopy **192**, 90–98 (1998).

[36] M. J. Booth and T. Wilson, "Strategies for the compensation of specimen-induced spherical aberration in confocal microscopy of skin," Journal of Microscopy **200**, 68–74 (2000).

[37] M. J. Booth and T. Wilson, "Refractive-index-mismatch induced aberrations in single-photon and two-photon microscopy and the use of aberration correction," Journal of Biomedical Optics **6**, 266–272 (2001).

[38] D. Ganic, X. Gan, and M. Gu, "Reduced effects of spherical aberration on penetration depth under two-photon excitation," Appl. Opt. **39**, 3945–3947 (2000).

[39] M. Schwertner, M. J. Booth, and T. Wilson, "Specimen-induced distortions in light microscopy," Journal of Microscopy **228**, 97–102 (2007).

[40] J. W. O'Byrne, P. W. Fekete, R. Arnison, H. Zhau, M. Serrano, D. Philp, W. Sudiarta, and C. J. Cogswell, "Adaptive opitcs in confocal microscopy," in "2nd International Workshop on Adaptive Optics for Industry and Medicine," G. D. Love, ed. (World Scientific, 1999), pp. 85–90.

[41] O. Albert, L. Sherman, G. Mourou, T. B. Norris, and G. Vdovin, "Smart microscope: an adaptive optics learning system for aberration correction in multiphoton confocal microscopy," Opt. Lett. **25**, 52–54 (2000).

[42] L. Sherman, J. Y. Ye, O. Albert, and T. B. Norris, "Adaptive correction of depth-induced aberrations in multiphoton scanning microscopy using a deformable mirror," Journal of Microscopy **206**, 65–71 (2002).

[43] M. J. Booth, "Adaptive optical microscopy: the ongoing quest for a perfect image," Light: Science & Applications **3**, e165 (2014).

[44] J. Feinleib, S. G. Lipson, and P. F. Cone, "Monolithic piezoelectric mirror for wavefront correction," Applied Physics Letters **25**, 311–313 (1974).

[45] J. E. Pearson and S. Hansen, "Experimental studies of a deformable-mirror adaptive optical system," J. Opt. Soc. Am. **67**, 325–332 (1977).

[46] J. C. Dainty, A. V. Koryabin, and A. V. Kudryashov, "Low-order adaptive deformable mirror," Appl. Opt. **37**, 4663–4668 (1998).

[47] T. Bifano, J. Perreault, R. Krishnamoorthy Mali, and M. Horenstein, "Microelectromechanical deformable mirrors," Selected Topics in Quantum Electronics, IEEE Journal of **5**, 83 –89 (1999).

[48] D. Dagel, W. Cowan, O. Spahn, G. Grossetete, A. Grine, M. Shaw, P. Resnick, and J. Jokiel, B., "Large-stroke MEMS deformable mirrors for adaptive optics," Microelectromechanical Systems, Journal of **15**, 572 – 583 (2006).

[49] S. Bonora and L. Poletto, "Push-pull membrane mirrors for adaptive optics," Opt. Express **14**, 11935–11944 (2006).

[50] A. N. Simonov, S. Hong, and G. Vdovin, "Piezoelectric deformable mirror with adaptive multiplexing control," Optical Engineering **45**, 070501–070501–3 (2006).

[51] P. Laird, N. Caron, M. Rioux, E. F. Borra, and A. Ritcey, "Ferrofluidic adaptive mirrors," Appl. Opt. **45**, 3495–3500 (2006).

[52] G. Vdovin and M. Loktev, "Deformable mirror with thermal actuators," Opt. Lett. **27**, 677–679 (2002).

[53] M. J. Booth, "Adaptive optics in microscopy," Philosophical Transactions of the Royal Society A: Mathematical, Physical and Engineering Sciences **365**, 2829–2843 (2007).

[54] E. Fernandez and P. Artal, "Membrane deformable mirror for adaptive optics: performance limits in visual optics," Opt. Express **11**, 1056–1069 (2003).

[55] N. Devaney, E. Dalimier, T. Farrell, D. Coburn, R. Mackey, D. Mackey, F. Laurent, E. Daly, and C. Dainty, "Correction of ocular and atmospheric wavefronts: a comparison of the performance of various deformable mirrors," Applied optics **47**, 6550–6562 (2008).

[56] E. Dalimier and C. Dainty, "Comparative analysis of deformable mirrors for ocular adaptive optics," Opt. Express **13**, 4275–4285 (2005).

[57] M. Booth, T. Wilson, H.-B. Sun, T. Ota, and S. Kawata, "Methods for the characterization of deformable membrane mirrors," Appl. Opt. **44**, 5131–5139 (2005).

[58] M. A. A. Neil, M. J. Booth, and T. Wilson, "Closed-loop aberration correction by use of a modal zernike wave-front sensor," Opt. Lett. **25**, 1083–1085 (2000).

[59] Neil, Wilson, and Juskaitis, "A wavefront generator for complex pupil function synthesis and point spread function engineering," Journal of Microscopy **197**, 219–223 (2000).

[60] J. Tang, R. N. Germain, and M. Cui, "Superpenetration optical microscopy by iterative multiphoton adaptive compensation technique," Proceedings of the National Academy of Sciences **109**, 8434–8439 (2012).

[61] SPIE, ed., *Deformable mirror based remote focusing for fast three-dimensional microscopy*, vol. 9713 (2016).

[62] P. Lanigan, I. Munro, E. Grace, D. Casey, J. Phillips, D. Klug, O. Ces, and M. Neil, "Dynamical hologram generation for high speed optical trapping of smart droplet microtools," Biomedical Optics Express **3**, 1609 (2012).

[63] F. Rooms, S. Camet, J. Charton, J.-F. Curis, and L. Jocou, "A new deformable mirror and experimental setup for free-space optical communication," in "SPIE LASE: Lasers and Applications in Science and Engineering," (International Society for Optics and Photonics, 2009), pp. 71990O–71990O.

[64] J. Charton, Z. Hubert, L. Jocou, E. Stadler, J.-L. Beuzit, and P. Kern, "Deformable mirror," Patent (2010). US Patent 7,733,550.

[65] O. Cugat, S. Basrour, C. Divoux, P. Mounaix, and G. Reyne, "Deformable magnetic mirror for adaptive optics: technological aspects," Sensors and Actuators A: Physical **89**, 1–9 (2001).

[66] H. W. Babcock, "The possibility of compensating astronomical seeing," Publications of the Astronomical Society of the Pacific **65**, 229–236 (1953).

[67] J. W. Hardy, *Adaptive optics for astronomical telescopes* (Oxford University Press on Demand, 1998).

[68] M. A. A. Neil, M. J. Booth, and T. Wilson, "New modal wave-front sensor: a theoretical analysis," J. Opt. Soc. Am. A **17**, 1098–1107 (2000).

[69] M. A. A. Neil, R. Juškaitis, M. J. Booth, T. Wilson, T. Tanaka, and S. Kawata, "Adaptive aberration correction in a two-photon microscope," Journal of Microscopy **200**, 105–108 (2000).

[70] M. J. Booth, M. A. A. Neil, and T. Wilson, "New modal wave-front sensor: application to adaptive confocal fluorescence microscopy and two-photon excitation fluorescence microscopy," J. Opt. Soc. Am. A **19**, 2112–2120 (2002).

[71] M. J. Booth, M. A. A. Neil, R. JuÅ¡kaitis, and T. Wilson, "Adaptive aberration correction in a confocal microscope," Proceedings of the National Academy of Sciences **99**, 5788–5792 (2002).

[72] P. Marsh, D. Burns, and J. Girkin, "Practical implementation of adaptive optics in multiphoton microscopy," Opt. Express **11**, 1123–1130 (2003).

[73] M. Booth, "Wave front sensor-less adaptive optics: a model-based approach using sphere packings," Opt. Express **14**, 1339–1352 (2006).

[74] S. M. Goldfeld, R. E. Quandt, and H. F. Trotter, "Maximization by quadratic hill-climbing," Econometrica: Journal of the Econometric Society pp. 541–551 (1966).

[75] W. Lukosz and M. Marchand, "Optischen abbildung unter Überschreitung der beugungsbedingten auflösungsgrenze," Optica Acta: International Journal of Optics **10**, 241–255 (1963).

[76] J. Braat, "Polynomial expansion of severely aberrated wave fronts," J. Opt. Soc. Am. A **4**, 643–650 (1987).

[77] D. Débarre, E. J. Botcherby, M. J. Booth, and T. Wilson, "Adaptive optics for structured illumination microscopy," Opt. Express **16**, 9290–9305 (2008).

[78] A. Facomprez, E. Beaurepaire, and D. Débarre, "Accuracy of correction in modal sensorless adaptive optics," Opt. Express **20**, 2598–2612 (2012).

[79] A. Thayil and M. J. Booth, "Self calibration of sensorless adaptive optical microscopes," Journal of the European Optical Society-Rapid publications **6** (2011).

[80] D. Debarre, M. J. Booth, and T. Wilson, "Image based adaptive optics through optimisation of low spatial frequencies," Opt. Express **15**, 8176–8190 (2007).

[81] D. Debarre, E. J. Botcherby, T. Watanabe, S. Srinivas, M. J. Booth, and T. Wilson, "Image-based adaptive optics for two-photon microscopy," Opt. Lett. **34**, 2495–2497 (2009).

[82] N. Olivier, D. Débarre, and E. Beaurepaire, "Dynamic aberration correction for multiharmonic microscopy," Opt. Lett. **34**, 3145–3147 (2009).

[83] I. Izeddin, M. E. Beheiry, J. Andilla, D. Ciepielewski, X. Darzacq, and M. Dahan, "PSF shaping using adaptive optics for three-dimensional single-molecule super-resolution imaging and tracking," Opt. Express **20**, 4957–4967 (2012).

[84] T. J. Gould, D. Burke, J. Bewersdorf, and M. J. Booth, "Adaptive optics enables 3d sted microscopy in aberrating specimens," Opt. Express **20**, 20998–21009 (2012).

[85] C. Bourgenot, C. D. Saunter, J. M. Taylor, J. M. Girkin, and G. D. Love, "3d adaptive optics in a light sheet microscope," Opt. Express **20**, 13252–13261 (2012).

[86] E. J. Gualda, J. M. Bueno, and P. Artal, “Wavefront optimized nonlinear microscopy of ex vivo human retinas,” Journal of Biomedical Optics **15**, 026007–026007–7 (2010).

[87] J. M. Girkin, S. Poland, and A. J. Wright, “Adaptive optics for deeper imaging of biological samples,” Current Opinion in Biotechnology **20**, 106 – 110 (2009).

[88] D. Debarre, A. Facomprez, and E. Beaurepaire, “Assessing correction accuracy in image-based adaptive optics,” in “SPIE MOEMS-MEMS,” , vol. 8253 S. S. Olivier, T. G. Bifano, and J. Kubby, eds. (SPIE, 2012), vol. 8253, p. 82530F.

[89] W. Lubeigt, S. P. Poland, G. J. Valentine, A. J. Wright, J. M. Girkin, and D. Burns, “Search-based active optic systems for aberration correction in time-independent applications,” Appl. Opt. **49**, 307–314 (2010).

[90] L. Kong and M. Cui, “In vivo fluorescence microscopy via iterative multi-photon adaptive compensation technique,” Optics express **22**, 23786–23794 (2014).

[91] N. Ji, D. E. Milkie, and E. Betzig, “Adaptive optics via pupil segmentation for high-resolution imaging in biological tissues,” Nat Meth **7**, 141–147 (2010).

[92] D. E. Milkie, E. Betzig, and N. Ji, “Pupil-segmentation-based adaptive optical microscopy with full-pupil illumination,” Opt. Lett. **36**, 4206–4208 (2011).

[93] J. L. Beverage, R. V. Shack, and M. R. Descour, “Measurement of the three-dimensional microscope point spread function using a shack-hartmann wavefront sensor,” Journal of Microscopy **205**, 61–75 (2002).

[94] O. Azucena, X. Tao, J. Crest, S. Kotadia, W. Sullivan, D. Gavel, M. Reinig, S. Olivier, and J. Kubby, “Adaptive optics wide-field microscope corrections using a mems dm and shack-hartmann wavefront sensor,” in “SPIE MOEMS-MEMS,” (International Society for Optics and Photonics, 2011), pp. 79310J–79310J.

[95] R. Aviles-Espinosa, J. Andilla, R. Porcar-Guezenec, X. Levecq, D. Artigas, and P. Loza-Alvarez, “Depth aberrations characterization in linear and nonlinear microscopy schemes using a shack-hartmann wavefront sensor,” in “SPIE BiOS,” (International Society for Optics and Photonics, 2012), pp. 82271D–82271D–11.

[96] O. Azucena, J. Crest, J. Cao, W. Sullivan, P. Kner, D. Gavel, D. Dillon, S. Olivier, and J. Kubby, “Wavefront aberration measurements and corrections through thick tissue using fluorescent microsphere reference beacons,” Opt. Express **18**, 17521–17532 (2010).

[97] X. Tao, O. Azucena, M. Fu, Y. Zuo, D. C. Chen, and J. Kubby, “Adaptive optics microscopy with direct wavefront sensing using fluorescent protein guide stars,” Opt. Lett. **36**, 3389–3391 (2011).

[98] X. Tao, O. Azucena, M. Fu, Y. Zuo, D. C. Chen, and J. Kubby, “Adaptive optics confocal microscopy using fluorescent protein guide-stars for brain tissue imaging,” in “SPIE MOEMS-MEMS,” , vol. 8253 S. S. Olivier, T. G. Bifano, and J. Kubby, eds. (SPIE, 2012), vol. 8253, p. 82530M.

[99] J. M. Bueno, E. J. Gualda, and P. Artal, “Adaptive optics multiphoton microscopy to study ex vivo ocular tissues,” Journal of Biomedical Optics **15**, 066004 (2010).

[100] S. A. Rahman and M. J. Booth, “Direct wavefront sensing in adaptive optical microscopy using backscattered light,” Applied optics **52**, 5523–5532 (2013).

[101] R. Aviles-Espinosa, J. Andilla, R. Porcar-Guezenec, O. E. Olarte, M. Nieto, X. Levecq, D. Artigas, and P. Loza-Alvarez, "Measurement and correction of in vivo sample aberrations employing a nonlinear guide-star in two-photon excited fluorescence microscopy," Biomed. Opt. Express **2**, 3135–3149 (2011).

[102] K. Wang, D. E. Milkie, A. Saxena, P. Engerer, T. Misgeld, M. E. Bronner, J. Mumm, and E. Betzig, "Rapid adaptive optical recovery of optimal resolution over large volumes," Nat Meth **11**, 625–628 (2014).

[103] M. Feierabend, M. Rückel, and W. Denk, "Coherence-gated wave-front sensing in strongly scatteringsamples," Opt. Lett. **29**, 2255–2257 (2004).

[104] M. Rueckel, J. A. Mack-Bucher, and W. Denk, "Adaptive wavefront correction in two-photon microscopy using coherence-gated wavefront sensing," Proceedings of the National Academy of Sciences **103**, 17137–17142 (2006).

[105] T. van Werkhoven, H. Truong, J. Antonello, R. Fraanje, H. Gerritsen, M. Verhaegen, and C. Keller, "Coherence-gated wavefront sensing for microscopy using fringe analysis," in "SPIE MOEMS-MEMS," , vol. 8253 S. S. Olivier, T. G. Bifano, and J. Kubby, eds. (SPIE, 2012), vol. 8253, p. 82530E.

[106] B. M. Hanser, M. G. L. Gustafsson, D. A. Agard, and J. W. Sedat, "Phase retrieval of widefield microscopy point spread functions," in "Proc. SPIE," (2001), pp. 60–68.

[107] B. M. Hanser, M. G. L. Gustaffson, D. A. Agard, and J. W. Sedat, "Phase-retrieved pupil functions in wide-field fluorescence microscopy," Journal of Microscopy **216**, 32–48 (2004).

[108] P. Kner, J. Sedat, D. Agard, and Z. Kam, "High-resolution wide-field microscopy with adaptive optics for spherical aberration correction and motionless focusing," Journal of Microscopy **237**, 136–147 (2010).

[109] P. Kner, "Adaptive optics for biological microscopy using phase diversity," in "SPIE MOEMS-MEMS," , vol. 8253 S. S. Olivier, T. G. Bifano, and J. Kubby, eds. (SPIE, 2012), vol. 8253, p. 82530G.

[110] B. Rappaz, P. Marquet, E. Cuche, Y. Emery, C. Depeursinge, and P. J. Magistretti, "Measurement of the integral refractive index and dynamic cell morphometry of living cells with digital holographic microscopy," Optics express **13**, 9361–9373 (2005).

[111] B. Rappaz, F. Charrière, C. Depeursinge, P. J. Magistretti, and P. Marquet, "Simultaneous cell morphometry and refractive index measurement with dual-wavelength digital holographic microscopy and dye-enhanced dispersion of perfusion medium," Optics letters **33**, 744–746 (2008).

[112] T. Dertinger, A. Loman, B. Ewers, C. B. Müller, B. Krämer, and J. Enderlein, "The optics and performance of dual-focus fluorescence correlation spectroscopy," Optics express **16**, 14353–14368 (2008).

[113] T. Dertinger, V. Pacheco, I. von der Hocht, R. Hartmann, I. Gregor, and J. Enderlein, "Two-focus fluorescence correlation spectroscopy: A new tool for accurate and absolute diffusion measurements," ChemPhysChem **8**, 433–443 (2007).

[114] C.-E. Leroux, I. Wang, J. Derouard, and A. Delon, "Adaptive optics for fluorescence correlation spectroscopy," Opt. Express **19**, 26839–26849 (2011).

[115] C.-E. Leroux, A. Grichine, I. Wang, and A. Delon, "Correction of cell-induced optical aberrations in a fluorescence fluctuation microscope," Opt. Lett. **38**, 2401–2403 (2013).

[116] C.-E. Leroux, S. Monnier, I. Wang, G. Cappello, and A. Delon, "Fluorescent correlation spectroscopy measurements with adaptive optics in the intercellular space of spheroids," Biomed. Opt. Express **5**, 3730–3738 (2014).

[117] T. Wilson and A. Carlini, "Size of the detector in confocal imaging systems," Optics letters **12**, 227–229 (1987).

[118] T. Wilson and A. Carlini, "Three-dimensional imaging in confocal imaging systems with finite sized detectors," Journal of Microscopy **149**, 51–66 (1988).

[119] J. Pawley, ed., *Handbook of Biological Confocal Microscopy* (Springer-Verlag New York Inc., 2006), 3rd ed.

[120] R. De Mets, I. Wang, J. Gallagher, O. Destaing, M. Balland, and A. Delon, "Determination of protein concentration on substrates using fluorescence fluctuation microscopy," in "SPIE BiOS," (International Society for Optics and Photonics, 2014), pp. 895007–895007.

[121] E. H. K. Stelzer, *Handbook of Biological Confocal Microscopy* (Springer-Verlag New York Inc., 2006), chap. The intermediate optical system of laser-scanning confocal microscopes., pp. 139–153.

[122] J. Gallagher, C.-E. Leroux, I. Wang, and A. Delon, "Accuracy of adaptive optics correction using fluorescence fluctuations," in "Proc. SPIE," , vol. 8978 (2014), vol. 8978, pp. 89780A–89780A–13.

[123] D. Malacara-Hernández and Z. Malacara-Hernández, *Handbook of Optical Design, Third Edition (Optical Science and Engineering)* (CRC Press, 2016).

[124] A. Negrean and H. D. Mansvelder, "Optimal lens design and use in laser-scanning microscopy," Biomed. Opt. Express **5**, 1588–1609 (2014).

[125] S. Bará, "Measuring eye aberrations with hartmann–shack wave-front sensors: Should the irradiance distribution across the eye pupil be taken into account?" JOSA A **20**, 2237–2245 (2003).

[126] J. Mertz, H. Paudel, and T. G. Bifano, "Field of view advantage of conjugate adaptive optics in microscopy applications," Applied optics **54**, 3498–3506 (2015).

[127] X. Tao, T. Lam, B. Zhu, Q. Li, M. R. Reinig, and J. Kubby, "Conjugate adaptive optics with remote focusing for three-dimensional focusing through scattering media," arXiv preprint arXiv:1702.05163 (2017).

[128] J.-H. Park, L. Kong, Y. Zhou, and M. Cui, "Large-field-of-view imaging by multi-pupil adaptive optics," Nature Methods (2017).

[129] R. D. Simmonds and M. J. Booth, "Modelling of multi-conjugate adaptive optics for spatially variant aberrations in microscopy," Journal of Optics **15**, 094010 (2013).

[130] A. Dubra and Y. Sulai, "Reflective afocal broadband adaptive optics scanning ophthalmoscope," Biomedical optics express **2**, 1757–1768 (2011).

[131] T. Wohland, R. Rigler, and H. Vogel, "The standard deviation in fluorescence correlation spectroscopy," Biophysical journal **80**, 2987–2999 (2001).

[132] M. Wahl, I. Gregor, M. Patting, and J. Enderlein, "Fast calculation of fluorescence correlation data with asynchronous time-correlated single-photon counting," Optics Express **11**, 3583–3591 (2003).

[133] E. Schaub, "F2cor: fast 2-stage correlation algorithm for fcs and dls," Optics express **20**, 2184–2195 (2012).

[134] M. Molteni and F. Ferri, “Commercial counterboard for 10 ns software correlator for photon and fluorescence correlation spectroscopy,” Review of Scientific Instruments **87**, 113108 (2016).

[135] J. W. Krieger, A. P. Singh, N. Bag, C. S. Garbe, T. E. Saunders, J. Langowski, and T. Wohland, “Imaging fluorescence (cross-) correlation spectroscopy in live cells and organisms,” Nature protocols **10**, 1948–1974 (2015).

[136] J. W. Krieger and J. Langowski, “Quickfit 3.0 (status: beta, compiled: ???, svn: ???): A data evaluation application for biophysics,” [web page] `http://www.dkfz.de/Macromol/quickfit/` (2015).

[137] M. A. Digman, C. M. Brown, P. Sengupta, P. W. Wiseman, A. R. Horwitz, and E. Gratton, “Measuring fast dynamics in solutions and cells with a laser scanning microscope,” Biophysical journal **89**, 1317–1327 (2005).

[138] C. E. Leroux, “Time-resolved aberrometry of the eye with a shack-hartmann wavefront sensor,” Ph.D. thesis, National University of Ireland Galway (2010).

[139] C. Leroux and C. Dainty, “Estimation of centroid positions with a matched-filter algorithm: relevance for aberrometry of the eye,” Opt. Express **18**, 1197–1206 (2010).

[140] O. Lardiere, R. Conan, R. Clare, C. Bradley, and N. Hubin, “Performance comparison of centroiding algorithms for laser guide star wavefront sensing with extremely large telescopes,” Appl. Opt. **49**, G78–G94 (2010).

[141] S. Thomas, T. Fusco, A. Tokovinin, M. Nicolle, V. Michau, and G. Rousset, “Comparison of centroid computation algorithms in a shack-hartmann sensor,” Monthly Notices of the Royal Astronomical Society **371**, 323–336 (2006).

[142] K. Baker and M. Moallem, “Iteratively weighted centroiding for shack-hartmann wave-front sensors,” Optics express **15**, 5147–5159 (2007).

[143] W. T. Welford, *Aberrations of Optical Systems*, Adam Hilger series on Optics and Optoelectronics (Adam Hilger, 1986).

[144] M. Born and E. Wolf, *Principles of Optics: Electromagnetic Theory of Propagation, Interference and Diffraction of Light* (Cambridge University Press, 2000).

[145] C. T. Culbertson, S. C. Jacobson, and J. M. Ramsey, “Diffusion coefficient measurements in microfluidic devices,” Talanta **56**, 365–373 (2002).

[146] E. M. Daly and C. Dainty, “Ophthalmic wavefront measurements using a versatile pyramid sensor,” Applied Optics **49**, G67–G77 (2010).

[147] Juskaitis, *Handbook of Biological Confocal Microscopy* (Springer, New York., 2006), chap. Measuring the real point spread function of high numerical aperture microscope objective lenses., pp. 239–250, 3rd ed.

[148] A. Jesacher, A. Thayil, K. Grieve, D. DÃ©barre, T. Watanabe, T. Wilson, S. Srinivas, and M. Booth, “Adaptive harmonic generation microscopy of mammalian embryos,” Opt. Lett. **34**, 3154–3156 (2009).

[149] J. Antonello, T. van Werkhoven, M. Verhaegen, H. H. Truong, C. U. Keller, and H. C. Gerritsen, “Optimization-based wavefront sensorless adaptive optics for multiphoton microscopy,” J. Opt. Soc. Am. A **31**, 1337–1347 (2014).

[150] H. Qian and E. L. Elson, “Distribution of molecular aggregation by analysis of fluctuation moments.” Proceedings of the National Academy of Sciences **87**, 5479–5483 (1990).

[151] M. A. Digman, R. Dalal, A. F. Horwitz, and E. Gratton, “Mapping the number of molecules and brightness in the laser scanning microscope,” Biophys J **94**, 2320–2332 (2008).

[152] J. D. Müller, “Cumulant analysis in fluorescence fluctuation spectroscopy,” Biophys J **86**, 3981–3992 (2004).

[153] L. Mandel, “Fluctuations of photon beams and their correlations,” Proceedings of the Physical Society **72**, 1037 (1958).

[154] D. E. Koppel, “Statistical accuracy in fluorescence correlation spectroscopy,” Physical Review A **10**, 1938–1945 (1974).

[155] H. Qian, “On the statistics of fluorescence correlation spectroscopy,” Biophysical Chemistry **38**, 49–57 (1990).

[156] S. Saffarian and E. L. Elson, “Statistical analysis of fluorescence correlation spectroscopy: The standard deviation and bias,” Biophysical Journal **84**, 2030–2042 (2003).

[157] W. B. Davenport, W. L. Root *et al.*, *An introduction to the theory of random signals and noise*, vol. 159 (McGraw-Hill New York, 1958).

[158] T. Wilson and C. Sheppard, *Theory and practice of scanning optical microscopy*, vol. 180 (Academic Press London, 1984).

[159] S. Hell and E. H. K. Stelzer, *Handbook of Biological confocal Microscopy* (Springer-Verlag New York Inc., 2006), chap. Lens aberrations in confocal fluorescence microscopy, pp. 347–354, 3rd ed.

[160] N. Ji, T. R. Sato, and E. Betzig, “Characterization and adaptive optical correction of aberrations during in vivo imaging in the mouse cortex,” Proceedings of the National Academy of Sciences **109**, 22–27 (2012).

[161] L. N. Thibos, X. Hong, A. Bradley, and X. Cheng, “Statistical variation of aberration structure and image quality in a normal population of healthy eyes,” JOSA A **19**, 2329–2348 (2002).

[162] R. Lane, A. Glindemann, J. Dainty *et al.*, “Simulation of a kolmogorov phase screen,” Waves in random media **2**, 209–224 (1992).

[163] J. Wang and J. Markey, “Modal compensation of atmospheric turbulence phase distortion,” JOSA **68**, 78–87 (1978).

[164] T. Wilson and A. Carlini, “The effect of aberrations on the axial response of confocal imaging systems,” Journal of Microscopy **154**, 243–256 (1989).

[165] S. Popoff, G. Lerosey, M. Fink, A. C. Boccara, and S. Gigan, “Image transmission through an opaque material,” Nature Communications **1**, 81 (2010).

[166] S. Popoff, G. Lerosey, R. Carminati, M. Fink, A. Boccara, and S. Gigan, “Measuring the transmission matrix in optics: an approach to the study and control of light propagation in disordered media,” Physical review letters **104**, 100601 (2010).

[167] O. Katz, E. Small, and Y. Silberberg, “Looking around corners and through thin turbid layers in real time with scattered incoherent light,” Nature Photonics **6**, 549–553 (2012).

[168] O. Katz, P. Heidmann, M. Fink, and S. Gigan, “Non-invasive single-shot imaging through scattering layers and around corners via speckle correlations,” Nature Photonics **8**, 784–790 (2014).

[169] S. Zustiak, J. Riley, H. Boukari, A. Gandjbakhche, and R. Nossal, “Effects of multiple scattering on fluorescence correlation spectroscopy measurements of particles moving within optically dense media,” Journal of biomedical optics **17**, 125004–125004 (2012).

[170] P. Schiebener, J. Straub, J. Levelt Sengers, and J. Gallagher, “Refractive index of water and steam as function of wavelength, temperature and density,” Journal of physical and chemical reference data **19**, 677–717 (1990).

[171] S. A. Kim, K. G. Heinze, and P. Schwille, “Fluorescence correlation spectroscopy in living cells,” Nature methods **4**, 963–973 (2007).

[172] D. Koppel, D. Axelrod, J. Schlessinger, E. Elson, and W. Webb, “Dynamics of fluorescence marker concentration as a probe of mobility,” Biophysical Journal **16**, 1315–1329 (1976).

[173] M. Dolega, M. Delarue, F. Ingremeau, J. Prost, A. Delon, and G. Cappello, “Cell-like pressure sensors reveal increase of mechanical stress towards the core of multicellular spheroids under compression,” Nature Communications **8** (2017).

[174] F. Ingremeau, M. E. Dolega, J. Gallagher, I. Wang, G. Cappello, and A. Delon, “Optical sensing of mechanical pressure based on diffusion measurement in polyacrylamide cell-like barometers,” Soft Matter pp. – (2017).

[175] M. L. Byron and E. A. Variano, “Refractive-index-matched hydrogel materials for measuring flow-structure interactions,” Experiments in fluids **54**, 1456 (2013).

[176] R. Schwartz, J. M. Berry, A. Subramanian, and X. Shi, “Non-tumorigenic mdck cell line for propagating viruses,” (2014). US Patent 8,748,174.

[177] R. M. Sutherland, “Cell and environment interactions in tumor microregions: the multicell spheroid model,” Science **240**, 177 (1988).

[178] F. Montel, M. Delarue, J. Elgeti, L. Malaquin, M. Basan, T. Risler, B. Cabane, D. Vignjevic, J. Prost, G. Cappello *et al.*, “Stress clamp experiments on multicellular tumor spheroids,” Physical review letters **107**, 188102 (2011).

[179] M. Delarue, F. Montel, O. Caen, J. Elgeti, J.-M. Siaugue, D. Vignjevic, J. Prost, J.-F. Joanny, and G. Cappello, “Mechanical control of cell flow in multicellular spheroids,” Physical review letters **110**, 138103 (2013).

[180] M. Delarue, F. Montel, D. Vignjevic, J. Prost, J.-F. Joanny, and G. Cappello, “Compressive stress inhibits proliferation in tumor spheroids through a volume limitation,” Biophysical journal **107**, 1821–1828 (2014).

[181] S. Monnier, M. Delarue, B. Brunel, M. E. Dolega, A. Delon, and G. Cappello, “Effect of an osmotic stress on multicellular aggregates,” Methods **94**, 114 – 119 (2016). Experimental Approaches in Mechanotransduction.

[182] B. Amsden, “Solute diffusion within hydrogels. mechanisms and models,” Macromolecules **31**, 8382–8395 (1998).

[183] R. J. Phillips, W. M. Deen, and J. F. Brady, “Hindered transport in fibrous membranes and gels: effect of solute size and fiber configuration,” Journal of colloid and interface science **139**, 363–373 (1990).

[184] R. J. Phillips, “A hydrodynamic model for hindered diffusion of proteins and micelles in hydrogels.” Biophysical Journal **79**, 3350 (2000).

[185] E. M. Johnson, D. A. Berk, R. K. Jain, and W. M. Deen, "Hindered diffusion in agarose gels: test of effective medium model," Biophysical journal **70**, 1017–1023 (1996).

[186] K. Mandal, I. Wang, E. Vitiello, L. A. C. Orellana, and M. Balland, "Cell dipole behaviour revealed by ecm sub-cellular geometry," Nature communications **5** (2014).

[187] T. Boudou, J. Ohayon, C. Picart, R. I. Pettigrew, and P. Tracqui, "Nonlinear elastic properties of polyacrylamide gels: implications for quantification of cellular forces," Biorheology **46**, 191–205 (2009).

[188] Q. Tseng, I. Wang, E. Duchemin-Pelletier, A. Azioune, N. Carpi, J. Gao, O. Filhol, M. Piel, M. Théry, and M. Balland, "A new micropatterning method of soft substrates reveals that different tumorigenic signals can promote or reduce cell contraction levels," Lab on a chip **11**, 2231–2240 (2011).

[189] B. Cabane and S. Hénon, *Liquides: solutions, dispersions, émulsions, gels* (Belin Paris, 2003).

[190] A. Bouchoux, P.-E. Cayemitte, J. Jardin, G. Gésan-Guiziou, and B. Cabane, "Casein micelle dispersions under osmotic stress," Biophysical journal **96**, 693–706 (2009).

[191] H. R. Verstraete, S. Wahls, J. Kalkman, and M. Verhaegen, "Model-based sensor-less wavefront aberration correction in optical coherence tomography," Optics letters **40**, 5722–5725 (2015).

[192] P. Pozzi, D. Wilding, O. Soloviev, H. Verstraete, L. Bliek, G. Vdovin, and M. Verhaegen, "High speed wavefront sensorless aberration correction in digital micromirror based confocal microscopy," Optics Express **25**, 949–959 (2017).

List of Figures